UNIVERSITY OF SOUTHAMPTON

FACULTY OF NATURAL AND ENVIRONMENTAL SCIENCES

Ocean and Earth Science, National Oceanography Centre Southampton

Heating and Cooling or Ebbing and Flowing? Oceanic Change from a Thermohaline Perspective

by

Dafydd Gwyn Evans

Thesis for the degree of Doctor of Philosophy

November 2016

UNIVERSITY OF SOUTHAMPTON

ABSTRACT

FACULTY OF NATURAL AND ENVIRONMENTAL SCIENCES
Ocean and Earth Science, National Oceanography Centre Southampton

Doctor of Philosophy

HEATING AND COOLING OR EBBING AND FLOWING? OCEANIC CHANGE FROM A THERMOHALINE PERSPECTIVE

by Dafydd Gwyn Evans

This thesis develops and applies novel methods to understand water mass variability and change in the global ocean. A water mass framework is developed that determines the diathermal and diahaline transformations of water between water mass classes from the temporal variations in their volumetric distribution. Water masses are defined in terms of their temperature and salinity. This reveals the roles of air–sea fluxes, mixing and transport changes. The second chapter explores the drivers of interannual variability in the overturning circulation in the North Atlantic subtropical gyre using the water mass framework. Variations in the volumetric distribution of water masses reveal that transport anomalies at the gyre boundaries predominantly set the volume and heat budget and that these transport anomalies are governed by Ekman pumping over the gyre. In the third and fourth chapters of this thesis the water mass framework is applied to observations of temperature and salinity in the Southern Ocean. Seasonal variations in the distribution of water masses reveal the imprint of the Southern Ocean overturning. This highlights the importance of seasonally varying air-sea fluxes in the formation of intermediate water at the expense of deep water, winter water and surface water. This reveals a diabatic pathway for the upwelling and conversion of deep water into intermediate water. Deep water is first cooled and freshened during the winter by mixing with overlying winter water triggered by a cabbeling instability. Sea ice-melt and surface heating then warm and freshen this seasonally formed water mass to create intermediate water during the summer months. These results suggest that the process of cabbeling could be a rate determining step in the global overturning circulation and the upwelling of deep waters. The fifth chapter of this thesis explores an alternative method to determine a volumetric distribution using individual Argo profiles. The volumetric distribution determined using this profile based estimate is compared to the distribution calculated using a geographically interpolated dataset. This comparison reveals that the interpolation scheme used to geographically grid Argo appears to artificially mix water masses toward the centre of the distribution.

Contents

List of Figures

Declaration of Authorship

I, Dafydd Gwyn Evans , declare that the thesis entitled *Heating and Cooling or Ebbing and Flowing? Oceanic Change from a Thermohaline Perspective* and the work presented in the thesis are both my own, and have been generated by me as the result of my own original research. I confirm that:

- this work was done wholly or mainly while in candidature for a research degree at this University;
- where any part of this thesis has previously been submitted for a degree or any other qualification at this University or any other institution, this has been clearly stated;
- where I have consulted the published work of others, this is always clearly attributed;
- where I have quoted from the work of others, the source is always given. With the exception of such quotations, this thesis is entirely my own work;
- I have acknowledged all main sources of help;
- where the thesis is based on work done by myself jointly with others, I have made clear exactly what was done by others and what I have contributed myself;
- parts of this work have been published as: Evans et al. (2014)

Signed:.....

Date:.....

Acknowledgements

Firstly, thank you to my supervisors Jan Zika, Alberto Naveira Garabato and George Nurser. They've all been a great support and I have learned a lot from each of them over the last 4 years. Thanks in particular to Jan, who has had a pretty tough few years. Nevertheless, he has always remained enthusiastic and excited about the work in this thesis. I couldn't have asked for a better supervisor. I'd also like to thank John Toole and Gael Forget for their help and support during my three month exchange at WHOI, and their involvement with the second chapter of this thesis.

At NOCS, there have been so many people who've helped me along the way and made life so much more bearable during my PhD. In a generally quiet office, Alastair has been great company, as has Leigh, who moved out a while ago still makes her presence felt by insisting on regular "lunch clubs". Everyone in my year have been great company, and I'm looking forward to celebrating each of their PhDs over the next year (or so). The same goes for the guys up in Oxford, who have been great conference travel companions during my PhD.

Outside of NOCS, I have an amazing group of friends who've been there for me through it all. They've all been great, but I'll name a few specifically here. Thanks to Rob and Fran for providing entertainment in the form of kittens, and many other things of course (including reading this thesis). Thank you to Tompy (and by extension Katie) for the lunch time coffees and for dragging me away when I needed it. And to Lloyd and Cha, who have helped with (among many other things) their regular and excellent music recommendations that make office life much more enjoyable.

Thank you to my Mum, Dad and all my extended family for basically putting up with me and supporting me through all of this. I couldn't be here now without you. And finally thank you to Ale, who has supported me ridiculous amounts over the last year. Thank you for always believing in me, and for giving me a well needed confidence boost when it's been lacking. This wouldn't have happened without you.

Chapter 1

Introduction

1.1 Understanding a changing ocean

The ocean changes. Understanding how and why it changes is the motivation of this thesis. The aim is to develop a framework that could ultimately aid our understanding of how anthropogenic climate change affects the temperature and salinity of the ocean. The challenge of achieving this aim involves separating the diabatic processes that change temperature and salinity from the transport processes that change temperature and salinity locally.

Diabatic changes in oceanic temperature or salinity occur as a consequence of a direct addition/removal of heat or freshwater by so called air–sea exchange between the atmosphere and the ocean and by mixing between adjacent parcels of water, or water masses (e.g. Walin, 1982). Temperature and salinity may also change diabatically due to sea-ice formation and riverine/cryosphere runoff. The focus of many recent studies has been to quantify both the decadal trends and oscillations in global ocean temperature and salinity and their drivers (e.g. Durack and Wijffels, 2010; Helm et al., 2010; Durack et al., 2012; Roemmich et al., 2012; Häkkinen et al., 2015). These studies seek to understand the effect that anthropogenic climate change is having on the exchange of heat between the atmosphere and ocean and on the strength of the global freshwater cycle. However, an appropriate quantification of such trends and oscillations requires a complete understanding of the processes that drive this variability at all spatial and temporal scales.

Spatially, at the smallest scale, oceanic temperature and salinity vary on a molecular level through diffusion and mixing. Beyond this, centimetre scale variability is set by turbulence, while submesoscale fluctuations drive variability at scales up to the order of 1km. At scales of greater than 10 km the effect of the Earth's rotation largely controls the flows that drive the mesoscale and basin scale spatial variations. On a

temporal scale, at the high end of the spectrum the ocean varies at diurnal and inertial frequencies. There is significant variability at annual frequencies due to the seasonal cycle, particularly in the high latitude oceans. The very low frequency, basin scale modes of variability drive interannual and decadal changes in temperature and salinity, while variability on centennial through to millennial scales is set by changes in the solar output and the orbit/rotational properties of the Earth (Imbrie et al., 1992). Crucially, long term trends calculated from observations of temperature and salinity in the ocean must not be aliased by spatial and temporal variability with higher or lower frequencies.

Defining the full spectrum of temperature and salinity variability in the ocean is hindered by limited sub-surface observations. Records of temperature and salinity suitable for defining long term trends do not exist earlier than the 1950s (Durack and Wijffels, 2010; Roemmich and Gilson, 2009). The inhomogeneity of these observations in space and time further compound these difficulties. Earlier datasets for example, are biased towards the Northern Hemisphere oceans and are predominantly sampled during the summer (Roemmich and Gilson, 2009). It is the advent of the Argo Program in the early 2000s which has really set the precedent for spatially and temporally rich records of ocean observations. Yet consistent Argo observations do not exist below 2000m and uncertainties in observations of temperature and salinity are still apparent at the smaller spatial scales associated with mesoscale and submesoscale variability (McGillicuddy et al., 2007; Calil and Richards, 2010; Chelton et al., 2011).

Changes in ocean heat and freshwater content can also be determined from estimates of the air–sea fluxes of heat and freshwater. This is achieved by calculating how a change in the air–sea fluxes drives a change in the transformation of water between water masses (Speer, 1993). This approach amounts to estimating an implied oceanic change directly from the air–sea changes, as opposed to observing these changes in the ocean. Uncertainty arises with this approach as a consequence of a poor agreement between model, satellite and in situ based air–sea flux estimates (Stephens et al., 2010; Smith et al., 2011; Josey, 2011). With regards to estimating the changing oceanic heat content for example, these uncertainties amount to a global imbalance in the exchange of heat between the air–sea interface equating to 20-30 Wm^{-2} that dwarfs the signal of anthropogenic climate change which is of the order 1 Wm^{-2} (Josey, 2011). A lack of oceanic observational records is an issue that particularly affects these discrepancies between air–sea flux datasets (Josey et al., 1999; Schanze et al., 2010), especially in data-sparse regions such as the Southern Ocean (Schulz et al., 2012). Recent studies have shown that it is easier to estimate changes in oceanic heat content and the global freshwater cycle from variations in oceanic temperature and salinity (Helm et al., 2010; Durack et al., 2012; Häkkinen et al., 2015; Zika et al., 2015). There has however been more success using air–sea flux products to estimate seasonal and interannual changes in water mass properties and ocean circulation (e.g. Forget et al., 2011; Grist et al., 2014).

Numerical models of the ocean are a useful tool with which to compare and contrast observations of the oceans. Ocean models also provide a platform to augment ocean observations, with global simulations with an ever increasing spatial resolution, providing estimates of past oceanic trends (Domingues et al., 2008; Durack et al., 2012) and predicting future changes (Collins et al., 2013). Poor agreement between individual models and disagreement between models and observations do however raise uncertainty in these estimates. Regardless, a robust comparison between observations and ocean models is a powerful way to validate observed oceanic variability and investigate their causes when spatial and temporal coverage become a limiting factor. In addition, models can be synthetically sampled with dummy observations to check whether real observations are giving an accurate estimate of large scale changes (Hirschi and Marotzke, 2007). Constraining ocean models with observations is an effective way to improve numerical models. This has been performed most effectively in ocean state estimates that use adjoint methods to converge model output to observations in a physically consistent manner (Forget et al., 2015). Such state estimates for example have been used to asses decadal changes in deep ocean heat content (Wunsch and Heimbach, 2014).

Conventionally we estimate changes in temperature and salinity by comparing data from one location at different times. The difficulty with this approach is that the resultant changes may not be specifically due to changing air–sea fluxes or differences in mixing intensity. Vertical heave of isopycnal surfaces and lateral transport of water will also result in a change in temperature or salinity. For example, the vertical upwelling of isopycnal surfaces by mesoscale eddies or by basin scale changes in wind-stress will appear as a cooling on a fixed depth surface (Bindoff and McDougall, 1994). Alternatively, a reduction in the northward transport of warm and salty water by the Atlantic meridional overturning circulation will imprint as a cooling and freshening in the high latitudes of the North Atlantic (Pardaens et al., 2008). The alternative to this conventional approach is to use a framework which follows surfaces of constant temperature, salinity or density, and measures change along or within those surfaces. Doing so will naturally remove the component of change due to heave, isolating the diabatic change. The most widely used of these quasi-Lagrangian coordinate systems is the water mass framework introduced by Walin (1982) and the isopycnal framework pioneered by Bindoff and McDougall (1994). The work presented in this thesis develops and extends the framework of Walin (1982).

To summarise, understanding oceanic change relies on a thorough understanding of the processes that affect observations of temperature and salinity. Knowing this, the chosen coordinate system must isolate the processes of interest. In the case of this thesis, these processes are changes in the diabatic air–sea fluxes of heat and freshwater and the intensity of sub-surface mixing. A significant unknown, which will be discussed below, is the role of advective transports in driving temperature and salinity changes. This thesis focuses on implementing the water mass framework in regions of the ocean where

the seasonal and interannual variations in air–sea fluxes and mixing are closely linked to the overturning circulation, namely the subtropical North Atlantic and the Southern Ocean. Thus, a robust framework is developed within which the impact of seasonal and interannual mixing and transport variability is known and understood, allowing improved estimates long-term diabatic changes. The following sections will provide background on the isopycnal and water mass frameworks and justify the implementation of the water mass framework as a starting point for this thesis. The final section of this chapter summarises the individual chapters of this thesis.

1.2 The ocean on isopycnal coordinates

The ocean, as observed from a conventional pressure or depth perspective, is subject to diabatic and adiabatic changes in temperature and salinity. Temperature and salinity change from a fixed hydrographic record may be caused by variations in the air–sea heat flux and balance of precipitation-evaporation at the region of the surface ocean in which the observed water type is formed. The same record can resolve fluctuations due to the adiabatic heaving of isopycnals by eddies/Rossby waves on weekly to seasonal timescales and changes in the basin scale distribution of wind stress on interannual timescales that do not represent a diabatic flux of freshwater or heat. Isolating the diabatic contribution is crucial in understanding the long-term variability in the ocean.

Observing the ocean using an isopycnal framework isolates almost entirely these diabatic processes, intrinsically removing changes due to isopycnal heaving (Bindoff and McDougall, 1994). To understand changes on isopycnal surfaces it is important to recognise how variations in the surface ocean fluxes of heat and freshwater resolve as a change from an isopycnal perspective. The scenarios of contrasting change in pressure and isopycnal coordinates by are discussed by Bindoff and McDougall (1994). They are pure warming, pure freshening and pure heave. A schematic summary of this work is shown and described in Figure 1.1. Bindoff and McDougall (1994) reveal the interesting properties of temperature and salinity change on isopycnal surfaces, where a warmed parcel of water appears to cool and freshen on an isopycnal surface. Alternatively, a freshened water parcel appears to freshen and cool on an isopycnal surface. These changes assume that temperature and salinity both decrease with depth.

A good example of the isopycnal framework in use is the analysis of a combination of Argo float data and hydrographic data in the Southern Ocean (Böning et al., 2008). The ventilation of water masses in the Southern Ocean is linked to the vigour of the meridional overturning circulation (MOC). In the Southern Ocean, the MOC is sensitive to changes in surface fluxes and stronger extratropical southern hemisphere westerlies projected for the 21st century (Fyfe and Saenko, 2006; Downes et al., 2009). The water masses formed within the Southern Ocean spread the globally. Changes in the water

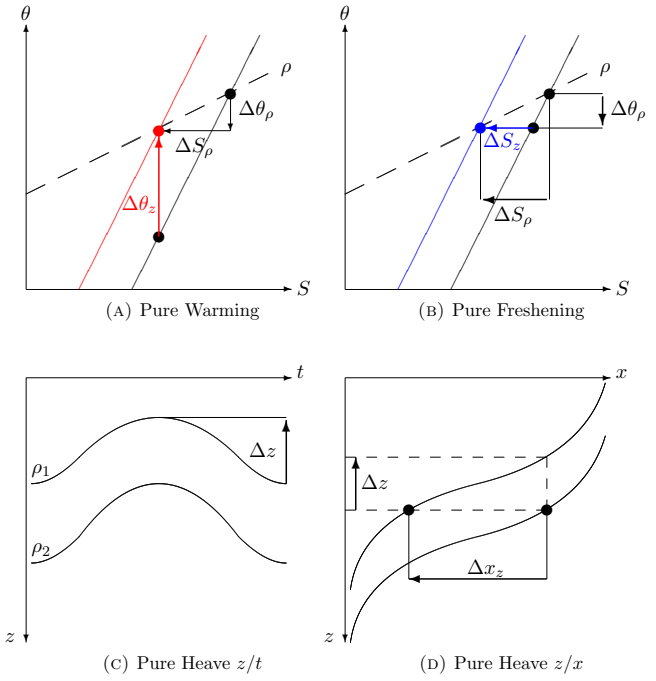

Figure 1.1: Examples of the (a) pure warming , (b) pure freshening and (c)/(d) pure heaving scenarios described by Bindoff and McDougall (1994). In (a) a parcel of water is warmed ($\Delta\theta_z$) on the original thermocline to density ρ which is colder ($\Delta\theta_\rho$) and fresher (ΔS_ρ) than a parcel of water with density ρ on the original thermocline. In (b) a parcel or water is freshened (ΔS_z) on the original thermocline to density ρ which is colder ($\Delta\theta_\rho$) and fresher (ΔS_ρ) than a parcel of water with density ρ on the original thermocline. In (c) and (d) density surfaces (ρ_1 and ρ_2) within the thermocline are raised by Δz (e.g. passage of anticyclonic eddy through fixed point time-series) resulting in a reduction of Δx_z, where x is potential temperature or salinity. There is no change in temperature or salinity on isopycnal coordinates in the pure heave scenario. After Bindoff and McDougall (1994).

masses ventilated in the Southern Ocean thus impact subsurface changes observed in the Atlantic (McCarthy et al., 2011, 2012b), Indian (Bindoff and McDougall, 2000; Bryden et al., 2003; McDonagh et al., 2005; Kobayashi et al., 2012) and Pacific (Boyer et al., 2005; Downes et al., 2009; Durack and Wijffels, 2010) Oceans.

Böning et al. (2008) reveal a coherent pattern of change along the circumpolar extent of the ACC. This consisted of a warming and freshening of water masses accompanied by a southward shift of isopycnal outcrops with no change in the slope of isopycnals and therefore the strength of the Antarctic Circumpolar Current (ACC) (Figure 1.2(a)). These changes were diagnosed using analysis of temperature and salinity trends on isopycnal and pressure surfaces at specific latitudes (Figure 1.2). The importance of understanding how the gradient of the temperature/salinity curve impacts the change observed on an isopycnal is underlined by this study. This is highlighted in Figure

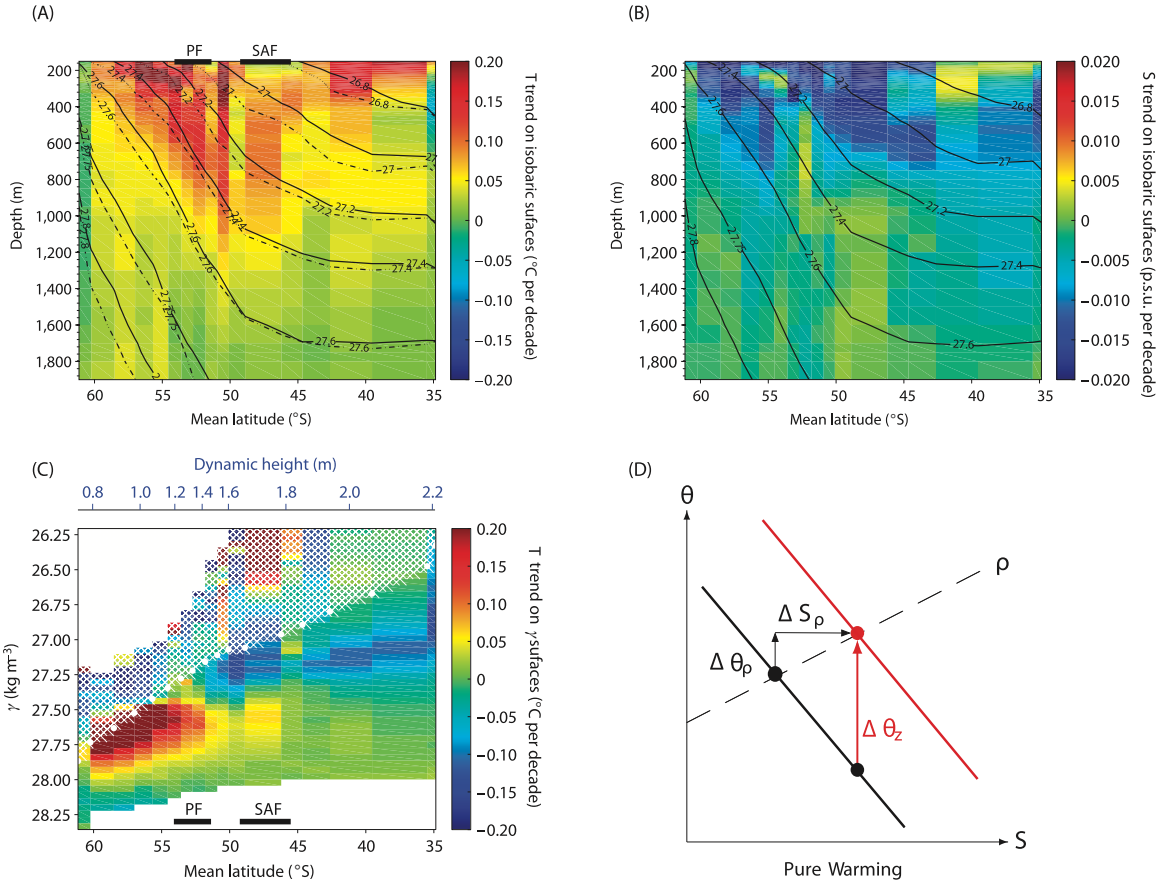

Figure 1.2: (a) and (b) Trends in potential temperature and salinity since the 1960s on pressure surfaces zonally averaged along the circumpolar extent of the ACC. Contours represent density, and the southward migration of isopycnals since the 1960s (from the solid to the dot-dashed contours). Black bars represent the mean position of the SAF and PF. (c) Potential temperature trends for the same period on isopycnal surfaces. White dots indicate the average density at 200m. (d) Example of pure warming scenario on an isopycnal surface where salinity increases with depth. A parcel of water is warmed ($\Delta\theta_z$) on the original thermocline to density ρ which is warmer ($\Delta\theta_\rho$) and saltier (ΔS_ρ) than a parcel of water with density ρ on the original thermocline. Adapted from Böning et al. (2008) and Bindoff and McDougall (1994).

1.2 so that on pressure surfaces (Figure 1.2(a) and 1.2(b)) temperature and salinity show a warming and freshening across both the polar front (PF) and the subantarctic front (SAF). North of the PF this manifests as a cooling (and freshening) on isopycnal surfaces (Figure 1.2(c)) when temperature and salinity decrease with depth, as discussed in Figure 1.2. Contrastingly, to south of the PF at densities greater than 27.2, there is as a warming (and salinisation) on isopycnal surfaces which is a consequence of the reversed gradient in temperature/salinity in this region, with temperature and salinity increasing with depth, as illustrated in Figure 1.2(d).

A further example of a study that utilises an isopycnal framework is a comprehensive

analysis of a 50 year time-series of global ocean salinity on pressure and density surfaces (Durack and Wijffels, 2010). In general, Durack and Wijffels (2010) show that a freshening occurred at high latitudes in the subpolar gyres and the subsurface waters ventilated by the water masses formed in these regions. Elevated salinity is seen within the subtropical gyres and below the surface in the mode waters formed within the region of these gyres. Thus, surface changes in salinity reflect the intensification of the Precipitation–Evaporation (P–E) field in a warmer atmosphere (Durack and Wijffels, 2010; Durack et al., 2012).

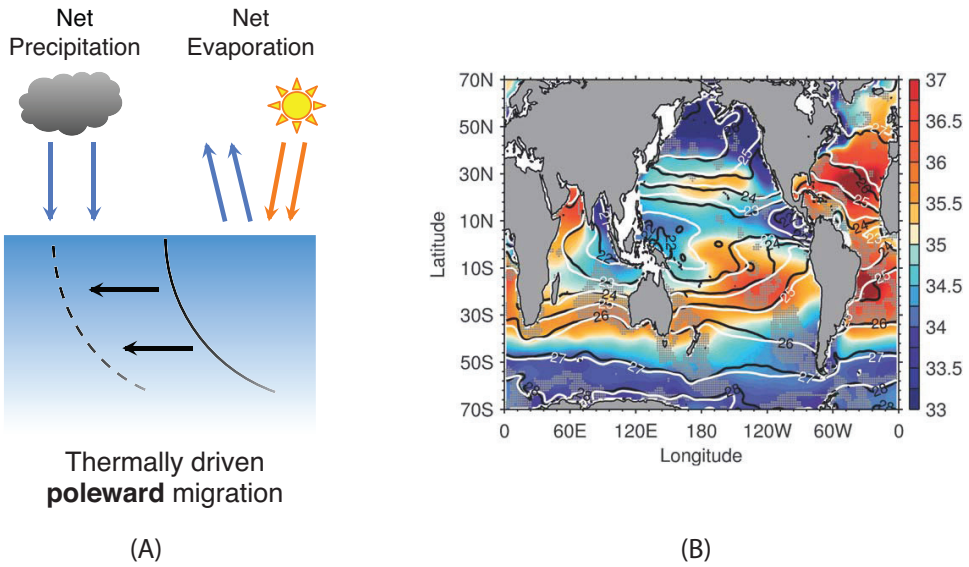

Figure 1.3: (a) Schematically represented migration of isopycnal outcrops due to oceanic warming. A change in salinity occurs as the outcrop migrates from a region of net evaporation to a region of net precipitation. (b) Position of winter isopycnal outcrops overlaid on the climatological mean salinity. From Durack and Wijffels (2010).

In determining the diabatic fluxes required to induce the observed trends in the global ocean, Durack and Wijffels (2010) demonstrate the importance of considering the effect of the meridional migration of isopycnal outcrops on changes observed on isopycnal surfaces. They show that salinity may change on an isopycnal when outcrops migrate, due to a large scale warming, between precipitation and evaporative dominated regions (Figure 1.3(a) and 1.3(b))(Durack and Wijffels, 2010). The importance of outcrop migration is further emphasised in an analysis of the Southern Ocean that showed trends on isopycnal surfaces relative to dynamic height contours across the ACC (Meijers et al., 2011). This analysis showed an adiabatic warming across the ACC could be induced by the poleward migration of isopycnal outcrops when inferring isopycnal changes at fixed latitudes. This would therefore contribute to the trends shown Böning et al. (2008).

Changes in ocean circulation have also been highlighted as a source of adiabatic variability in an isopycnal framework. This source of variability is likely important in the analysis of trends by Curry et al. (2003) and Curry and Mauritzen (2005) for example,

who compare trends in salinity on density and depth surfaces in the Atlantic basin. They show that at latitudes greater than 40°N the water column freshened on depth and isopycnal surfaces between 1985-99, with a decrease of 0.03 psu, encompassing the waters that compose the North Atlantic Deep Water (NADW). South of 25°S, the salinity of surface thermocline waters decreased by <0.2 psu, while the salinity of Antarctic Intermediate Water (AAIW) and Upper Circumpolar Deep Water (UCDW) decreased by 0.02 psu. These changes are apparent on both isopycnals and depth surfaces, but appear more coherent on isopycnals, reflecting subduction of water on isopycnals that have been altered diabatically by changing surface fluxes. Curry et al. (2003) attribute the freshening trends to an increase in precipitation in addition to an increase in the volume of freshwater and ice being exported from the Arctic. In addition, increased evaporation in the tropical and subtropical Atlantic Ocean is thought to have raised salinity on both depth and isopycnal surfaces between the sea surface and 500m (Curry et al., 2003; Boyer et al., 2005; Hosoda et al., 2009; Durack and Wijffels, 2010).

However, a weakening of the Atlantic Meridional Overturning Circulation (AMOC) and therefore the transport of warm and salty water from the subtropical Atlantic Ocean into the subpolar Atlantic, could imprint as a cooling and freshening trend on isopycnals as shown in model analyses (Pardaens et al., 2008). Further, in the South Atlantic different salinity changes have been reported in AAIW, with a freshening reported between 1985 and 1999 (Curry et al., 2003) and a contrary salinisation between 1983 and 2009 (McCarthy et al., 2011). Fluctuations in the transport of saltier AAIW from the Indian Ocean in to the South Atlantic has been suggested as a source of variability that could produce this difference (McCarthy et al., 2011). More recently, westward propagating salinity anomalies have been highlighted as a potential pathway for the transport of saltier water, but the exact nature of these anomalies is unclear (McCarthy et al., 2012b).

In summary, the isopycnal framework is a useful tool to understand diabatic changes of temperature and salinity by removing the adiabatic effects of vertical heave. However, this framework is also subject to horizontal motions due to transport changes or isopycnal outcrop migration, particularly when using a fixed geographical horizontal coordinate such as latitude. Using a dynamically varying horizontal coordinate such as dynamic height is a useful alternative, but such methods are only practical in the Southern Ocean due to the unique vertical structure of the ACC.

1.3 Oceanic changes in water mass coordinates

Walin (1982) developed a quantitative framework to relate variations in the air–sea fluxes of heat to the strength of the overturning circulation in the ocean. This approach links the volume change between a pair of isothermal surfaces to the rate of transformation

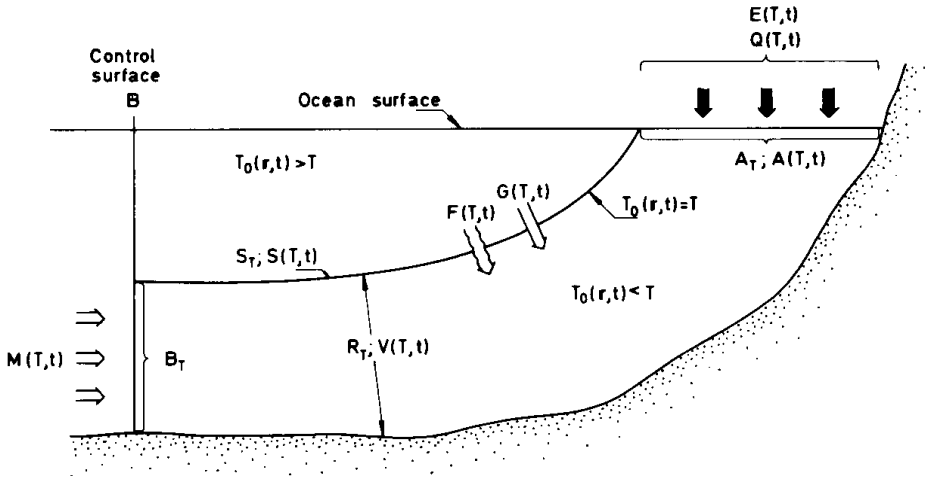

Figure 1.4: (a) Schematic representation of the processes affecting the volume of water at temperatures less than T. The transformation of water by the air–sea heat flux is shown by E, the transformation across the isotherm at T is given by G. The volume flux across the control surface B due to the transport is given by M. The definition for each term can be found in Walin (1982). From Walin (1982).

across these isothermal surfaces by air–sea fluxes and sub-surface mixing (Figure 1.4). Relating these diabatic processes to the volume change also allows the inclusion of a term representing the volumetric transport into the given temperature class when an isotherm is intersected by a geographical section or control surface as in Figure 1.4. Therefore, by tracking the volume change within a defined temperature, salinity or density class, the unwanted effect of heave is naturally removed. Unlike in the isopycnal framework horizontal motions are also naturally removed, allowing changes in oceanic temperature or salinity to be described simply in terms of air–sea fluxes, sub-surface mixing and advective processes across a defined geographical boundary.

The water mass framework presented by Walin (1982) has proved a powerful tool for understanding many aspects of the large scale circulation in the ocean, and the resultant heat and freshwater budgets of key water masses. Speer and Tziperman (1992) and Speer (1993) were among the first to apply this framework to understand the role of transformations by air–sea fluxes of heat and freshwater in the formation of North Atlantic water masses in temperature and salinity coordinates. These methodologies have been used to diagnose the water mass budget of ocean models, understanding the balance between air–sea fluxes and mixing (Nurser et al., 1999) and to validate model outputs (Marsh et al., 2005). They have also proved useful in determining the sensitivity of the meridional overturning circulation to the strength of air–sea fluxes (Nurser and Marsh, 1998; Marsh et al., 2000; Grist et al., 2009), in understanding the processes that govern the water mass transformations in the Southern Ocean (Badin et al., 2013; Cerovečki et al., 2013) and in the seasonal cycle of North Atlantic eighteen degree water/subtropical mode water volume and formation (Maze et al., 2009; Forget et al.,

2011).

The analyses that have the most relevance to this thesis are those that consider the balance of air–sea fluxes, mixing and advection in the formation and structure of water masses. Nurser et al. (1999) were among the first to describe this balance in an isopycnic model of the North Atlantic by describing the formation of water between density classes. Importantly they note that in a steady state ocean the formation of water within a given density class must be zero, so that transformation by air–sea fluxes is countered by diapycnal mixing. Thus, air–sea fluxes act to increase the width of the volumetric distribution among density classes, while mixing acts to narrow this distribution. Furthermore, this implies that if the volumetric changes between density classes and the formation by air–sea fluxes are known, the strength of diapycnal mixing can be inferred. Nurser et al. (1999) emphasise that this approach may be more useful when performed in restricted regions if the transports into and out of a given density class are known, thus capturing regions of the ocean in which diapycnal mixing is intensified.

Forget et al. (2011) apply a similar decomposition to a time varying ocean, as opposed to the mean ocean state, to estimate the seasonal cycle of North Atlantic subtropical mode water (STMW) formation. This study highlights the suitability of the water mass framework to aid the understanding of the volume budget for a specific water mass. Their decomposition highlighted the role of air–sea fluxes in driving wintertime formation of STMW, a destruction of STMW year-round by mixing and a destruction during the summer months by air–sea fluxes. Further, included within their budget is the role of advection in transporting STMW from their domain. Thus, the work of Nurser et al. (1999), Forget et al. (2011) and many others provide the context from which to understand the roles of air–sea fluxes, mixing and transport in the volumetric budget of water masses, and therefore the heat and freshwater content of the ocean. The application of the water mass framework in these analyses means that the adiabatic effects of vertical heave and isopycnal outcrop migration are naturally removed.

Defining water masses by one tracer, such as density, does provide a limitation on the application of the water mass framework. Firstly, much of the geographical information regarding a particular water mass is lost, so that conclusions regarding the relative roles of air–sea fluxes and mixing cannot easily be given a geographical context. An example is the geographical location of mixing that upwells water in the interior ocean, countering the formation at the sea-surface by air–sea fluxes (Nurser et al., 1999; Zika et al., 2012). The use of a single tracer as a definition for a water mass therefore provides no information about the meridional, zonal and vertical movement of water. In addition, within certain regions of the ocean water masses are ambiguously defined according to density classes (Marsh et al., 2005). In the Southern Ocean for example, a density class my encompass multiple water masses that are subject to contrasting forcing mechanisms. At certain times of the year, Antarctic Winter Water spans a wide range of densities that includes Circumpolar Deep Water and Antarctic Intermediate Water. Similarly, the use

of a range in temperature to define STMW, may include water that does not meet the classical definition of STMW with a low potential vorticity (Forget et al., 2011).

The use of two tracers to define water masses greatly reduces these limitations. Forget et al. (2011) for example, use potential vorticity as an additional constraint to define STMW. The major water masses that make up the worlds oceans are each uniquely defined by a specific temperature and salinity set by the surface heat and freshwater fluxes in their formation regions. A natural pair of tracers for the purpose of defining water masses is therefore temperature and salinity. In the context of the water mass framework, water mass classes are defined by a range of temperature and salinity, allowing the volume of a given temperature/salinity class to be described in terms of the transformations across surfaces of constant temperature (isotherms) and salinity (isohalines) in terms of air–sea fluxes and mixing.

The use of temperature and salinity (or thermohaline) coordinates to describe water mass variability is nothing new to oceanography. Speer (1993) described the role of surface forcing in the formation of water masses in temperature and salinity coordinates, defining vectors representing the transformation of water across isotherms and isohalines due to air–sea fluxes of heat and freshwater respectively. More recently Döös et al. (2012), Zika et al. (2012) and later Groeskamp et al. (2014) projected the mean overturning circulation of the global ocean into thermohaline coordinates, producing a thermohaline streamfunction that represents the volume transports across isothermal and isohaline surfaces. The resultant streamfunction resolves a remarkably coherent global cell reminiscent of the idealised global conveyor belt schematic (Richardson, 2008). Despite losing all geographical information, the fact that water masses have distinct temperatures and salinities relating to their formation region allows the thermohaline streamfunction to be clearly interpreted with a geographical context.

Complementing this thesis and the work of Döös et al. (2012), Zika et al. (2012) and Groeskamp et al. (2014) is the analysis of Hieronymus et al. (2014) who describes the time-mean thermohaline circulation of an ocean model by quantifying the transformations across isotherms and isohalines. This approach compares favourably with the thermohaline streamfunction, but has the advantage that the transformations due to air–sea fluxes and mixing can be separately assessed. This thesis will complement these recent advances in our view of the ocean in thermohaline coordinates by seeking to understand the time varying nature of the ocean in thermohaline coordinates. This thesis will use observations of temperature and salinity, augmented by climatologies and model output, to gain novel insights into the nature of the overturning circulation in key regions of the ocean. Thus enabling better predictions of the ways in which anthropogenic climate change may affect the momentum, heat and freshwater budgets of the ocean

1.4 Thesis outline

To summarise, this thesis will present the development of a framework that will be used to understand changes in temperature and salinity in the oceans. Understanding the complex variability of temperature and salinity requires the careful consideration of the interaction between fluctuations on multiple spatial and temporal scales. Crucially the framework must isolate diabatic changes to temperature and salinity due to air–sea fluxes and mixing, and remove adiabatic changes. The framework developed in this thesis is an extension of the water mass framework developed by Walin (1982), projecting the ocean into thermohaline coordinates as volumetric distribution. Temperature and salinity changes will then be rationalised in terms of the transformation of water across the isotherms and isohalines that define individual water mass classes. This framework naturally removes the adiabatic variability associated the vertical heave of isopycnals and the horizontal migration of isopycnal outcrops.

Much of the recent work on the representation ocean circulation in thermohaline coordinates focuses on the mean state of the ocean and therefore the relative roles of air–sea buoyancy fluxes and mixing in maintaining this mean state. The work in this thesis instead focuses on the seasonal and interannual variability of water masses in thermohaline coordinates, particularly in regions where the variations in air–sea fluxes and mixing on these time-scales are closely linked to the overturning circulation. This approach highlights the applicability of the methods developed in this thesis for separating the complicated interaction between the overturning circulation, air–sea buoyancy fluxes and mixing. The analysis in this thesis further provides the groundwork to understand long term changes in the momentum, heat and freshwater budgets of the ocean by improving our understanding of the roles mixing and advection in setting the volumetric distribution of water masses in thermohaline coordinates.

The aim of the second chapter of this thesis is to understand the drivers of interannual variability of the overturning circulation in the North Atlantic subtropical gyre. Using temperature coordinates, this analysis adopts a similar approach to Nurser et al. (1999), applying the water mass framework to both observations and models using a gridded Argo climatology and an ocean state estimate. This novel analysis explores the variability between temperature classes, capturing the large scale variations in the volumetric distribution of water masses, revealing that transport anomalies at the gyre boundaries predominantly set the volume and heat budget and that these transport anomalies are governed by Ekman pumping over the gyre.

The third chapter of this thesis develops the water mass framework in temperature and salinity coordinates, which is applied to observations of temperature and salinity across Drake Passage. Seasonal variations in the distribution of water masses reveal the imprint of the Southern Ocean overturning. This highlights the importance of seasonally varying

air-sea fluxes in the winter-time formation of intermediate water at the expense of deep water, winter water and surface water.

The fourth chapter of this thesis extends the analysis of the third chapter to the entire Southern Ocean using an ocean state estimate and an observationally based seasonal climatology. This reveals a diabatic pathway for the upwelling and conversion of deep water into intermediate water. Deep water is first cooled and freshened during the winter through mixing with overlying winter water. The distribution of this modified deep water in temperature/salinity space and its maximum density suggests the process of cabbeling is important in the upwelling of this deep water. Sea ice-melt and surface heating then warm and freshen this seasonally formed water mass to create intermediate water during the summer months. This mechanism and the conventional view of intermediate water formation through winter time cooling north of the polar front combine to give a double peak in the seasonal cycle of intermediate water volume. These results suggest that the process of cabbeling could be a rate determining step in the global overturning circulation and the upwelling of deep waters formed in the high latitude North Atlantic.

To assess the effect that interpolating Argo data onto a regular geographical grid has on the water mass framework, the fifth chapter of this thesis explores the potential to develop an alternative method to determine a volumetric distribution using individual Argo profiles. The volumetric distribution determined using this profile based estimate is compared to the distribution calculated using a geographically interpolated dataset. This comparison reveals that the interpolation scheme used to geographically grid Argo appears to artificially mix water masses toward the centre of the distribution. The thesis is concluded in the final chapter.

Chapter 2

Recent Wind Driven Changes in the Atlantic Meridional Overturning Circulation

In review: Dafydd Gwyn Evans, John Toole, Gael Forget, Jan D. Zika, Alberto C. Naveira Garabato, A. J. George Nurser, and Lisan Yu. Recent wind-driven changes in the Atlantic meridional overturning circulation. *Journal of Physical Oceanography.* **All work in this chapter was done by myself.**

Abstract

Interannual variability in the volumetric water mass distribution within the North Atlantic subtropical gyre is described in relation to variability in the Atlantic Meridional Overturning Circulation. The relative roles of diabatic and adiabatic processes in the volume and heat budgets of the subtropical gyre are investigated by projecting data into temperature coordinates as volumes of water using an Argo based climatology and an ocean state estimate (ECCO v4). The use of a single tracer, in the form of temperature, suitably captured the large scale variations in the water mass volume distribution. This highlights that variations in the subtropical gyre volume budget are predominantly set by transport divergence in the gyre. A strong correlation between the volume anomaly due to transport divergence and the variability of both thermocline depth and Ekman pumping over the gyre suggests that wind-driven heave drives transport anomalies at the gyre boundaries. This wind-driven heaving contributes significantly to variations in the heat content of the gyre, as do anomalies in the air–sea fluxes. The analysis presented here suggests that wind forcing plays an important role in driving interannual variability in the Atlantic meridional overturning circulation, and that this variability can be unraveled from spatially-distributed hydrographic observations using a water mass framework.

2.1 Introduction

The Atlantic meridional overturning circulation (AMOC) is commonly defined in the depth-latitude plane as the large-scale hemispheric exchange of northward-flowing warm and saline surface waters with compensating southward-flowing cold and fresh deep waters (Talley, 2013). The resultant northward heat transport within the North Atlantic affects both the long-term climatic state over northern Europe (Trenberth and Caron, 2001; Johns et al., 2010), and the interannual climate variability across the North Atlantic basin (Maidens et al., 2013). This interannual variability can be very pronounced. In 2009-2010 for example, an observational estimate at 26°N revealed a temporary reduction in the AMOC strength from a mean of 18.5 Sv (2004–2009) to 12.8 Sv between 2009 and mid-2010 (1 Sv=1×10^6 m^3s^{-1}) (McCarthy et al., 2012a). It remains unclear whether this change occurred due to local atmospheric forcing anomalies (Roberts et al., 2013; Buckley et al., 2014; Yang, 2015), or through remotely forced changes in the overturning (Cunningham et al., 2013; Sonnewald et al., 2013; Bryden et al., 2014).

Understanding the relative roles of atmospheric forcing and intrinsic ocean dynamics in the heat and salt budgets of the North Atlantic Ocean requires a careful separation of many processes that often feed back on each other. The role of the atmosphere is often divided between the long-term impact of buoyancy forcing due to air-sea fluxes of heat and freshwater, and the action of winds on the sea-surface (Polo et al., 2014; Forget and Ponte, 2015). The ocean circulation can adjust to the latter on short time scales (days to months) through barotropic dynamics (Willebrand et al., 1980; Andres et al., 2011, 2012), and on longer timescales (years to decades) through various baroclinic modes (Anderson and Gill, 1975; Williams et al., 2013; Forget and Ponte, 2015). Both processes affect the ocean by altering its circulation meridionally and zonally. The forced oceanic responses can propagate to remote locations through boundary or Kelvin waves along the equator and ocean margins, and through the interior as westward-propagating Rossby waves (Johnson and Marshall, 2002; Forget and Ponte, 2015). The action of the wind on the sea-surface may also affect circulation changes by driving near surface advection and enhancing near-surface mixing.

Here, we investigate the drivers of interannual AMOC variability as defined and measured using mooring based arrays. We use a water mass analysis framework (Walin, 1982; Speer and Forget, 2013; Evans et al., 2014; Zika et al., 2015), in which we project data from a gridded Argo product (Roemmich- Gilson Argo climatology: RGAC; Roemmich and Gilson, 2009) and an ocean state estimate (Estimating the Circulation and Climate of the Ocean version 4: ECCO v4; Forget et al., 2015) onto temperature coordinates (Evans et al., 2014). Using this framework, we quantify interannual variations in water mass inventories of the subtropical gyre. The averaging and smoothing required to produce monthly gridded data sets (RGAC and ECCO v4) mitigates the impact of aliased variability associated with mesoscale eddies (e.g., see Forget et al., 2011). We

then assess the extent to which water mass volume changes are driven by air-sea exchanges of heat (Speer, 1993) using various air-sea flux products (ECCO v4, Kalnay et al., 1996; Yu et al., 2006; Dee et al., 2011). We further use ECCO v4 to determine the contributions from lateral transports to water mass inventory changes between 26°N and 45°N and go on to assess the relationship between those transport variations and perturbations in the wind-stress curl (Dee et al., 2011; Yu and Jin, 2014) during the same period.

In this chapter, we show that interannual AMOC variability at 26°N is associated with changes in water mass inventories in the subtropical Atlantic. We describe the data and methods used for this chapter in section 2.2. In sections 2.3 and 2.4, we use the water mass transformation framework to show that the variability in the water mass volume of the subtropical North Atlantic is primarily driven by adiabatic changes in the circulation of the subtropical gyre in response to anomalous wind-stress curl in the region. However, some fluctuations in heat content anomaly cannot be explained entirely by adiabatic processes, but require a diabatic contribution through air-sea fluxes of heat. In section 2.5 we present evidence that suggests local wind forcing drives much of the observed interannual variability in the AMOC, and discuss the potential for monitoring this variability with basin-scale hydrographic observations.

2.2 Data and Methods

2.2.1 Data

This chapter uses gridded hydrographic observations, a mooring-based AMOC estimate, a full ocean state estimate and atmospheric reanalyses products to understand the diabatic and adiabatic contributions to water mass variability in the subtropical North Atlantic. From each product we therefore use data between the latitudes of 26°N and 45°N in the North Atlantic. The gridded hydrographic observations are the Roemmich–Gilson Argo climatology (RGAC; Roemmich and Gilson, 2009) accessed at http://sio–argo.ucsd.edu/RG_Climatology.html. In this monthly product the temperature and salinity data are gridded horizontally using objective analysis on a 1–degree grid and vertically at intervals of 10m at the surface increasing to 50m at the maximum depth of 1975m. From these monthly maps we calculate the conservative temperature (units=°C) and absolute salinity (units=g kg^{-1}) according to TEOS-10 (IOC et al., 2010). To mitigate the effect of water adiabatically heaving across the base of the RGAC domain, our calculation of volume in temperature classes only includes water lighter than $\sigma_0 = 27.7$ in RGAC. In our domain, this surface is never deeper than 1975m. This ensures that the only adiabatic volume changes we observe are those due to transport changes across 26°N and 45°N.

We also use monthly potential temperature and salinity from the Estimating the Circulation and Climate of the Ocean version 4.11 (ECCO v4) state estimate accessed at http://www.ecco–group.org that closely fit Argo data (Forget et al., 2015). This dataset further provides velocity, transport and surface flux estimates that are dynamically consistent with the estimated hydrography. Throughout, we will refer to conservative temperature (from RGAC) and potential temperature (from ECCO v4) as Θ, and absolute salinity (RGAC) and practical salinity (ECCO v4) as S.

We rely on complementary data sets to verify our interpretation of the results. An estimate of the AMOC strength and variability at 26°N is obtained from the RAPID-WATCH MOC monitoring project (Smeed et al., 2015). We use monthly mean fields for shortwave radiation, longwave radiation, sensible heat flux and latent heat flux from the NCEP/NCAR (Kalnay et al., 1996) and ERA-interim (Dee et al., 2011) reanalyses to calculate net air–sea heat flux. These have horizontal resolutions of ∼1.9° and 0.75° respectively. We obtain sea surface temperature (SST; resolution of 1°) from the NOAA optimally interpolated SST product (hereinafter 'Reynolds–SST') as described in Reynolds et al. (2004). For the calculation of wind-stress curl we use the WHOI OAFlux project (Yu and Jin, 2014) wind-stress products calculated using the COARE 3.0 algorithm, which has a horizontal resolution of 0.25°.

It is worth noting that the output ECCO v4 is constrained using Argo profiles, therefore the Θ and S fields from ECCO v4 and RGAC are not independent. However, ECCO v4 does not use RAPID-WATCH MOC estimates which encompass Florida Straits transport estimates and scatterometry data. The transport estimates from ECCO v4 and RAPID-WATCH may therefore be considered independent.

2.2.2 Calculation of water mass volume and diathermal transformations

The methods described here are based on the water mass framework of (Walin, 1982) applied to a time varying ocean (Evans et al., 2014; Zika et al., 2015). The volume of water colder than a particular isotherm Θ^* is defined by

$$V(\Theta^*) = \iiint \Pi(\Theta^* - \Theta)\mathrm{d}x\mathrm{d}y\mathrm{d}z \tag{2.1}$$

where $\Pi(x)$ is a Heaviside function that is 0 when $x < 0$ and 1 when $x \geq 0$. In practice x, y are transformed into spherical polar coordinates. The volume per unit Θ, the volumetric distribution, is simply $\partial V/\partial\Theta$. We determine the volumetric distribution in the Atlantic between 26°N and 45°N for each month using a nominal grid spacing $\Delta\Theta$ of 0.5°C.

The volume, V is set in part by the inflow of water at the boundaries of the domain (e.g. 26°N and 45°N) defined by

$$M(\Theta^*) = \iint \Pi(\Theta^* - \Theta) v \mathrm{d}y^\dagger \mathrm{d}z \tag{2.2}$$

where v is the velocity component normal to the domain boundary and $y^\dagger$ is the horizontal dimension running along the domain edge (Ferrari and Ferreira, 2011; Forget et al., 2011). This is the adiabatic component of the water mass inventory. Diathermal transformations across surfaces of constant Θ represent the diabatic contribution to the inventory. These diathermal transformations are the integral of the dia–thermal velocity crossing a given iso-thermal surface (surface of constant Θ):

$$U(\Theta^*) = \int_{\Theta=\Theta^*} \frac{1}{|\nabla\Theta|}\frac{\partial\Theta}{\partial t} + \mathbf{u}\cdot\frac{\nabla\Theta}{|\nabla\Theta|}\mathrm{d}A \tag{2.3}$$

where $\int_{\Theta=\Theta^*} \mathrm{d}A$ is the area integral over the surface where $\Theta = \Theta^*$ and $\mathbf{u}$ is velocity. The budget for V is then

$$\frac{dV}{dt} = M - U \tag{2.4}$$

Practically diagnosing the adiabatic (M) and diabatic (U) contributions to the inventory change from velocity measurements is difficult. In practice these are therefore determined from changes in the volumetric distribution of water in Θ coordinates. We solve for the monthly diathermal transformations across each isotherm as described in Evans et al. (2014) from the monthly changes in the Θ volumetric distribution by building a series of linear equations to describe the volume change in each Θ class in terms of the unknown diathermal transformations across each isotherm. Diathermal ransformations are presented in units of Sverdrups (Sv; 1 Sv = 1×10^6 m^{3}s^{-1}). The diathermal transformation across an individual isotherm describes the amount of water that changes temperature by $\Delta\Theta$. As a whole, the divergence of these diathermal transformations represent volume change that most closely matches the observed volume changes within each temperature class. They therefore do not necessarily describe the actual path of water through Θ coordinates, but instead the net change indicated by the change in the volumetric distribution. The volume changes implied by air–sea heat fluxes are discussed in the next section.

It should be expected that instrumental and sampling errors would affect the volumetric distributions and diathermal transformations calculated as part of this study. Specifically, aliasing of eddy heave may increase the sampling error associated with our results. In an attempt to quantify such sampling errors we randomly impose a heave of either -30m or +30m to each grid point and time–step in RGAC, but uniformly to all depths for each grid point. Therefore, a given grid point at (x, y) and a heave of 30m for example,

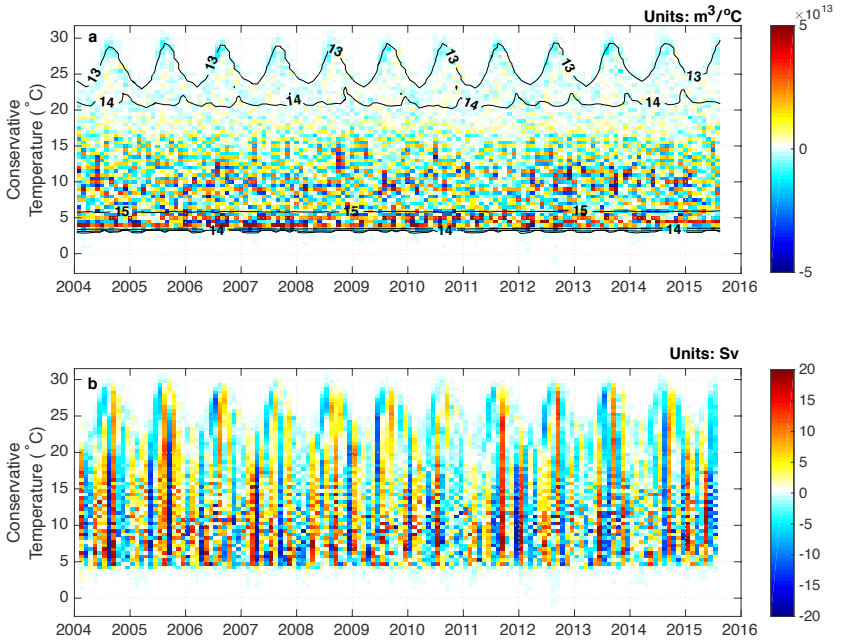

Figure 2.1: (a) Black contours represent a time-series of $\log_{10}$ water mass volume (in $m^3/°C$) from RGAC with no artificially added error. Colours show the difference between the volume shown by the black contours and the volume calculated with a random vertical heave of either -30m or +30m added to the measurements of Θ. Units are $m^3/°C$. (b) Difference between the diathermal transformations calculated using the volume estimates determined with and without artificially added error. Units: Sv (1 Sv= 1×10^6 m^3s^{-1}).

$\Theta(x, y, z, t)$ becomes $\Theta(x, y, z + 30m, t)$. We don't decrease the heave to zero at the surface, as this simple approach serves to illustrate the affect of heave, while only imposing a small bias to the surface Θ/S classes. We then calculate the water mass volumes and the resultant diathermal transformations and subtract them from those calculated without the artificially added heave (Figure 2.1). The induced error in water mass volume is an order of magnitude less than the variability in water mass volume (black contours in Figure 2.1). The added eddy heave does however generate (non-diabatic) variability in the inferred diathermal transformations, which are relatively large. A similar check using a representative instrumental error had a limited impact on the calculated water mass volumes and diathermal transformations.

2.2.3 Calculation of dia–surface transformations due to air/sea fluxes

Using a method similar to Speer (1993) and Evans et al. (2014) we calculate the diathermal transformations implied by air–sea fluxes of heat over our domain. The total heat

flux into water colder than Θ^* is defined by

$$F_\Theta(\Theta^*) = \iint \Pi(\Theta^* - \Theta)\, Q_{net}\, \mathrm{d}x\mathrm{d}y \tag{2.5}$$

where Q_{net} is the net surface heat flux (W m^{-2}). The diathermal transformation rate due to the air–sea heat flux is then

$$U_{Air-Sea} = \frac{1}{\rho C_p} \frac{\partial F_\Theta}{\partial \Theta} \tag{2.6}$$

where ρ is the density and C_p is the specific heat capacity of seawater. Again, data in the Atlantic between 26°N and 45°N are selected and discrete temperature intervals of $\Delta\Theta = 0.5$°C are used. To avoid the uncertainty due to Argo's irregular data coverage we use Reynolds SST maps rather than RGAC when computing F_Θ. Heat fluxes are determined using both NCEP/NCAR, ERA-Interim reanalyses and ECCO v4.

2.2.4 Calculation of the volume change due to the divergence of transport in the subtropical gyre

We calculate the volume change in Θ coordinates due to transport changes using fields for velocity and Gent-McWilliams (Gent and McWilliams, 1990) bolus transport from ECCO v4. The contribution due to resolved sub-monthly variations in velocity and temperature are neglected and would be important at eddy permitting resolution. We consider transects of Θ and the total meridional transport per grid cell at 26 and 45°N, and calculate the total volume change (divergence of monthly mean transport divided by monthly time interval) for each Θ class. From these volume changes we then determine the implied volume fluxes between Θ classes as described above for the total volume change.

Wunsch and Heimbach (2013b) show that ECCO v4 simulates well the magnitude and variability of the Eulerian RAPID-WATCH AMOC estimate, although with a slightly reduced range of variability. Here we define the Eulerian overturning circulation in ECCO v4 as the transport at the depth of maximum $\Psi_z(z^*) = \int\int_\eta^{z^*} v\, dx\, dz$, where v is the meridional component of velocity and η is the sea surface. Further, Ψ_z is displayed with units of Sv. The depth of maximum Ψ_z occurs at approximately the same depth as the 6°C isotherm. This isotherm also marks a transition in the structure of thermohaline volume change due to transport across 26°N and 45°N, as is discussed below. A comparison of the time-series (Figure 2.2) reveals the good agreement between the AMOC estimates with a correlation coefficient of 0.68 through the overlapping period from 2004-2011 (significant at 95% confidence interval).

Also shown in Figure 2.2 is the time–mean (1992-2012) water mass volume change from ECCO v4 within the chosen domain due to the divergence of transport across 26°N

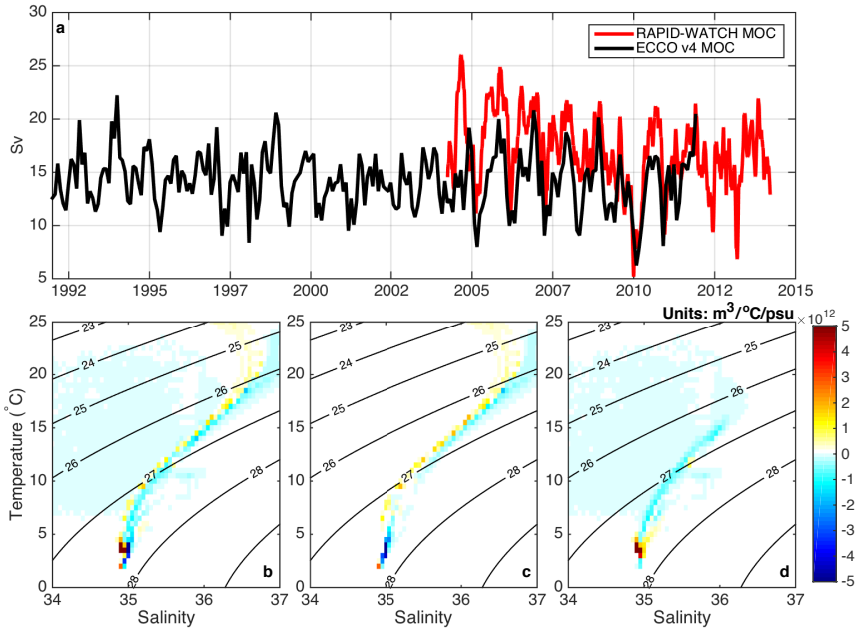

Figure 2.2: (a) RAPID-WATCH AMOC estimate (red line) and ECCO v4 AMOC at 26°N. Units: Sv (1 Sv= 1×10^6 m^3s^{-1}). (b) ECCO v4 time-mean (1992–2012) transport divergence in Θ/S coordinates for the region between 26°N and 45°N, divided by monthly time interval to give volume change. Units: $m^3/°C$ psu. (c) ECCO v4 volume change in thermohaline coordinates for the region north of 26°N implied by the time-mean (1992–2012) transport at this latitude. Units: $m^3/°C/psu$. (d) Volume change in thermohaline coordinates for the region south of 45°N implied by the time-mean (1992–2012) transport at this latitude. Units: $m^3/°C/psu$.

and 45°N, and the contribution towards the volume change due to the net transports across the individual sections. These are plotted against Θ and S to better highlight the meridional and zonal structure of the subtropical gyre (hereinafter 'the gyre') captured by this projection, providing context for the discussion in the following sections.

This adiabatic volumetric change implied by the lateral transport across our domain's boundaries in ECCO v4 implies the following. At 26°N, at Θ>6°C, the lateral transport reflects the circulation of the gyre, with warmer/fresher water entering the domain in the west and cooler/saltier water leaving the domain in the ocean interior. Using only this volume change to compute U would give a positive (but adiabatic) volume flux of cold into warm water. At Θ<6°C, deep water leaving the domain imprints as a loss of cold water, also implying a positive volume flux. In contrast, at 45°N, loss of warmer waters to the north at Θ>6°C is opposed by a southward transport of cold, deep water at Θ<6°C, thereby inducing an apparent volume flux of warm water into cold water to the south of 45°N.

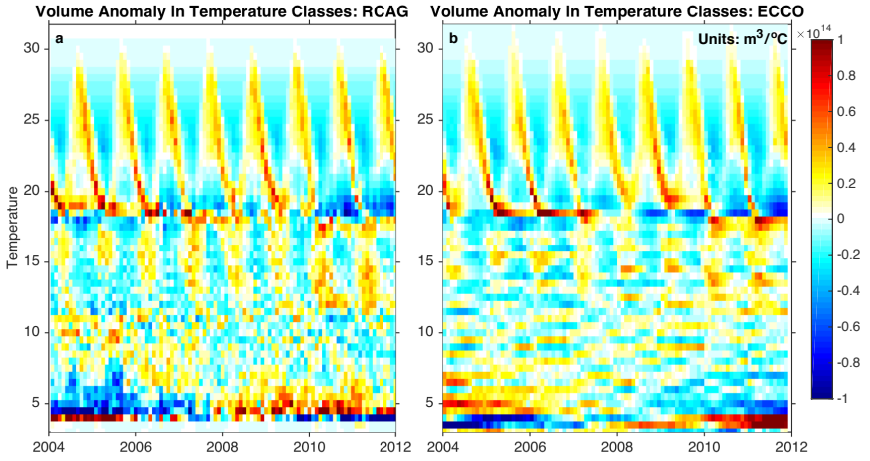

Figure 2.3: (a) Volume anomaly in Θ classes with respect to the time-mean for the period shown from RGAC in the North Atlantic between 26 and 45°N. Units are $m^3/°C$. (b) Volume anomaly in Θ classes with respect to the time-mean for the period shown from ECCO v4 in the North Atlantic between 26 and 45°N. Units are $m^3/°C$.

2.2.5 Calculation of Ekman pumping

We calculate Ekman pumping as the vertical component of the curl of the wind-stress divided by a reference density ($\rho = 1000$ kg m^{-3}) and f, the Coriolis parameter, assuming an ocean at rest. We thus obtain estimates of monthly vertical displacements from OAFlux.

2.3 Diabatic and adiabatic contributions to water–mass volume variability in the Subtropical Gyre

First we explore the variability of water mass volume within Θ classes. A time series of the volumetric distribution in temperature classes highlights both the seasonal variation in the water mass inventory at Θ>10°C and interannual changes over the entire temperature range (Figure 4.2(a) and (b)). In both RGAC (left) and ECCO v4 (right) data, we see a seasonal exchange of volume between the warmer surface waters (Θ>18°C) and mode/central waters (Θ between 10 and 18°C). This seasonal variability is imprinted on interannual changes in the water masses with the largest volume: subtropical mode water (STMW; Θ∼18°C), North Atlantic Central Water (NAW; Θ∼12°C) and North Atlantic Deep Water (NADW; Θ∼5°C). It is the diabatic and adiabatic contributions to this interannual variability we aim to characterise. Differences between the ECCO v4 and RGAC analyses at Θ<10°C are the result of excluding water denser than $\sigma_0 = 27.7$ in RGAC. During the winter of 2009/10, over a period of 3 months the volume above the permanent thermocline (and depth of maximum overturning; Θ>6°C) in both RGAC

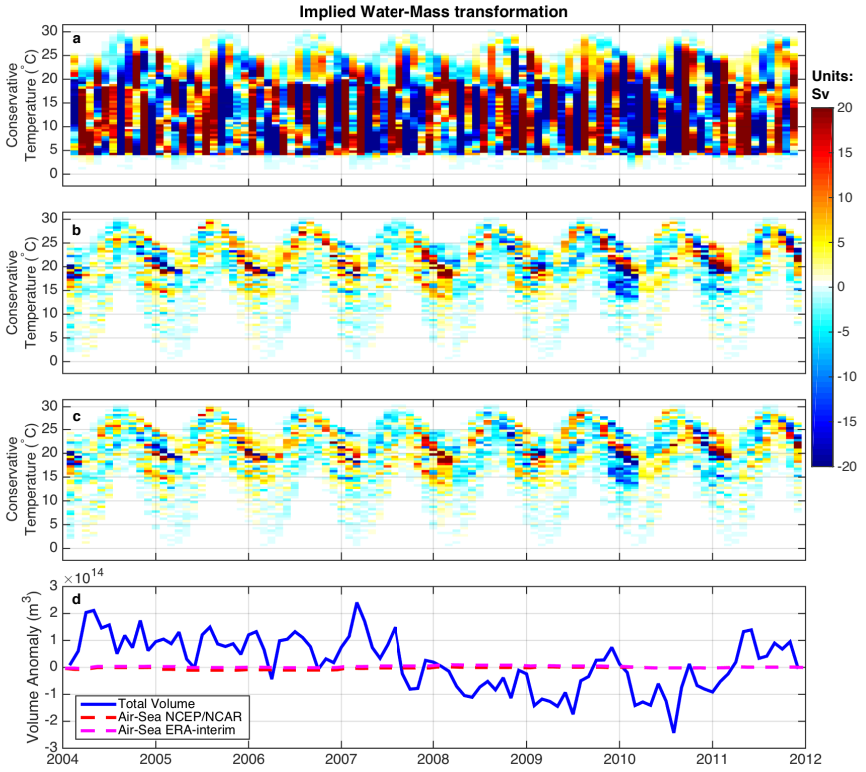

Figure 2.4: (a) Implied water mass diathermal transformation anomalies with respect to the monthly-mean (2004–2012) to remove the mean seasonal cycle. Diathermal transformations were calculated using the month to month change in volumetric distribution from RGAC. (b) Diathermal transformation anomaly with respect to the monthly-mean (2004–2012) inferred from NCEP/NCAR air-sea heat fluxes. (c) Diathermal transformation anomaly with respect to the monthly-mean (2004–2012) inferred from ERA-Interim air-sea heat fluxes, determined using Reynolds surface Θ. Units: Sv (1 Sv$= 1 \times 10^6$ m^{3}s^{-1}). (d) Volume anomaly (V') for temperatures greater than 6°C. Units: m^3.

and ECCO v4 dropped by approximately 2–3$\times 10^{14}$ m^3, equivalent to a transport of 25 Sv. This is indicative of the occurrence of either a diathermal transformation of warm to cold water, or an adiabatic re-arrangement of water masses associated with an export of upper-ocean waters and an import of deep waters across the domain boundaries.

The relative roles of diabatic and adiabatic processes may be assessed by determining the diathermal transformation of water between temperature classes required to explain the changes in volume shown in Figure 4.2 (a) and (b) (RGAC: Figure 2.4 and ECCO v4: Figure 2.5). The diabatic contribution to this variability is determined using air-sea heat flux products from NCEP/NCAR (Figure 2.4(b)), ERA-interim (Figure 2.4(c) and ECCO v4 (Figure 2.5(b)). The adiabatic component of change is inferred from the divergence of lateral transports across 26°N and 45°N in ECCO v4 (Figure 2.5(c)). In

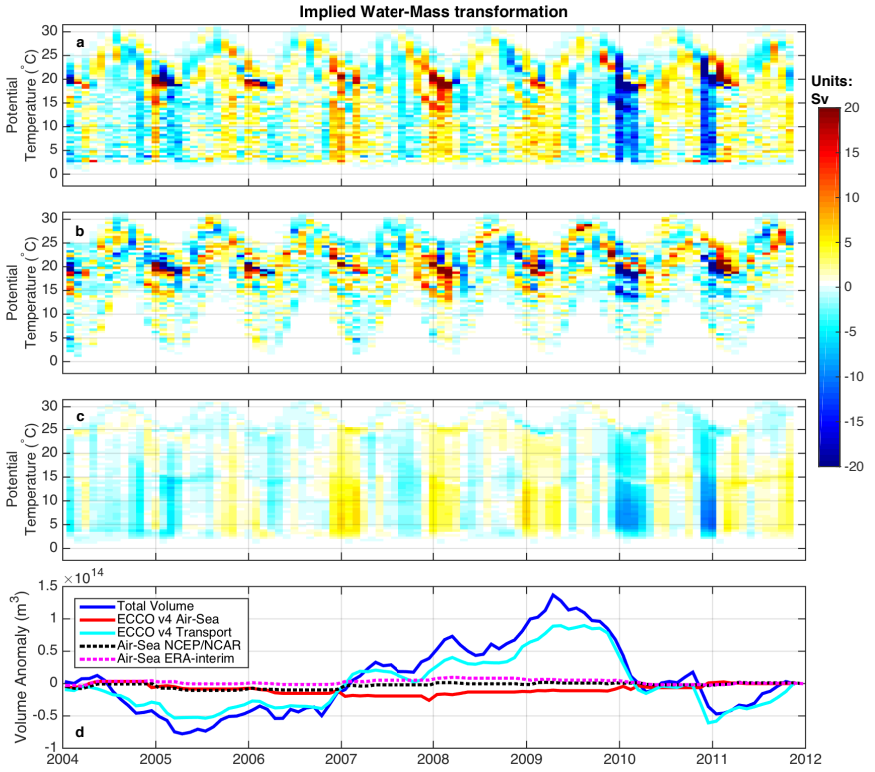

Figure 2.5: (a) Implied diathermal transformation anomalies with respect to the monthly-mean (2004–2012) to remove the mean seasonal cycle. Diathermal transformations were calculated using the month to month change in volumetric distribution from ECCO v4. (b) Diathermal transformation anomaly with respect to the monthly-mean (2004–2012) inferred from ECCO v4 air-sea heat fluxes. (c) M anomaly (see (2.2)) with respect to the monthly-mean (2004–2012) implied by the divergence of transport between 26 and 45°N in ECCO v4. Units: Sv (1 Sv= 1×10^6 m^{3}s^{-1}). (d) Volume anomaly (V') for temperatures greater than 6°C. Units: m^3.

all cases positive values indicate cold water being replaced with warm water within the domain of study.

Removing the mean seasonal cycle unveils substantial interannual variability in Figures 2.4 and 2.5. Variability in the anomalous diathermal transformations inferred from the RGAC water mass volume fluctuations are however dominated by noise (Figure 2.4). As discussed in section 2.2.2, this may be a consequence of aliased eddy heave. The remaining time-series, and in particular ECCO v4 (Figure 2.5(a)) contain anomalously negative signals during the winters of 2009/10 and 2010/11. Such a signal is suggestive of either intensified wintertime cooling or the introduction of excess cold water into our study region across its northern or southern boundaries at those times. Intensified wintertime cooling is consistently seen in diathermal transformation rates computed from

Figure 2.6: (a) The volume flux due to M (from Figure 2.5(c)), integrated at 6°C. This gives the volume anomaly (i.e. V') for temperatures greater than 6°C due to the variability in transport at 26°N and 45°N (solid cyan line). The dashed cyan line is determined using the transport at 26°N and the dotted cyan line is determined using the transport at 45°N. AMOC monthly-mean anomaly (2004-2012), estimated from RAPID-WATCH (magenta line) and from ECCO v4 (i.e. Ψ_z) at 26°N and 45°N (dashed and dotted grey lines respectively). Units: m^3. (b) Time-integrated diathermal transformations (blue, red, black and magenta lines; from Figures 2.4 and 2.5), integrated through all temperatures greater than 6°C, giving heat content anomaly (H'). Time-integrated M (cyan lines), integrated through all temperatures greater than 6°C, giving heat content anomaly. Positive gradient indicates warming in the upper ocean Units: J.

NCEP/NCAR, ERA-Interim and ECCO v4 surface heat fluxes for temperatures between 15 and 20°C (Figure 2.4(b)/(c) and Figure 2.5(b) respectively). However the adiabatic component (i.e., M) computed from ECCO v4 (Figure 2.5(c)) displays prominent negative anomalies at all temperatures, and in fact explains the bulk of the volumetric census anomalies seen in the winters of 2009/10 and 2010/11 particularly at Θ<15°C (Figure 2.5(a)). The relative roles of diabatic forcing at Θ>15°C and adiabatic forcing through all Θ are consistent throughout the time-series.

The anomalous diathermal transformations due to air–sea fluxes, and volume fluxes due to transport displayed in Figure 2.4(a)-(c) and Figure 2.5(a)-(c) can be represented as volume changes by integrating with respect to time (Figure 2.4(d) and Figure 2.5(d)):

$$V'(t) = \int (M - U_\Theta)\, dt. \tag{2.7}$$

By Gauss' theorem, this gives the volume change in the ocean warmer than 6°C when these diathermal transformations and volume fluxes are integrated at $\Theta = 6$°C. As discussed in section 2.2.4, Θ=6°C represents the transition between the upper and deep ocean. Therefore, in Figure 2.4(d) and Figure 2.5(d) a negative (positive) slope represents the volume loss (gain) in the upper ocean. In Figure 2.4(d) we compare this volume anomaly from the RGAC data (blue line) to the volume anomaly implied by NCEP/NCAR (red dashed) and ERA-interim (magenta dashed). In Figure 2.5(d) we compare the volume anomaly from ECCO v4 (blue line) to the volume anomaly implied by the transport divergence in ECCO v4 (cyan line) and to the air-sea heat fluxes from ECCO v4 (red line), NCEP/NCAR (red dashed) and ERA-interim (magenta dashed). This further highlights the dominant role of the adiabatic term in setting the distribution of volume in Θ classes within the gyre. The RGAC data is again dominated by noise making it difficult to assess the variability shown in Figure 2.4(d).

The adiabatic term, driven by the divergence of transport at the boundaries of our domain, can be separated into its components at 26°N (cyan long dashed) and 45°N (cyan short dashed; Figure 2.6(a)) in ECCO v4. The implied volume anomalies evaluated at $\Theta = 6$°C compare well with the AMOC integrated over time in RAPID-WATCH (magenta) and ECCO v4 at 26°N (grey long dashed) and 45°N (grey short dashed). There are some differences between the RAPID-WATCH volume anomaly and the adiabatic volume term from ECCO v4 (solid cyan), because the latter includes changes due to transport at both 26°N and 45°N. There is also disagreement between the adiabatic volume term based on the transport at 45°N (short dashed cyan) and the ECCO v4 overturning at 45°N (short dashed grey) during 2009, which may be due to the way these terms are calculated. Importantly the good agreement between the magenta and cyan lines in Figure 2.6(a) reveals the importance of the transport variability at 26°N in determining the volume budget of the gyre between 26°N and 45°N.

The diabatic air–sea heat flux term and the adiabatic transport term can be described in terms of the upper ocean heat content by integrating the volume anomaly from (2.7) at each isotherm across all temperatures greater than 6°C as follows:

$$H'|_{\Theta>\Theta^*} = \rho_0 c_p \int_{\Theta^*}^{\infty} V' \, d\Theta, \tag{2.8}$$

where ρ_0 is a reference density and c_p is the (constant) specific heat capacity of water. Here, heat content anomaly H' has units of Joules. This unconventional estimate of the heat content provides an interpretation of the large scale heat content changes within the water mass framework (for a similar analysis see Palmer and Haines, 2009). Time-series of H' are shown in Figure 2.6(b) from the total volume changes in ECCO v4 (blue line), the transport divergence in ECCO v4 (cyan lines) and the air-sea heat fluxes from ECCO v4 (red line), NCEP/NCAR (red dashed) and ERA-interim (magenta dashed). The large dashed and small dashed cyan lines show the contributions to H' in ECCO

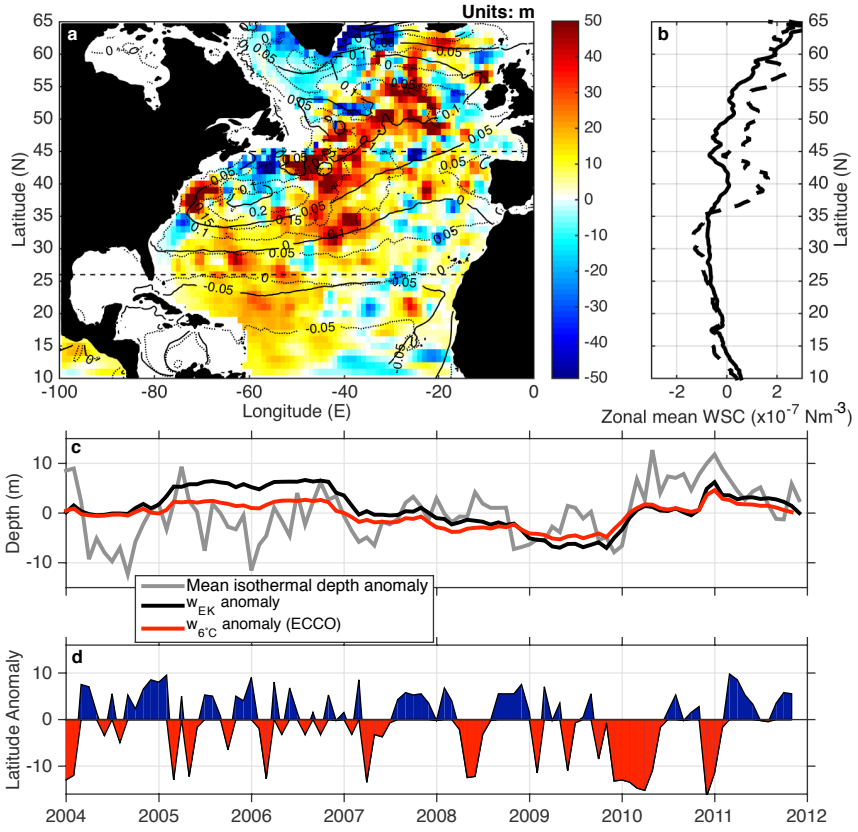

Figure 2.7: (a) Colours represent depth anomaly (with respect to the monthly-mean for 2004–2012) of the 6°C isotherm from RGAC, averaged over March 2010 to November 2010. Red indicates a shoaling and blue indicates a deepening. Units: m. Solid contours indicate the time-mean (2004-2008) zonal wind-stress (units: N m^{-2}) and dotted contours show the zonal wind-stress averaged over November 2009 to March 2010 from OAflux. (b) Zonal mean wind-stress curl averaged over 2004-2008 (solid black curve) and November 2009 to March 2010 (dashed curve), from OAflux. Units: N m^{-3}. (c) Depth anomaly (with respect to the monthly-mean for 2004-2012) of the 6°C isotherm averaged over 26 and 45°N from RGAC (grey). Time-integrated vertical Ekman velocity anomaly (with respect to the monthly-mean for 2004-2012) from OAflux (black). Time-integrated vertical velocity anomaly (with respect to the monthly-mean for 2004–2012) at the 6°C isotherm from ECCO v4 (red). Units: m. (d) Latitude of maximum zonal wind-stress with monthly-mean removed. Units: Degrees.

v4 by transports at 26°N and 45°N respectively. A negative (positive) slope represents a cooling (warming) in the upper ocean.

In the discussion below, all correlations are significant at the 95% confidence interval during the displayed time-frame of 2004–2012. According to ECCO v4, diabatic air-sea fluxes and adiabatic advection play a roughly equal role in setting the variability of H' with correlations of $r = 0.96$ and $r = 0.88$ respectively. Variability in transport at

26°N correlates more strongly with the adiabatic contribution to H' ($r = 0.96$) than the transport at 45°N ($r = 0.73$). Between 2004 and 2012 the standard deviation of the total H' (blue line; 2.9×10^{21}J) is mostly determined by the advective term, which has a standard deviation of 1.7×10^{21}J. Differences between the sum of the air-sea flux and advective terms and the total H' allude to the contribution of mixing, but some of this difference may also be due to an insufficient temporal resolution since we use monthly fields in our computations.

The contribution of the adiabatic advective terms in Figure 2.5 and Figure 2.6 to the negative anomalies during the winters of 2009/10 and 2010/11 suggests that a lateral rearrangement of water masses across the mid-latitude North Atlantic was predominantly responsible for the abrupt, short-term decline in the AMOC at 26°N during these winters. At 26°N, the negative volume flux anomalies in Figure 2.5(a)-(c) and the negative slope of the cyan dashed curve in Figure 2.6(a) imply a reduction in the upper-ocean exchange of warm/fresh and cold/salty water driven by the gyre circulation and an increased transport in the deep ocean (Figure 2.2 and section 2.2.4). At 45°N, the negative volume flux anomalies in Figure 2.5(a)-(c) and the negative slope of the cyan dotted curve in Figure 2.6(a) suggest an increase in both the northward transport of warm water and/or southward transport of cold water in the winter of 2009/2010. The combination of anomalous transports at 26°N and 45°N yields an adiabatic volumetric change due to a divergence above the thermocline and a convergence below, consistent with our inferred volumetric changes (Figure 4.2) and with the negative anomalies in Figure 2.5.

2.4 Mechanisms of adiabatic water mass variability during 2009/10 and 2010/11

The most plausible driver of such a rapid perturbation in the lateral transport through the boundaries of our study region is a change in wind forcing. We consider the relative configuration of the wind-stress and ocean circulation over our region of interest during the winter of 2009/10. This is illustrated by Figure 2.7(a), which shows the anomalies in the depth of the 6°C isotherm in March–November 2010 according to RGAC (colour) and in the zonal wind-stress during November 2009–March 2010 according to OAFlux (dotted contour), as well as the time mean (2004-2008) zonal OAFlux wind-stress (solid contour). During the period of reduced AMOC, a southward shift in the zonal wind-stress maximum (Figure 2.7(d)) precedes a general shoaling of the 6°C isotherm between 26°N and 45°N. The southward shift of the wind affects the meridional profile of wind-stress curl, generating anomalously positive curl between 35°N and 45°N and anomalously negative curl between 26°N and 35°N (Figure 2.7(b)).

These changes in isotherm depth and the wind-stress over the entire gyre (i.e. 10°N to 45°N) suggests that the wind-driven gyre circulation shifted south in response to the

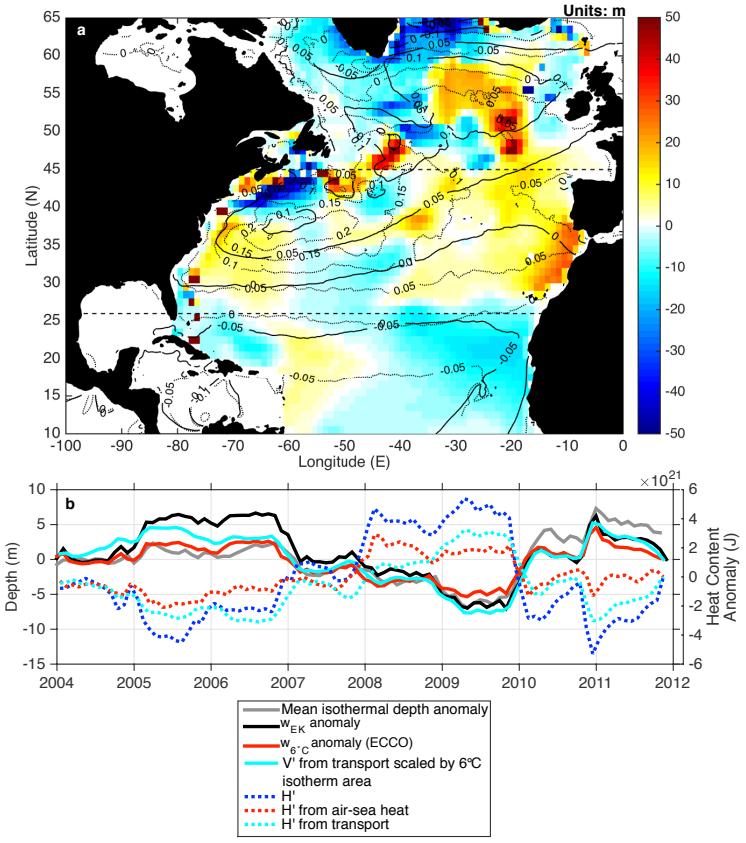

Figure 2.8: (a) Colours represent depth anomaly (with respect to the monthly-mean for 2004–2012) of the 6°C isotherm from ECCO v4, averaged over March 2010 to November 2010. Red indicates a shoaling and blue indicates a deepening. Units: m. Solid contours indicate the time-mean (2004-2008) zonal wind-stress and dashed contours show the zonal wind-stress (N m^{-2}) averaged over November 2009 to March 2010 from OAflux. (b) Depth anomaly (with respect to the monthly-mean for 2004-2012) of the 6°C isotherm averaged over 26 and 45°N from ECCO v4 (grey). Time-integrated vertical Ekman velocity anomaly (with respect to the monthly-mean for 2004-2012) from OAflux (black). Time-integrated vertical velocity anomaly (with respect to the monthly-mean for 2004-2012) at the 6°C isotherm from ECCO v4 (red). Volume anomaly (V') from ECCO v4 transport divergence (from Figure 2.6(a)) scaled by the surface area of the 6°C isotherm (cyan). Units: m. Dashed lines are the similarly coloured solid lines of heat content anomaly shown in Figure 2.6(b).

changing wind field. During the winter of 2009/10, the change in thermocline depth induced by Ekman pumping implied by the wind-stress curl anomaly, averaged between 26°N and 45°N, shows a shoaling similar to the observed isotherm depth anomaly averaged over the same region (Figure 2.7(c)). But in general the agreement between time-series is poor, with a fairly low correlation coefficient of $r = 0.27$. This may be related to the sparsity of data earlier in the Argo time-series. Note that the southward shift of the westerlies over the mid-latitude North Atlantic in the winter of 2009/10 was uniquely prolonged during our study period and preceded the shoaling of the 6°C

isotherm (Figure 2.7(d)).

The spatial pattern of the 6°C isotherm depth anomaly is similar in ECCO v4 (Figure 2.8(a)), as is the magnitude of the average isotherm depth change (Figure 2.8(b)). These similarities are evident along the boundaries of the domain and in the subpolar ocean. Through the interior of the subtropical ocean, the shoaling in RGAC is greater. Further, in ECCO v4 there is deepening of the 6°C isotherm to the south of 26°N, not entirely replicated by RGAC. These differences may be a consequence of poor Argo profile coverage. The spatial pattern of isotherm depth in RGAC also seems to alias some mesoscale eddy variability, which is not present in ECCO v4. The opposing pattern of isothermal depth anomaly across the entire gyre is indicative of a southward shift in the gyre.

The agreement between isotherm depth change (grey line; Figure 2.8(b)) and that implied by Ekman pumping (black line; Figure 2.8(b)) is good ($r = 0.77$, significant at the 95% confidence interval), much better than that for RGAC. Further, the isotherm depth changes implied by variations in vertical velocity at the 6°C isotherm (red line; Figure 2.8(b)) correlate strongly with isotherm depth changes ($r = 0.90$) and with those implied by variability in Ekman pumping ($r = 0.93$), suggesting our application of Ekman pumping is appropriate here. Of particular interest are the strong correlations between both the volume and heat content anomaly inferred from the divergence of transport in ECCO v4 (cyan curves in Figure 2.6(a) and (b)) and the depth changes due to Ekman pumping ($r = -0.95$ and $r = -0.98$ respectively; black curve in Figure 2.8(b)), which suggests that basin-wide variability in wind-stress curl sets the divergence of heat and volume in the gyre. In Figure 2.8(b), the volume anomaly due to transport divergence (solid cyan line) has been scaled by the surface area of the 6°C isotherm, giving a depth change with a magnitude that matches both the isotherm depth anomaly and depth change implied by Ekman pumping. The causes of the differences between the depth change implied by Ekman pumping and the variables represented by the grey, red and cyan lines between 2005 and 2007 are not clear.

2.5 Summary and Conclusions

Our results indicate that interannual fluctuations in the upper ocean (>6°C) volume budget of the gyre north of 26°N are primarily set adiabatically by the variability of transport at 26°N and 45°N, while the diabatic air–sea fluxes have a minimal effect. The contribution of air–sea heat fluxes to the volume change at Θ>6°C will only increase if the domain extends permanently beyond the surface outcrop of the 6°C isotherm. For control volumes like ours in which the northern boundary mostly lies equatorward of the 6°C outcrop, air-sea heat fluxes only drive exchange between water mass classes warmer than 6°C rather than across the 6°C isotherm. A good agreement between the volume anomaly due to transport divergence and the variability of both thermocline depth and

Ekman pumping across the gyre suggests that wind-driven heave plays an important role in the transport anomalies at 26°N and 45°N. Yang (2015) show similar results using a simplified model configuration of the North Atlantic. This wind-driven heaving is also a major driver of variations in the heat content of the thermocline waters of the gyre, although anomalies in the air–sea heat fluxes also have an important influence on heat content. While the co-variability of winds and ocean circulation suggests that the wind is driving the ocean, the data is not of high enough temporal resolution to distinguish causality in this ocean/atmosphere mechanism, future analysis would therefore require higher temporal resolution data.

Further, we show that a short-term southward shift of the gyre occurred in 2009/10, linked to a southward shift of the westerlies over the North Atlantic basin. This drove an adiabatic shoaling of isotherms through increased Ekman pumping, presumably leading to transport anomalies across 26°N and 45°N. This suggests that the reduction in the northward transport observed at 26°N in 2009/10 (McCarthy et al., 2012a; Bryden et al., 2014) reflects a southward shift in the mean structure of the interior gyre circulation. While the shift of the gyre (as delimited by the 6°C isotherm) is primarily driven adiabatically, the gyre heat content anomaly is also affected by air-sea heat fluxes.

We conclude that wind forcing plays an important role in driving local, short-term variations in the AMOC. Wind-driven variability has been shown to impact the AMOC across both the subpolar and subtropical gyres (Häkkinen et al., 2011; Schloesser et al., 2014). Such variations in the AMOC have been shown to have significant climatic impacts over the North Atlantic region (e.g. Cunningham et al., 2013), yet the physical mechanisms of these climatic impacts remain unclear. This component of AMOC variability is difficult to resolve and understand with direct observational estimates of the overturning, yet may be unraveled by combining transport estimates with broadly distributed hydrographic observations using the analysis framework presented here. We thus propose that this approach could enhance our ability to interpret the causes and implications of the AMOC variability measured with the mooring array at 26°N.

Chapter 3

The imprint of Southern Ocean overturning on seasonal water mass variability in Drake Passage

Published as: Dafydd Gwyn Evans, Jan D. Zika, Alberto C. Naveira Garabato, and A. J. George Nurser. The imprint of Southern Ocean overturning on seasonal water mass variability in Drake Passage. *Journal of Geophysical Research: Oceans*, 119(11):7987–8010, 2014. **All work in this chapter was done by myself.**

Abstract

Seasonal changes in water mass properties are discussed in thermohaline coordinates from a seasonal climatology and repeat hydrographic sections. The SR1b CTD transects along Drake Passage are used as a case study. The amount of water within temperature and salinity classes and changes therein are used to estimate diathermal and diahaline transformations. These transformations are considered in combination with climatologies of surface buoyancy flux to determine the relative contributions of surface buoyancy fluxes and sub-surface mixing to changes in the distribution of water in thermohaline coordinates. The framework developed provides unique insights into the thermohaline circulation of the water masses that are present within Drake Passage, including the erosion of Antarctic Winter Water (AAWW) during the summer months and the interaction between the Circumpolar Deep Waters (CDW) and Antarctic Intermediate Water (AAIW). The results presented are consistent with summertime wind-driven inflation of the CDW layer and deflation of the AAIW layer, and with new AAIW produced in the winter as a mixture of CDW, remnant AAWW and surface waters. This analysis therefore highlights the role of surface buoyancy fluxes in the Southern Ocean overturning.

3.1 Introduction

The temperature and salinity of the ocean change on a broad spectrum of temporal and spatial scales (Bindoff and McDougall, 1994; Bryden et al., 2003; Delcroix et al., 2005). Such changes are associated with both diabatic (e.g. buoyancy fluxes) and adiabatic (e.g. isopycnal heaving) processes. Diagnosing what drives both intra-annual and decadal fluctuations is crucial for understanding the variations of temperature and salinity observed on regional (Delcroix et al., 1996; Curry et al., 1998, 2003; Meijers et al., 2011) and global (Durack and Wijffels, 2010; Purkey and Johnson, 2010; Durack et al., 2012) scales.

Observed from a conventional Eulerian (fixed geographic) perspective, the ocean is subject to both diabatic and adiabatic changes in temperature and salinity. That is, from a hydrographic record of a particular location in the ocean, one may observe a diabatic change over time in temperature or salinity that is the consequence of variations in the balance of surface heat fluxes or evaporation minus precipitation (E-P) at the region of the surface ocean in which the observed water type is formed, or variations in the strength of mixing processes. In addition, the same fixed hydrographic record is influenced by adiabatic heaving of isopycnals on both seasonal [e.g. Chelton et al., 2011] and interannual (Böning et al., 2008) timescales. These do not represent an addition/removal of freshwater or heat at the surface ocean. Thus, when attempting to understand the variability in the ocean, isolating the diabatic contribution is crucial.

Observing the ocean from an isopycnal framework removes changes due to isopycnal heaving (Bindoff and McDougall, 1994). Effective use of this method however, must be underpinned by a robust understanding of how variability in surface ocean fluxes of freshwater and heat are translated onto observations from an isopycnal perspective. Bindoff and McDougall (1994) separate the above changes in the ocean into three scenarios: pure warming, pure freshening and pure heave, presenting the resultant difference from both pressure and isopycnal perspectives. They highlight the counterintuitive nature of temperature and salinity change on isopycnals. Assuming temperature and salinity decrease with depth, a warming at fixed depth is reflected as a cooling and freshening on an isopycnal. However, a freshening at fixed depth also manifests as a freshening and a cooling on an isopycnal.

Durack and Wijffels (2010) demonstrate the importance of considering the effect of the meridional migration of isopycnal outcrops on changes observed on isopycnal surfaces. These processes will project as changes on isopycnals for example, as isopycnal outcrops migrate due to large scale warming of the ocean, through the mean salinity field set by the stationary E-P field. This would produce an adiabatic change in salinity on isopycnal surfaces that does not reflect a change in the global E-P budget.

Isopycnal outcrop and frontal migration may also occur as a result of dynamical processes. An alternative method to assess changes on isopycnal surfaces was utilised in the Southern Ocean by remotely tracking the position of dynamic height contours (Meijers et al., 2011). Meijers et al. (2011) show an adiabatic warming across the Antarctic Circumpolar Current (ACC) induced by the wind-driven poleward migration of isopycnal outcrops. The usefulness of this method is restricted by the assumption that temperature and salinity profiles are uniquely zonally coherent.

An alternative to density or dynamic height coordinates is to project observations into thermohaline (temperature versus salinity) coordinates. Again, this naturally removes the effect of isopycnal heaving. Bryden et al. (2003), for example, employed this method to assess decadal water mass changes by estimating the minimum change between two profiles in thermohaline coordinates. They showed patterns of coherent change between transects across the Indian Ocean. Such methods are still however subject to the adiabatic process of frontal migration.

Quantitative methods first developed by Walin (1982) have been used to investigate changes in water mass coordinates. Fluxes in water mass coordinates are assessed in terms of air-sea fluxes and diapycnal mixing, integrated across water mass volumes defined by their temperature or density (Nurser et al., 1999; Grist et al., 2009; Maze et al., 2009; Cerovečki et al., 2011; Badin et al., 2013), thus naturally following frontal boundaries. These methods have been extended to thermohaline coordinates (i.e. two tracers) to understand surface fluxes (Speer, 1993), the global thermohaline circulation (Döös et al., 2012; Zika et al., 2012) and the role of variability in that circulation (Groeskamp et al., 2014). However no study has yet applied the water mass transformation framework to understand changes in observations in thermohaline coordinates. Such methods incorporate the best of both the isopycnal framework and the tracking of frontal movements, as following water masses defined by their temperature and salinity implicitly follows isopycnal movement both vertically and horizontally. In addition, changes within thermohaline coordinates are more natural than changes within an isopycnal framework (i.e. the pure warming and pure freshening scenarios of Bindoff and McDougall (1994)) and the geographically distinct thermohaline properties of water masses enable a global analysis within thermohaline coordinates.

The importance of understanding water mass changes in the Southern Ocean is underscored by the fact that the ACC plays a key role in the transformation, formation and ventilation of the world's water masses (Rintoul and Naveira-Garabato, 2013; Talley, 2013). Thus, it is important to understand the sensitivity of the ACC to the changes in the surface buoyancy fluxes and extratropical southern hemisphere westerlies projected for the 21st century (Fyfe and Saenko, 2006; Downes et al., 2009). Within Drake Passage, the focus for this chapter, and the South Atlantic region as a whole, a balance between surface buoyancy fluxes, wind-driven Ekman transport and upwelling, interior diapycnal mixing and eddy stirring/advection controls the distribution of water masses

(Speer et al., 2000; Naveira Garabato et al., 2007; Zika et al., 2009; Marshall and Speer, 2012). In particular, this includes the upwelling and transformation of North Atlantic Deep Water (NADW) into the Upper and Lower Circumpolar Deep Waters (UCDW/L-CDW), the formation and export of Antarctic Bottom Water (AABW), subduction of Antarctic Intermediate Water (AAIW) and Sub-Antarctic Mode Water (SAMW), and the seasonal formation and erosion of Antarctic Winter Water (AAWW; see the two top left panels of Figure 3.1 for the geographical locations of each water mass along a transect across Drake Passage). The role of seasonal changes in the air-ice-sea buoyancy fluxes of heat and freshwater in the formation of these water masses is less clear.

This chapter combines and expands on the work of Walin (1982) and Speer (1993) to explore the seasonal water mass changes in terms of volumes of water in thermohaline coordinates from a repeat hydrographic transect along Drake Passage. We estimate dia-surface water mass transformations as fluxes across isotherms and isohalines, and use these estimates in combination with dia-surface transformations inferred from sea-surface heat and freshwater fluxes to describe the diabatic processes responsible for changes in the distribution of water in thermohaline coordinates. Exploring well defined seasonal changes in this way enables a clearer understanding of the advantages and disadvantages of this technique, which will be useful for the exploration of longer-term (interannual and beyond) trends in temperature and salinity.

Using this water mass transformation framework we resolve the upwelling (CDW) and downwelling (AAIW/SAMW) limbs of the Southern Ocean overturning circulation enabled by the seasonal changes of buoyancy exchange between the atmosphere and the ocean. In the next section we describe the data that we use and our method for the calculation of dia-surface water mass transformations. Sections 3.3 and 3.4 describe seasonal changes along Drake Passage in Eulerian and thermohaline coordinates and in section 3.6 we project the changes calculated in thermohaline coordinates into Eulerian coordinates. These results are interpreted in section 3.7 and summarised in section 3.8.

3.2 Methods

3.2.1 Data

This chapter compares the conservative temperature (Θ) and absolute salinity (S) calculated from two different observational datasets: shipboard conductivity-temperature-depth (CTD) sections and a hydrographic climatology. The shipboard CTD data comprises 20 repeat transects along Drake Passage SR1b sections, occupied between November 1993 and March 2013, available online from the British Oceanographic Data Centre (www.bodc.ac.uk). The advantages of Θ and S over potential temperature and practical salinity are discussed in IOC et al. (2010). The data are full-depth 2 db resolution profiles

of Θ, S and pressure from stations separated on average by ∼20 nautical miles, between 54.67°S and 61.05°S and at 56.56°W. The occupations we use are between November and March, with the majority occurring during December. As a result, our analysis performed using the SR1b dataset is restricted to a comparison between early and late summer. Some transects are incomplete and are not used as part of this analysis.

To augment this approach we also use the CSIRO Atlas of Regional Seas (CARS) 2009. This global climatology provides an atlas of seasonal water mass properties at a 1/2° resolution derived from all available historical subsurface measurements (Ridgway et al., 2002), including CTD data from 1972 within Drake Passage. The data was accessed at www.cmar.csiro.au/cars, from which Θ and S sections replicating the SR1b nominal stations were extracted for comparison with seasonal changes in the SR1b transects. The CARS climatology is restricted to the surface 1000m, so analysis of the SR1b section data will also be restricted to this depth. The CARS climatology includes year-round estimates of seasonal mean temperature and salinity constructed from a mean state estimate and the annual and semiannual harmonic components. This enables both a comparison with the summer changes derived from the SR1b data and further analysis into seasonal changes during the austral winter.

The variability within the SR1b section data is typically dominated by mesoscale processes, apparent as an adiabatic heaving of isopycnals (e.g. compare slope of white contours from SR1b and CARS in Figure 3.1). This makes changes between occupations difficult to interpret. Due to the idealised nature of the fitted seasonal cycle and the lower vertical and horizontal resolution, this is not the case within the CARS seasonal climatology. Therefore, one of the main goals for this chapter is to compare these datasets, and to assess whether or not we can resolve the same seasonal changes in both datasets, by removing this aliased adiabatic mesoscale variability from the seasonal changes observed in the section occupations. That much of the CARS seasonal climatology is likely constructed using SR1b data in this region should not affect the outcome of this analysis given our aim to simply remove the aliased mesoscale variability present in the SR1b data. The CARS seasonal climatology otherwise uses mostly data from Argo profiling floats, particularly during the winter.

We utilise two global air/sea flux climatologies for the sake of comparison: the NOCS flux V2.0 (Berry and Kent, 2009) and a combination of the Woods Hole Oceanographic Institute (WHOI) OAflux/International Satellite Cloud Climatology Project (ISCCP)/Global Precipitation Climatology Project (GPCP) datasets (Yu et al., 2006). From the WHOI OAflux project (hereinafter WHOI; accessed from http://oaflux.whoi.edu) the net heat flux and evaporation products are used. The data used are monthly mean values, globally gridded to 1 degree for the period 1958-present. The net heat flux dataset is a combination of WHOI products and ISCCP radiation products (Schiffer and Rossow, 1985; hosted on the WHOI OAflux project website). Using the WHOI

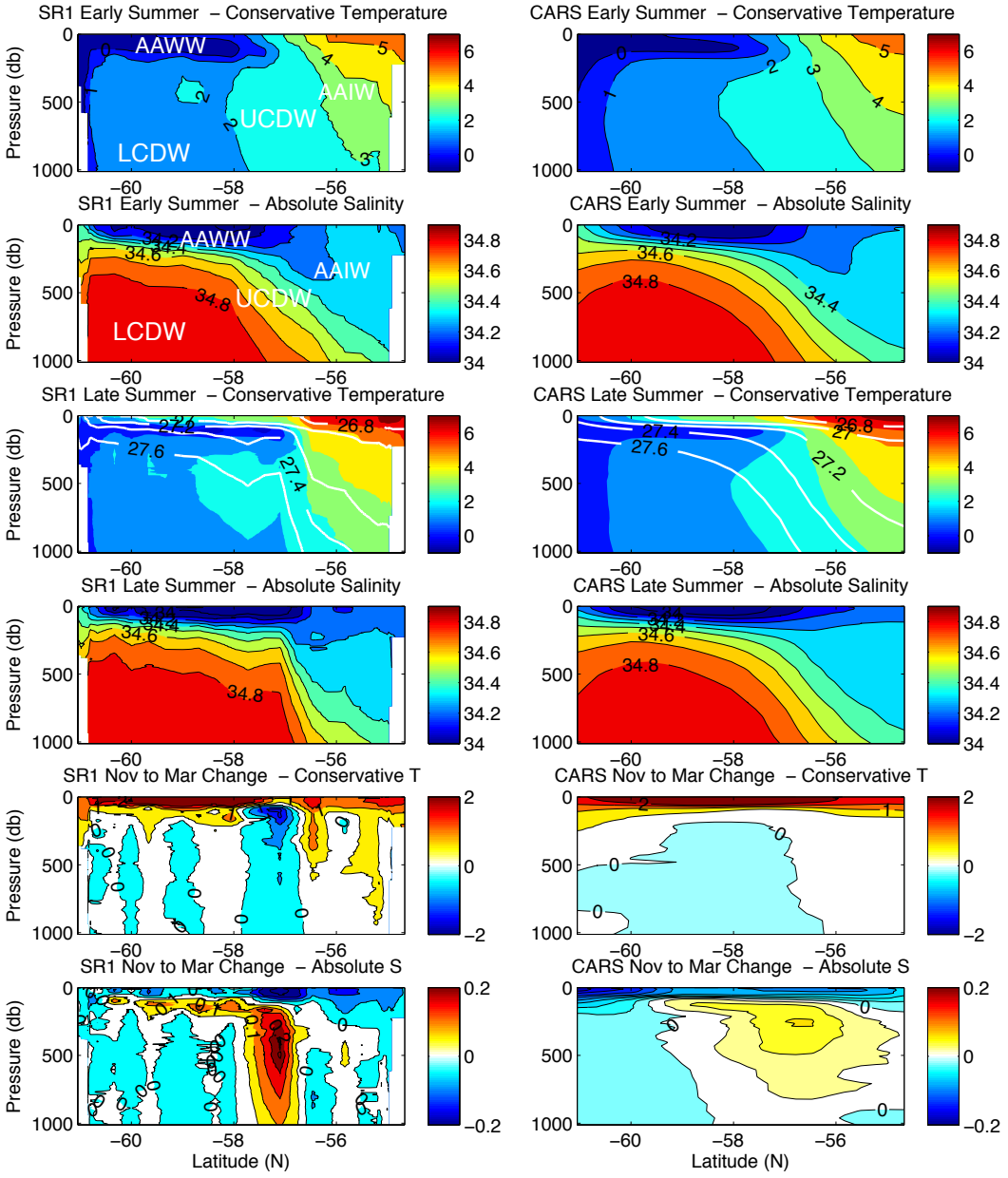

Figure 3.1: Mean early summer and late summer section comparison of Θ and S from the SR1b section occupations (left column) and the CARS seasonal climatology (right column). White contours are potential density anomaly referenced to zero pressure. Labels show Antarctic Winter Water (AAWW), Antarctic Intermediate Water (AAIW), Upper Circumpolar Deep Water (UDCW) and Lower Circumpolar Deep Water (LCDW). The bottom two plots of each figure are the mean late summer section minus the mean early summer section.

dataset, freshwater fluxes are determined through a combination of the WHOI evaporation product and monthly mean precipitation data from the GPCP. This combines various satellite and gauge measurements of precipitation into a merged 2.5 degree global dataset (Adler et al., 2003). From the NOCS flux V2.0 (hereinafter NOCSv2) air/sea flux dataset monthly mean long-wave radiation, short-wave radiation, latent heat flux and sensible heat flux were used to calculate the net heat flux. Freshwater flux was calculated using the NOCSv2 evaporation rate and precipitation rate products. All NOCSv2 products are globally gridded to 1 degree for 1973-2006. For both air–sea flux products data are limited during the winter at the southern end of the transect due to sea-ice cover. Data from all surface flux data sets are linearly interpolated onto the station positions associated with the SR1b section.

3.2.2 Dia-tracer volume flux calculation

The following section describes a general method to represent changes of Θ and S in the ocean as diathermal and diahaline transformations of water between water mass classes in thermohaline coordinates. These dia-surface transformations should be interpreted as volume fluxes of water, and have units of $m^3\ s^{-1}$. They cannot be practically diagnosed from velocity measurements and must therefore be determined indirectly from changes in the volumetric distribution of water projected into thermohaline coordinates. In the case of a two-dimensional ocean transect, which is the focus for this analysis, the method is identical; however the inferred transformations are area fluxes and have units of $m^2\ s^{-1}$.

To infer these dia-surface transformations, first consider the conservation of some tracer, C, which, assuming incompressible flow, can be described as follows:

$$\frac{\partial C}{\partial t} + \mathbf{u} \cdot \nabla C = f_C + \nabla \cdot \mathbf{K} \nabla C. \tag{3.1}$$

Here $\mathbf{u}$ is the three dimensional Eulerian velocity, f_C is a source/sink of C and $\mathbf{K}$ is a diffusion tensor encompassing both the isopycnal and diapycnal mixing coefficients. Here the change in C is separated into the Eulerian and advective components (LHS), which are balanced by a diabatic flux term and a diffusive term (RHS).

Dividing the left hand side of equation (3.1) by the modulus of the tracer gradient gives the dia-surface velocity component (u_C), the component of the velocity that crosses the surface of constant C, so that:

$$u_C = \frac{1}{|\nabla C|} \frac{\partial C}{\partial t} + \mathbf{u} \cdot \frac{\nabla C}{|\nabla C|}. \tag{3.2}$$

Here $(\partial C/\partial t)/\left|\nabla C\right|$ is the component of the dia-surface velocity due to movement of the surface of constant C and $(\mathbf{u}\cdot\nabla C)/\left|\nabla C\right|$ is the component of the dia-surface velocity due to Eulerian flow normal to the surface of constant C. Note u_C has units of m s^{-1}. Equation (3.2) will be undefined where $|\nabla C| = 0$ but no iso-surface will exist there either. We now consider the tracers Θ and S, so that u_{Θ^*} becomes the diathermal velocity crossing the isotherm Θ and u_{S^*} the diahaline velocity crossing the isohaline S. The transformation across each isotherm (Θ) within the salinity class $S^* = S \pm \Delta S/2$ and across the isohaline (S) within the temperature range $\Theta^* = \Theta \pm \Delta\Theta/2$ will therefore be:

$$U_\Theta(\Theta, S) = \int_{\Theta^*=\Theta} \Pi(S, S^*)\, u_{\Theta^*}\, \mathrm{d}A, \tag{3.3}$$

$$U_S(\Theta, S) = \int_{S^*=S} \Pi(\Theta, \Theta^*)\, u_{S^*}\, \mathrm{d}A, \tag{3.4}$$

where Π is a boxcar function that is 0 when Θ or S is outside the range defined by the given Θ-S class, or 1 when Θ and S are within this range, while $\int \mathrm{d}A$ is an integral over the surface area of the isotherm within the salinity limits or over the isohaline surface within the temperature limits. A positive transformation represents water moving to warmer and saltier water mass classes. Thus, the rate of change of a volume of water defined by a given Θ-S class ($\Theta^* = \Theta \pm \Delta\Theta/2$, $S^* = S \pm \Delta S/2$) in terms of the transformation of water across isotherms and isohalines defined at $\Theta \pm \Delta\Theta/2$ and $S \pm \Delta S/2$ is

$$\begin{aligned}\left.\frac{DV}{Dt}\right|_{\Theta,S} &= U_\Theta(\Theta - \Delta\Theta/2, S) - U_\Theta(\Theta + \Delta\Theta/2, S) + \\ & U_S(\Theta, S - \Delta S/2) - U_S(\Theta, S + \Delta S/2) + \epsilon(\Theta, S).\end{aligned} \tag{3.5}$$

This relation is shown schematically in Figure 3.2 in both geographical coordinates (top) and thermohaline coordinates (bottom). Here the volume of water at Θ and S is set by the transformation of water across the isotherms $\Theta - \Delta\Theta/2$ and $\Theta + \Delta\Theta/2$, and the isohalines $S - \Delta S/2$ and $S + \Delta S/2$, with dia-surface transformations of $U_\Theta(\Theta - \Delta\Theta/2, S)$, $U_\Theta(\Theta + \Delta\Theta/2, S)$, $U_S(\Theta, S - \Delta S/2)$ and $U_S(\Theta, S + \Delta S/2)$ respectively, as given in (4.2). These dia-surface transformations therefore represent the volume of water transformed per unit time by $\Delta\Theta$ for the diathermal components and by ΔS for the diahaline components, to account for the volume change within each $\Theta - S$ class. Volume fluxes into and out of the geographical domain within which thermohaline volumes are determined may be interpreted as two additional unknown volume flux terms on the RHS of equation 4.2, which have been combined into ϵ.

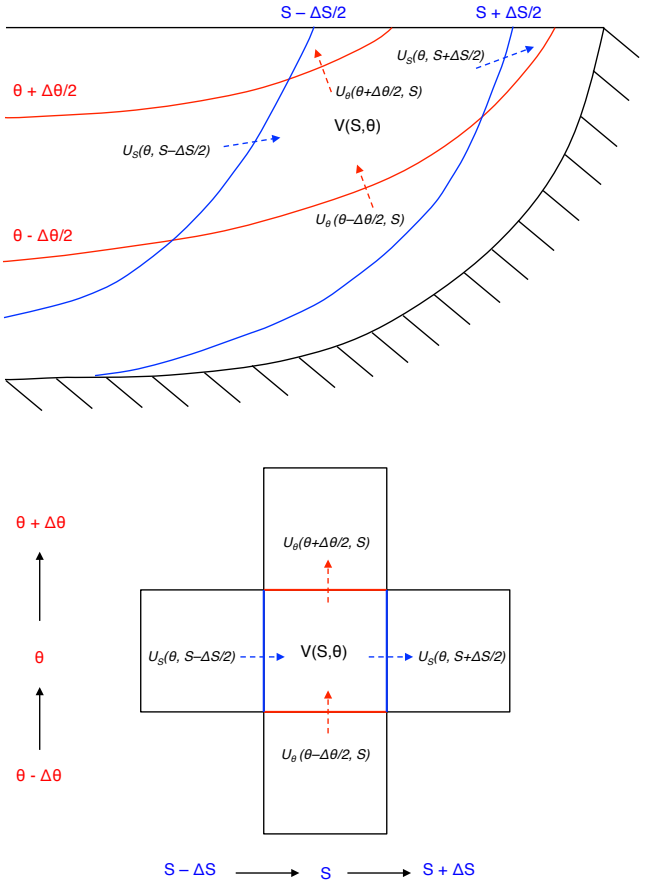

Figure 3.2: Schematic of the relation described by (3.5) for a given value of Θ and S.

The dia-surface transformations across each isotherm and isohaline are thus constrained by the volume changes of each Θ-S class. We can then uniquely determine the dia-surface transformations by solving for the transformation field with minimum magnitude that satisfies equation (3.5). The volume changes are determined as follows. First a nominal grid spacing in thermohaline coordinates is chosen. This grid spacing must be fine enough to resolve the finer water mass transformations in the specified region, but coarse enough to give adequate coverage in Θ-S coordinates so that there are not any artificially disconnected regions separated by no data. Further, it is advantageous to choose Θ and S spacings that have a roughly similar contribution in terms of changes in density. A resolution of 0.25°C and 0.025 g kg^{-1} is chosen to meet these criteria. As would be expected, a coarser resolution in Θ and S gives larger individual volumes and thus larger dia-surface transformations as in general the total volume should not increase.

To calculate the water mass volume associated with each Θ-S class, the volume of each geographical grid cell was calculated (i.e. zonal×meridional×vertical extent, or meridional×vertical extent for an ocean section). The Θ-S value at the centre of each geographical grid cell was determined through linear interpolation. The thermohaline

volume for a given Θ-S class is then the sum of the volume associated with each geographical grid cell within the range $\Theta \pm \Delta\Theta/2$ and $S \pm \Delta S/2$. In practice the thermohaline area associated with each SR1 section occupation is normalised so that the total area of each section is the same. Note that a particular Θ-S combination can exist in multiple locations within the geographical grid for example, by advection by eddies. An advantage of this method is its ability to capture the effect that such processes have on these water masses. Further, by definition water masses in adjacent Θ-S classes must be adjacent in geographical coordinates as there cannot be a discrete jump in the gradient of Θ or S, unless separated by a land mass, which is not the case in this chapter.

Using (4.2), a set of linear equations can be built to link the observed change in volume of each Θ-S class, as determined above, to the dia-surface transformations within the defined thermohaline coordinate space:

$$\mathbf{A}\mathbf{x} = \mathbf{b}, \tag{3.6}$$

where,

$$\mathbf{A} = \begin{bmatrix} -1 & 0 & \cdots & 0 & -1 & \cdots & 0 & 0 & \cdots & 0 \\ 1 & -1 & \cdots & 0 & 0 & \cdots & 0 & 1 & \cdots & 0 \\ \vdots & \vdots & \ddots & \vdots & \vdots & \ddots & \vdots & \vdots & \ddots & \vdots \\ 0 & 0 & \cdots & 1 & 0 & \cdots & 1 & 0 & \cdots & 0 \end{bmatrix}, \tag{3.7}$$

$$\mathbf{b} = \left[\frac{DV}{Dt}\Big|_{\Theta_1,S_1}, \quad \frac{DV}{Dt}\Big|_{\Theta_2,S_1}, \quad \cdots, \quad \frac{DV}{Dt}\Big|_{\Theta_m,S_n} \right] \tag{3.8}$$

$$\begin{aligned} \mathbf{x} = [&U_\Theta((\Theta_2+\Theta_1)/2, S_1), U_\Theta((\Theta_3+\Theta_2)/2, S_1) \cdots, U_\Theta((\Theta_m+\Theta_{(m-1)})/2, S_n), \\ &U_S(\Theta_1, (S_2+S_1)/2), U_S(\Theta_2, (S_2+S_1)/2)), \cdots, U_S(\Theta_m, (S_n+S_{(n-1)})/2), \\ &\epsilon(\Theta_1, S_1), \cdots, \epsilon(\Theta_m, S_n)] \end{aligned} \tag{3.9}$$

Here the vector $\mathbf{b}$ is the observed change in volume of each Θ-S class, divided by the relevant time-interval and should be $m \times n$ long, where m is the number of individual Θ classes and n is the number of individual S classes. The vector of unknowns $\mathbf{x}$ will therefore be the diathermal and diahaline transformations and the volume change associated with ϵ. The vector $\mathbf{x}$ will have length $[(m-1)\times n] + [m \times (n-1)] + (m \times n)$. The matrix $\mathbf{A}$ represents the coefficients relating each term on the RHS of (4.2) to the volume change. Each of the $m \times n$ rows represents the equation for the change in volume of a Θ-S class. The first $[(m-1)\times n] + [m \times (n-1)]$ columns in $\mathbf{A}$ corresponds to a each Θ or S iso-surface, and the coefficients describe the relation of each iso-surface to

the Θ-S class designated in each row. A coefficient of 1 is assigned to the isotherm (or isohaline) at $\Theta - \Delta\Theta/2$, and a coefficient of -1 is assigned to the isotherm (or isohaline) at $\Theta + \Delta\Theta/2$. The coefficient is zero for each isotherm and isohaline that is not adjacent in thermohaline coordinates to the $\Theta - S$ class associated with the given row.

The last $m \times n$ columns of $\mathbf{A}$ represent each Θ-S class, to which a coefficient of 1 is assigned if that value of Θ or S is adjacent to the boundary of the domain in geographical coordinates; thus allowing a flux into or out of the domain due to the terms combined into ϵ. Further, we are assuming that only advection meridionally through the northern boundary of the geographical domain will affect the distribution of volume in thermohaline coordinates. The linear equations can then be solved for $\mathbf{x}$ using a least squares regression, where the magnitude of the residuals (i.e. $\sqrt{\sum(\mathbf{b} - \mathbf{A}\mathbf{x})^2}$) are minimised. For reference these residuals are shown in Figure 3.11. For all calculations the relative residuals ($(\sqrt{\sum(\mathbf{b} - \mathbf{A}\mathbf{x})^2})/\sqrt{\sum(\mathbf{b})^2}$) are less than 0.001 and generally $<1 \times 10^{-6}$. The divergence of the derived transformations therefore represent the combination of volume fluxes that give a volume change that most closely match the volume change of each Θ-S class.

The temporal distribution of SR1b section occupations enables analysis of the changes in water mass area and the associated dia-surface transformation from early to late summer. The early summer water mass area is estimated from five November section occupations (1993, 1994, 1996, 2000 and 2001) by calculating the water mass area in $\Theta - S$ space for each individual section and computing the mean area. The late summer estimate is determined in the same way from three section occupations from February 2000, February 2009 and March 2013. The seasonal change in water mass area distribution is therefore the difference between early and late summer. This change divided by the time-interval from early to late summer (3.5 months) is used to populate $\mathbf{b}$ and thus infer the seasonal fluxes of water mass area. The early to late summer water mass area changes and inferred dia-surface transformations are not sensitive to the selected transects and the outcomes are not affected if individual sections are used as opposed to a mean. The distribution of the averaged SR1b section occupations through the time-series might result in the aliasing of any long-term trends in the early to late summer means. However, as discussed by Meredith et al. (2011), there is no clear long-term trend in water mass properties along Drake Passage. The seasonal change in water mass area within $\Theta - S$ space for CARS is determined in the same way; however, the early summer water mass area distribution uses the climatological estimate for November, whereas the late summer uses both the February and March estimates.

3.2.3 Calculation of dia-surface transformations inferred from air/sea fluxes

The transformation of sea surface $\Theta - S$ classes can be determined from air/sea fluxes of heat and freshwater. Speer (1993) presents a method to calculate the transformation implied by surface air/sea fluxes in thermohaline coordinates. Diathermal (F_Θ) and diahaline (F_S) transformations are determined by calculating the amount of water converted by the integrated heat and freshwater flux over the area (A) within each sea-surface Θ and S class:

$$F_\Theta(\Theta, S) = \int \frac{\Pi(\Theta, \Theta^*)}{\Delta\Theta} \Pi(S, S^*) \frac{Q_{net}}{\rho C_p} \, \mathrm{d}A; \tag{3.10}$$

$$F_S(\Theta, S) = \int \Pi(\Theta, \Theta^*) \frac{\Pi(S, S^*)}{\Delta S} f_{net} S \, \mathrm{d}A. \tag{3.11}$$

Again Π is a boxcar function that is either 0 when Θ or S is outside the range defined by the given Θ-S class, or 1 when Θ and S are within this range. Q_{net} and f_{net} are the net surface heat flux (W m^{-2}) and E-P (m s^{-1}) respectively, ρ is the density and C_p is the specific heat capacity of seawater. Here $\int \mathrm{d}A$ represents an integral over an area of the sea surface occupied by a given $\Theta - S$ class. This calculation of F_Θ differs from that used by Speer (1993) through the use of density, converting the mass flux calculated by Speer (1993) to a volume flux. Thus, F_Θ and F_S are in units of m^3 s^{-1}. When calculating these fluxes over a two-dimensional ocean transect as done here, $\mathrm{d}A$ becomes $\mathrm{d}L$, where L is the length-scale defined by each sea-surface Θ-S class, giving a flux in units of m^2 s^{-1}.

From the dia-surface transformations calculated using equations (3.10) and (3.11) the inferred volume change can be computed using equation (3.6) by populating $\mathbf{x}$ with F_Θ and F_S, giving $\mathbf{b}$, the rate of change of volume due to air-sea fluxes, which when multiplied by the relevant time-interval yields the volume change. This surface buoyancy flux-inferred volume change can then be removed from the observed volume change, giving a residual volume change. Residual dia-surface transformations can then be calculated by populating $\mathbf{b}$ with the residual volume change divided by the time interval, and solving for $\mathbf{x}$ as in section 3.2.2 for the total dia-surface transformations. From equation (3.1), this gives the residual dia-surface transformations due to diffusive processes if an entire $\Theta - S$ volume is enclosed. If the entire volume is not enclosed, so that all the water of a given $\Theta - S$ class is not captured within the geographical domain used, transport of this particular class across the geographical boundary will imprint as a dia-surface transformation. Similarly, for a two-dimensional transect where water mass area is considered, as opposed to water mass volume, this residual will also include a component associated with changes in the advective transport of water through the

boundaries of the geographical domain used. In both cases these volume transports would manifest in the term ϵ in equation 4.2.

3.3 Drake Passage from an Eulerian perspective

To provide a comparative framework in which to present the water mass changes within Drake Passage in thermohaline coordinates, we first discuss early to late summer changes from an Eulerian perspective, i.e. in latitude-pressure coordinates. In Eulerian coordinates a mean of the SR1b section occupations in November is used to represent early summer. This is compared with a mean late summer transect determined using the three section occupations from February 2000, February 2009 and March 2013 (left column, Figure 3.1). These are compared with mean transects taken from the CARS climatology using the same combination of months (right column, Figure 3.1).

In the early summer along SR1b mean, surface and near-surface waters are generally cooler, in particular a thick tongue of cold (Θ<0°C) and fresh (S<34.2 g kg^{-1}) AAWW extends northward from the Antarctic continent (Figure 3.1;first four panels). This layer is less pronounced later in the summer, while surface waters are in general warmer and fresher. Underlying these seasonal surface water masses is a wedge of relatively salty CDW with S>34.8 g kg^{-1}. Discerning any change in the properties of these deeper water masses is difficult given the large variability in the depth of isopycnals surrounding them. This is likely the result of aliased mesoscale variability, also evidenced by the lenses of ∼2°C water that have been advected across the Polar-Front (PF) and are evident in both early and late summer.

The CARS climatology generally replicates the mean properties represented by the SR1b section observations, differing only in the absence of the mesoscale related variability (Figure 3.1; first four panels, right column). Further, the wedge of CDW appears to be less extensive in the climatology and shows very little change during the summer.

The change in Θ and S from early to late summer (Figure 3.1; lower four plots) highlights some of the difficulties in determining change within an Eulerian coordinate system. The change according to the SR1b section data gives a generally coherent warming (>2°C) and freshening (<-0.015 g kg^{-1}) at the surface where the seasonal change is large (Figure 3.1; left column, lower two plots). Below the surface the pattern of change is much less clear due mostly to aliased mesoscale variability, with an apparent cooling of up to 2°C and an increase in S as high as 0.2 g kg^{-1} in the region of the PF. In the absence of these mesoscale fluctuations, the CARS climatology again shows a coherent warming and freshening in the surface with similar magnitude, but suggests a more coherent area of weaker cooling and salinification below the surface, coinciding roughly in location with the largest subsurface changes according to the SR1b section data. The proximity

of these changes to the PF makes disentangling the relative contribution of diabatic and adiabatic changes difficult given the impact of frontal migration in this region.

3.4 Drake Passage in thermohaline coordinates

In this section we discuss changes in water mass properties in thermohaline coordinates within Drake Passage, comparing data from the SR1b section occupations and the CARS climatology. These results are then interpreted in section 3.7. To provide some geographical context to the $\Theta - S$ observations, the mean $\Theta - S$ profiles from the SR1b transects used in section 3.3 are plotted in Figure 3.3, where the colour-scale represents the pressure associated with each measurement. In both the observations and the CARS climatology the UCDW and the saltier LCDW make up the shoulder of measurements characterised by the pycnocline that shoals from the northern to the southern end of the transect, and is mostly set by a strong gradient in S between the fresher SAMW/surface waters and the saltier UCDW and LCDW. According to the SR1b section occupations (and to some extent the climatology) surface and near-surface observations (blues to yellows) are grouped into two regions of $\Theta - S$ space, which are geographically separated by the PF. This separation is exaggerated by the late summer as the S-minimum associated with AAIW at 4°C and 34.3 g kg^{-1} is reduced. From early to late summer the surface waters in general become warmer and fresher in both datasets. The subsurface AAWW is apparent in both the climatology and the observations, but is approximately 0.2°C warmer in the climatology. The AAWW warms from early to late summer in both datasets.

The distribution of water mass area within thermohaline coordinates and the early to late summer change in distribution (determined as described in section 3.2.2) is similar according to the SR1b section occupations and the CARS climatology (Figure 3.4; left and right panels respectively). The region of largest water mass area is associated with LCDW (Θ ~2°C and S ~34.9 g kg^{-1}). Both datasets resolve a ridge of high water mass area either side of the PF, the warmer side of which is made up of UCDW and AAIW. The peak at the coldest and freshest extent of the ridge associated with the region south of the PF highlights the seasonally formed AAWW. The erosion of AAWW from early to late summer is evident both as a decrease in water mass area at this region of $\Theta - S$ space and as a redistribution of water mass area into warmer and fresher regions of $\Theta - S$ space. Also evident is a redistribution of surface water masses to a warmer and fresher region of $\Theta - S$ space.

The information in Figures 3.3 and 3.4 enables a clear description of the early to late summer changes in water mass properties within Drake Passage. These seasonal changes described in thermohaline coordinates are not aliased by frontal migration or the adiabatic processes associated with mesoscale variability apparent in the left panel of Figure

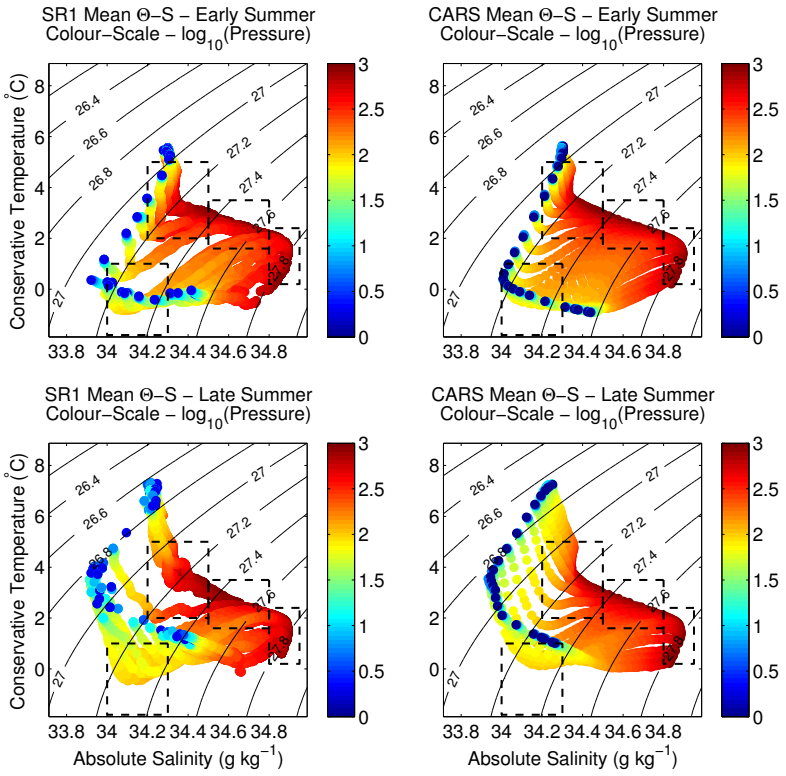

Figure 3.3: Mean early summer (top row) and late summer (bottom row) $\Theta - S$ profiles from the SR1b section occupations (left column) and the CARS seasonal climatology (right column). The colour scale indicates the $\log_{10}$ pressure of each observation. The dashed boxes show the locations of (from left to right) AAWW, AAIW, UCDW and LCDW.

3.1. Furthermore, they provide an initial basis for a quantitative assessment of the balance between the diabatic exchanges of buoyancy that drive the observed seasonal changes. We will now discuss the associated dia-surface transformations derived from the change in water mass area between early summer and late summer.

For an entirely enclosed water mass *volume*, the change in the distribution of this volume within $\Theta - S$ space and the derived dia-surface transformations will be entirely diabatic. A change associated with surface buoyancy forcing will therefore appear as a redistribution to a different region in $\Theta - S$ space according to the applied buoyancy flux (e.g. panel (b), Figure 3.5). In contrast, both isopycnal and diapycnal mixing of two water masses in different regions of $\Theta - S$ space will appear as dia-surface transformations that converge to the mean Θ and S of the two water masses that are being mixed (e.g. panel (a), Figure 3.5). In this investigation, where we are analysing the seasonal change within a two-dimensional ocean transect and discussing this change in terms of water mass *area*, the case that all changes are diabatic is not true. The analysis of an ocean transect using this method, as with other methods, is subject to the adiabatic change associated with variability in the meridional and zonal advection of water in geographical coordinates through the geographical boundary of the domain from which

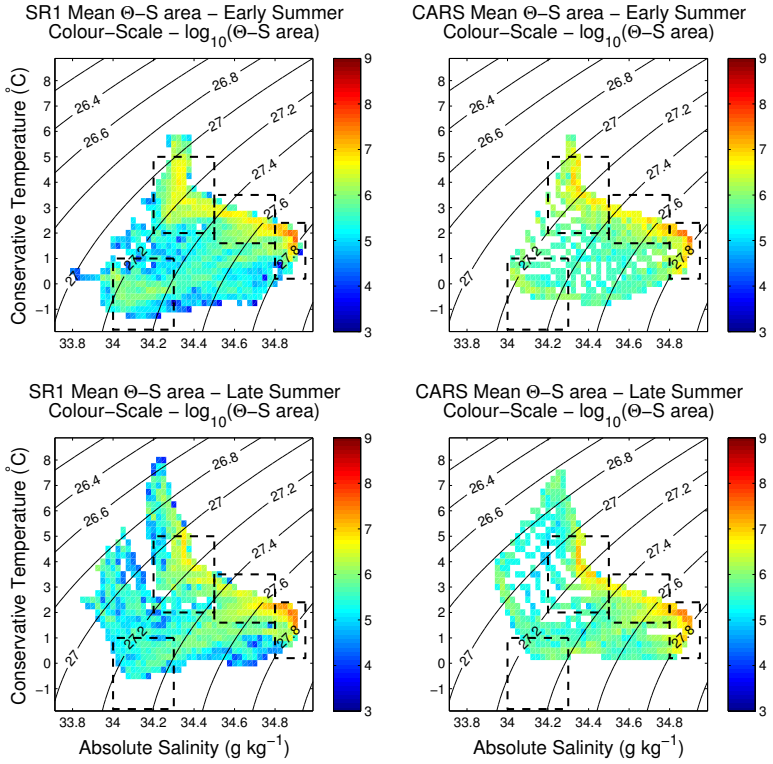

Figure 3.4: Mean early summer (top row) and late summer (bottom row) $\Theta - S$ area from the SR1b section occupations (left column) and the CARS seasonal climatology (right column). The colour scale indicates the $\log_{10}$ area of each $\Theta - S$ class. The dashed boxes show the locations of (from left to right) AAWW, AAIW, UCDW and LCDW.

water mass area is determined (ϵ term, RHS equation (4.2)). In this case, an adiabatic change will appear as a redistribution of water mass area to a different region in $\Theta - S$ space, with a similar appearance to a diabatic change driven by surface buoyancy fluxes (panel (b), Figure 3.5). For example, an increase in the amount of cold salty water transported into the section geographically, would imprint as negative diathermal and positive diahaline transformations in $\Theta - S$ space. The advantage of this method is that it should be clearer, with some interpretation, where these advective processes are affecting the distribution of water mass area within $\Theta - S$ space, based on a comparison with the implied dia-surface transformations derived using the seasonal surface air/sea fluxes and the estimated area change due to ϵ.

The early to late summer change in water mass area and the associated dia-surface transformations are characterised by a redistribution of water to a generally warmer region within $\Theta - S$ space (Figures 3.6 and 3.7; SR1b and CARS respectively). The area changes for both the SR1b section occupations and the CARS climatology indicate a warming of the ridges of high water mass area highlighted in Figure 3.4. The largest changes occur in the AAIW ($\sim$4°C and 34.4 g kg^{-1}). Large changes in water mass area also occur in the UCDW and the LCDW. The loss of water mass area from the

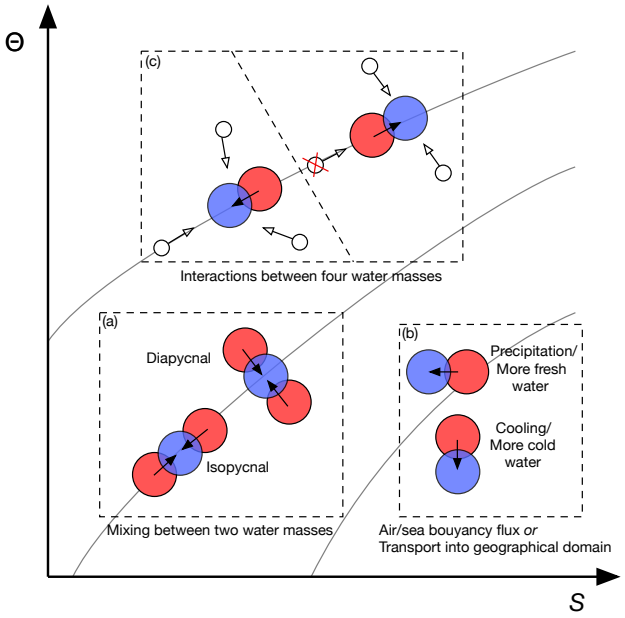

Figure 3.5: A simplified representation of the processes that can change the location of water mass area within $\Theta - S$ space. In each a red circle represents the initial location of a water mass in $\Theta - S$ space, and a blue circle represents the final location. The black arrows are the dia-surface transformations of water mass area associated with the redistribution. In the case of box (c), which describes the interactions of four water masses, the unfilled arrows represent the direction from which each water mass (unfilled circles) is mixing. This relates to the process affecting the location of AAIW within $\Theta - S$ space during winter (left) and summer (right) and it's relation to the presence of AAWW (e.g. bottom left unfilled circle) as discussed in section 3.7.

coldest and freshest region within $\Theta - S$ space reflects the seasonal erosion of AAWW over the summer. The transformation vectors in Figures 3.6 and 3.7 show the minimum transformation required to produce the observed change in water mass area. These transformations may not reflect the actual path within $\Theta - S$ space taken by each parcel of water; however, given the temporal resolution of both datasets, the black arrows represent as much as can be inferred regarding the direction and magnitude of the transformations.

In the surface and near-surface waters of the section occupations and the climatology, that is near the region of lowest S along the ridges of high water mass area, the direction of the dia-surface transformations reflect a warming and freshening. These transformations have magnitudes of the order of 0.5 $m^2\ s^{-1}$ and are typically diapycnal in direction. The erosion of AAWW seems to be driven by a mostly diathermal transformation with a minimal diahaline component. This is consistent in both datasets. The dia-surface transformations in the deeper water masses are larger when determined using the section occupations. They have magnitudes of $<0.3\ m^2\ s^{-1}$ with a warming and salinification in the AAIW, a consistent positive diahaline component throughout the UCDW, but a

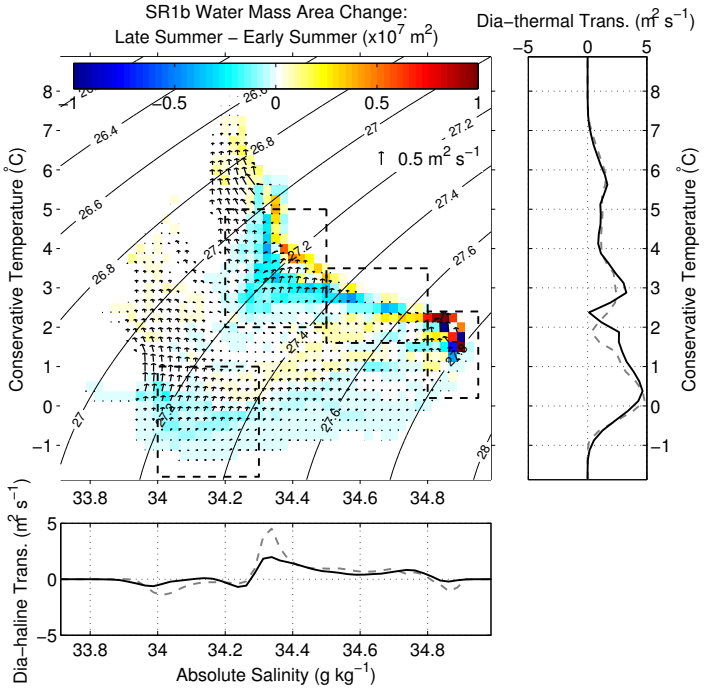

Figure 3.6: $\Theta - S$ area change (colour scale) and associated dia-surface transformations (arrows) from early summer to late summer from the SR1b section occupations. The right and lower panels are the summed diathermal and diahaline transformations respectively (black lines: SR1b section occupations, grey lines: CARS climatology). Area change has units of $1{\times}10^7$ m^2. Transformations have units of m^2 s^{-1}. The dashed boxes show the locations of (from left to right) AAWW, AAIW, UCDW and LCDW.

warming at Θ<1°C and a cooling at Θ>1°C. For the LCDW in the region of highest S, dia-surface transformations have a positive diathermal component, with negative and positive diahaline components converging at 34.85 g kg^{-1}. The dia-surface transformations in the deeper water masses are much weaker according to the seasonal climatology. The transformations have a similar direction, but differ with a convergence of vectors in the LCDW at a Θ and S of ∼1°C and 34.8 g kg^{-1}.

The diahaline and diathermal transformations summed across all values of Θ and S respectively for both the section occupations (Figure 3.6; bottom/right panel) and the seasonal climatology (Figure 3.7; bottom/right panel) are similar. Exceptions are a negative diathermal transformation that is evident only in the section occupations between 2 and 3°C and a negative diahaline transformation at S>34.8 g kg^{-1} in the seasonal climatology. These differences between the section occupations and the climatology are likely an aliasing of a change in either the zonal or meridional advection of water through the section that is aliased to a greater extent by the averaging of the section occupations.

Solving for ϵ in equation (4.2) provides an estimate of the transport through the geographical boundary of the section. The volume change associated with ϵ for both the

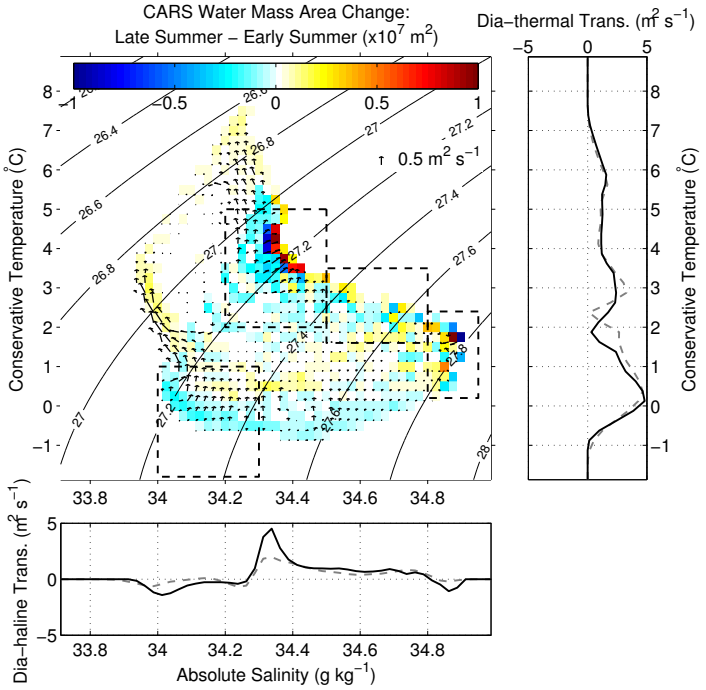

Figure 3.7: $\Theta - S$ area change (colour scale) and associated dia-surface transformations (arrows) from early summer to late summer from the CARS climatology. The right and lower panels are the summed diathermal and diahaline transformations respectively (black lines: CARS climatology, grey lines: SR1b section occupations). Area change has units of 1×10^7 m^2. Transformations have units of m^2 s^{-1}. The dashed boxes show the locations of (from left to right) AAWW, AAIW, UCDW and LCDW.

SR1b section occupations (Figure 3.8; top) and the CARS climatology (Figure 3.8; bottom) indicate an increase of water mass area in the LCDW, suggesting a flow of LCDW into the geographical domain of the section. There is also a loss of water mass area in the AAIW, suggesting a flow of AAIW out of the geographical domain of the section. The degree to which the changes of water mass area associated with ϵ calculated in this way reflect the actual transport into and out of the geographical domain of the section remains unclear. However, this approach could be tested using a numerical model where the volume transports can be easily determined.

We next describe the early to later summer dia-surface transformation and resultant area change inferred from the sea-surface fluxes of heat and freshwater from the WHOI climatology. The following analysis was also performed using the NOCSv2 climatology, which shows that there is no substantial difference between the inferred transformations discussed below. To determine a smooth seasonal transition from early to late summer, the surface fluxes and the sea-surface Θ and S were linearly interpolated to a high temporal resolution of approximately 6 days. The dia-surface transformations were determined for each time step, and the sum of the resultant area change was calculated for all the resultant time steps. This sum was then used to determine the total implied dia-surface transformation, which is shown in Figures 3.9 and 3.10. If this interpolation

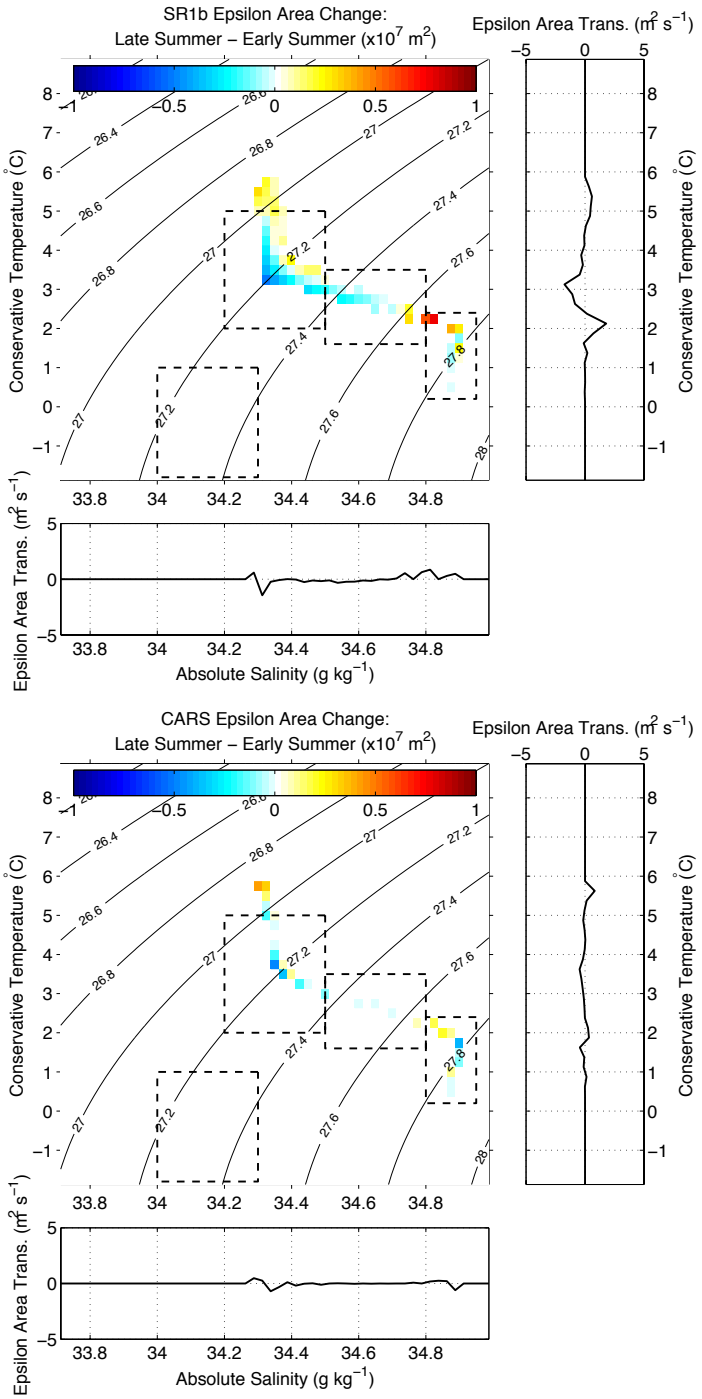

Figure 3.8: $\Theta - S$ area change associated with the ϵ term in equation (4.2) for the SR1b section occupations (top) and the CARS seasonal climatology (bottom). Area change has units of 1×10^7 m^2. Solid lines in the bottom and right panels indicate the $\Theta - S$ area change summed across all Θ or S divided by the time-interval from early to late summer (3.5 months) to compare to Figures 3.6 and 3.7. The dashed boxes show the locations of (from left to right) AAWW, AAIW, UCDW and LCDW.

is not performed then the inferred area change is restricted to a small region of $\Theta - S$ space, and does not mimic the broad redistribution apparent at the surface in Figures 3.6 and 3.7. An interpolation with a lower temporal resolution results in data-less regions of $\Theta - S$ space.

The implied water mass area change and dia-surface transformations indicate ubiquitous warming and freshening of all surface water masses from early to late summer (Figures 3.9 and 3.10; SR1b/CARS respectively), with transformations up to 0.5 m^2 s^{-1} in the regions of $\Theta - S$ space with high water mass area separated geographically by the PF. This separation is evident as peaks in the plots of the diathermal and diahaline transformations in the upper panels of Figures 3.9 and 3.10, summed across all S and Θ respectively. The pattern of water mass area change shown in Figures 3.9 and 3.10 are noisy and patchy. This partly reflects the noise within the air-sea flux data, but also the impact of strong gradients in Θ and S across the PF.

The area change, determined from air/sea fluxes can be subtracted from the total area change shown in Figures 3.6 and 3.7 to give a residual area change, and therefore transformation. The resultant pattern of area change and the vectors of transformation remain unchanged from the net change shown in Figures 3.6 and 3.7 for the majority of $\Theta - S$ space away from the sea-surface (Figures 3.9 and 3.10; lower panel). The net water mass area change and transformation in the surface water masses (e.g. Figures 3.6 and 3.7) are smaller than the transformation and change inferred from the air/sea fluxes. The result is a residual negative diathermal transformation and positive diahaline transformation for those surface water masses that are parallel to the slope of the $\Theta - S$ profiles, suggesting a downward mixing of the seasonally warmed and freshened surface water with the generally cooler and saltier sub-surface water. The convergence of vectors to $\sim$0°C and 34.1 g kg^{-1} within $\Theta - S$ space (lower panels of Figures 3.9 and 3.10) indicate the erosion of the AAWW during the summer. The direction of the vectors suggests this process is underpinned by diapycnal mixing (see panel (a), Figure 3.5).

Dia-surface transformation of water mass area inferred from the NOCSv2 climatology (Figure 3.12; top left: SR1b section occupations; top right: CARS) show a similar pattern of freshening and warming to the WHOI climatology, apart from a small positive diahaline transformation at the warmest Θ in the CARS climatology. The residual water mass area change and dia-surface transformations determined using the NOCSv2 climatology (Figure 3.12; bottom left: SR1b section occupations; bottom right: CARS) are therefore similar to those determined using the WHOI climatology, particularly the region of $\Theta - S$ space that defines the AAWW. This consistency between sea surface flux data sets gives confidence in the reliability of both data.

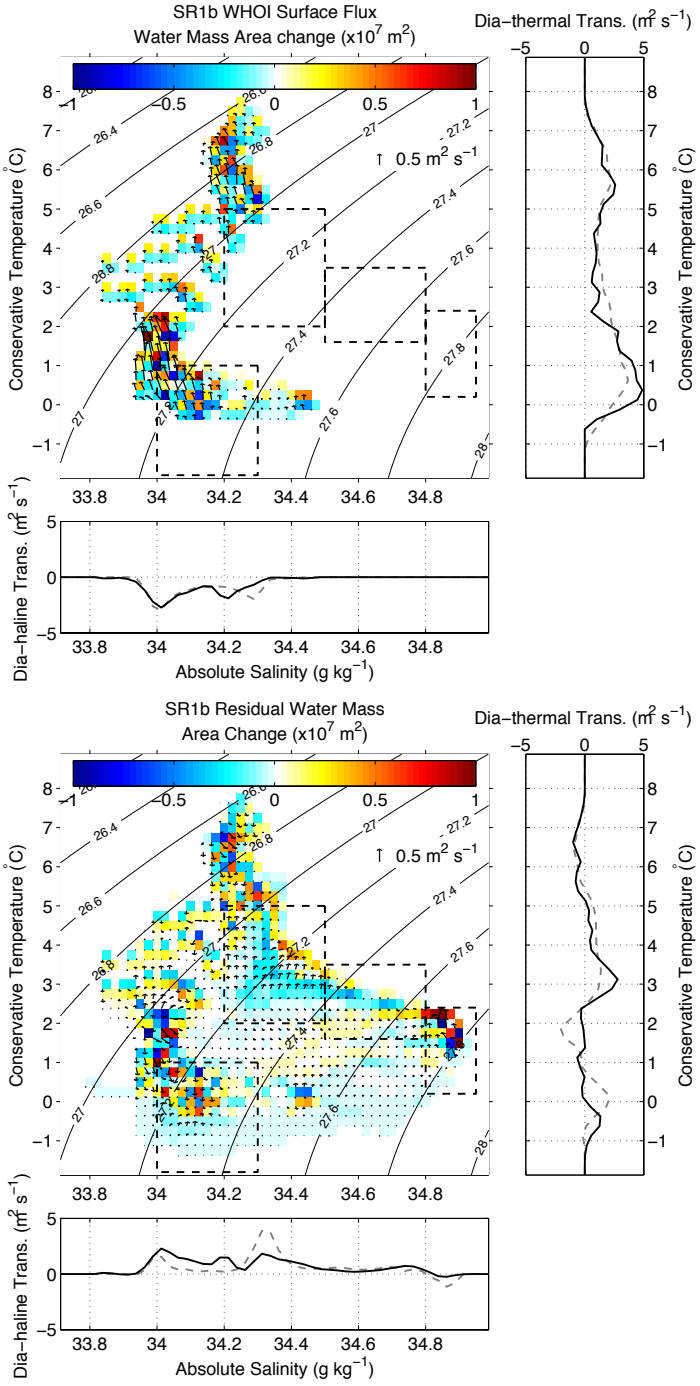

Figure 3.9: As in Figure 3.6 but showing dia-surface transformations and $\Theta - S$ area change inferred from the WHOI surface flux climatology (upper plots), and the resultant residual dia-surface transformations and $\Theta - S$ area change (lower plots) from the SR1b section occupations. The surface flux area change and associated dia-surface transformations are determined cumulatively from the surface heat and freshwater fluxes between early and late summer. The residual area change and associated dia-surface transformations are calculated by subtracting the sea surface flux inferred area change from the total area change (colour scale in Figure 3.6). Area change has units of 1×10^7 m^2.

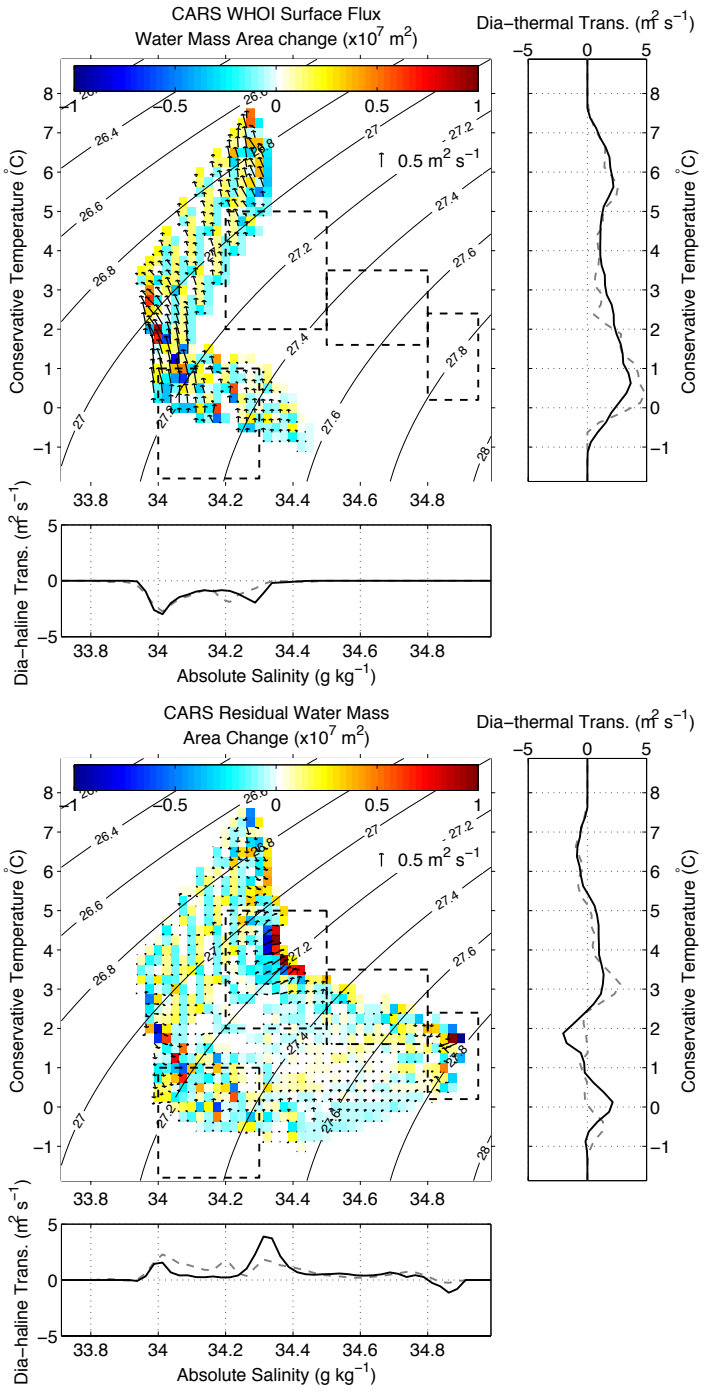

Figure 3.10: As in Figure 3.7 but showing dia-surface transformations and $\Theta - S$ area change inferred from the WHOI surface flux climatology (upper plots), and the resultant residual dia-surface transformations and $\Theta - S$ area change (lower plots) from the CARS climatology. The surface flux area change and associated dia-surface transformations are determined cumulatively from the surface heat and freshwater fluxes between early and late summer. The residual area change and associated dia-surface transformations are calculated by subtracting the sea surface flux inferred area change from the total area change (colour scale in Figure 3.7). Area change has units of 1×10^7 m^2.

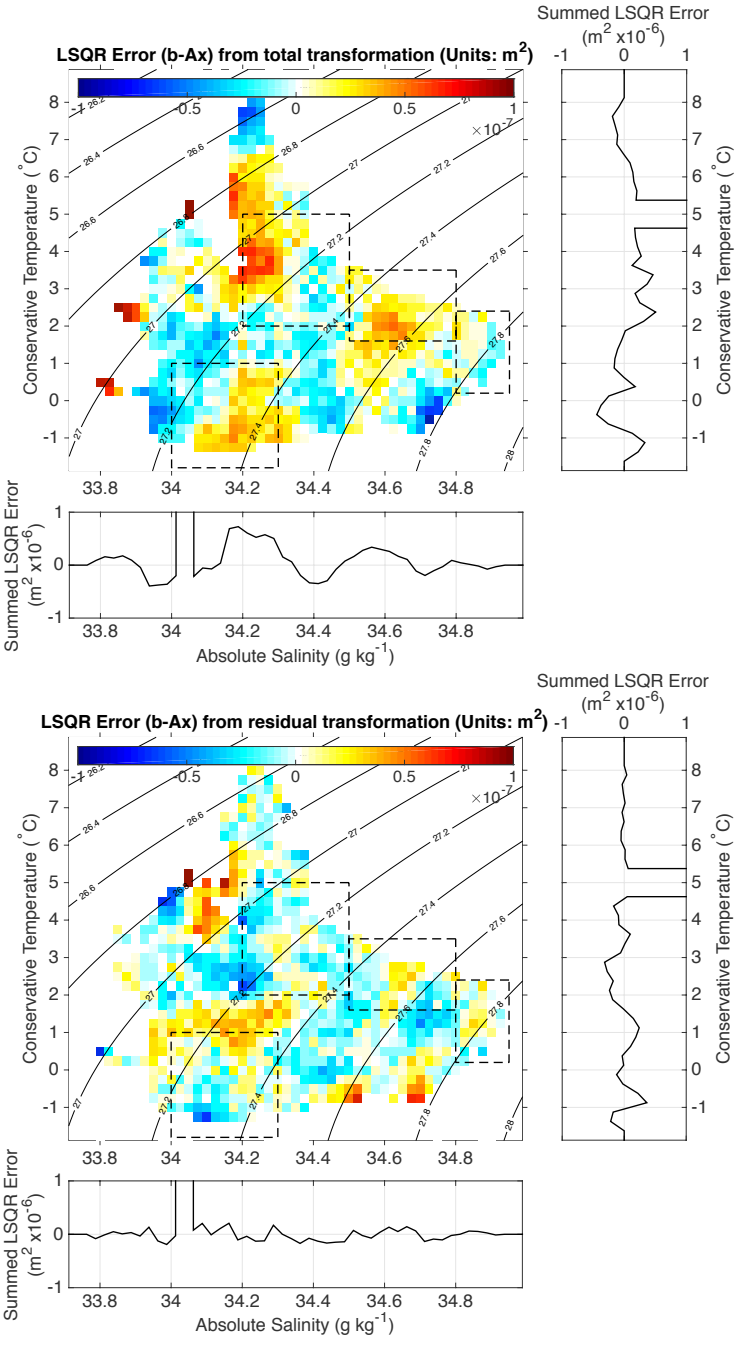

Figure 3.11: Error in the least squares minimisation (i.e. $\mathbf{b} - \mathbf{Ax}$) from the calculation of the total dia-surface transformations shown in Figure 3.6 and the residual dia-surface transformations shown in the lower plot of Figure 3.9. The black curves plotted in the lower and right panels show the this error summed across all Θ and S respectively. Error has units of m^2. The maximum residual error reaches $0.02\mathrm{m}^2$ compared to the the area change which is $\mathcal{O}(10^7)$.

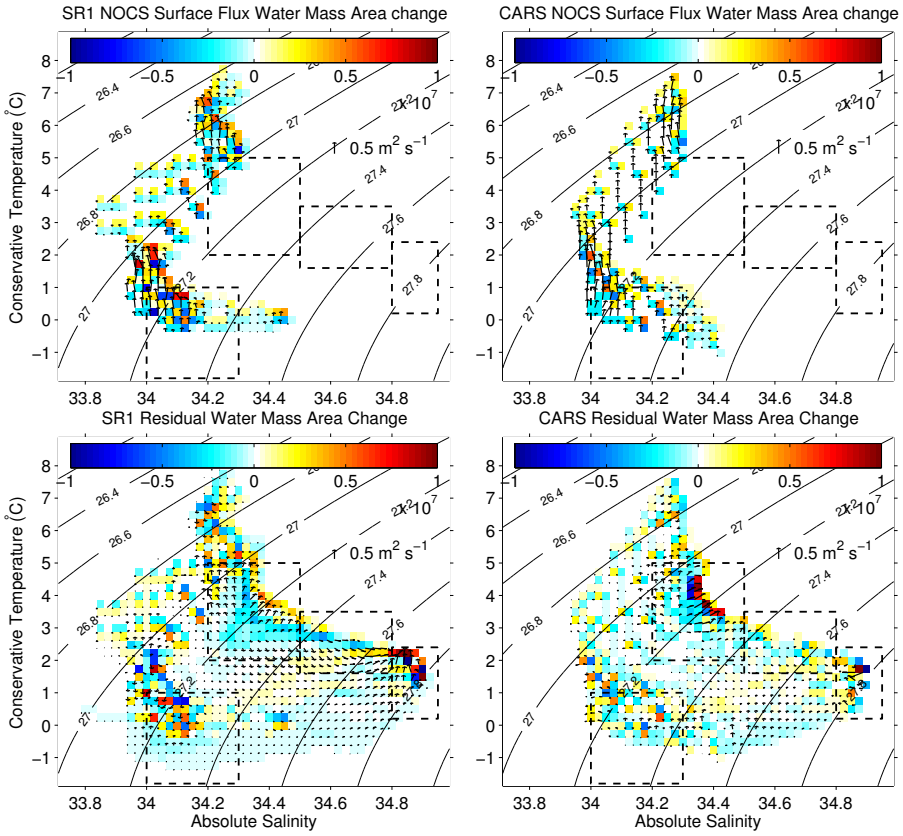

Figure 3.12: As in Figures 3.9 and 3.10 but showing dia-surface transformations and $\Theta - S$ area change inferred from the NOCSv2 surface flux climatology (top row) and inferred residual change (bottom row) for the SR1b section occupations (left column) and the CARS climatology (right column).

3.5 Austral winter thermohaline water mass changes along Drake Passage in a seasonal climatology

The early to late summer changes along Drake Passage within thermohaline coordinates according to the SR1b section occupations and the CARS seasonal climatology agree well, providing confidence in the use of both datasets especially given the sparse temporal nature of the SR1b section occupations and the impact of mesoscale variability in this dataset. We will now discuss the entire seasonal cycle more fully by analysing the winter water mass area changes along Drake Passage using the CARS climatology over the winter period from March to September. It is important to note that there is no air/sea flux data available in the southernmost region of the SR1b section, so that important information regarding the processes affecting AAWW formation is absent from the coldest regions of $\Theta - S$ space in Figures 3.13 and 3.14 as highlighted by the grey stippling in these figures. The total water mass area change and the associated dia-surface transformation (Figure 3.13) in general indicate a pattern of water mass area re-distribution that opposes the change from early to late summer (e.g. Figure 3.7). At

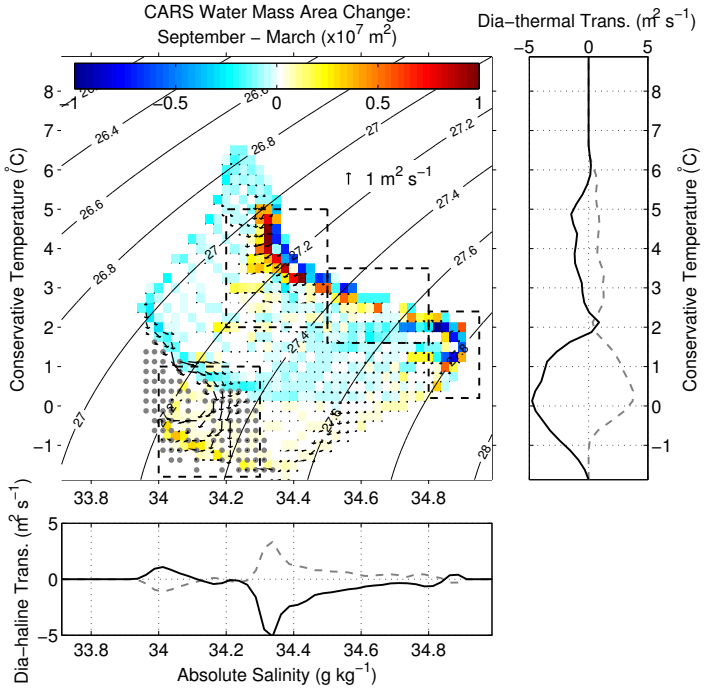

Figure 3.13: Seasonal winter (March to September) change of $\Theta - S$ area change and associated dia-surface transformations from the CARS seasonal climatology (right column). The right and lower panels are the summed diathermal and diahaline transformations respectively (black lines: winter fluxes, grey lines: summer fluxes). Grey stippling indicates $\Theta - S$ classes in which air/sea flux data was unavailable at some point between March and September. Area change has units of 1×10^7 m^2. Transformations have units of m^2 s^{-1}. The dashed boxes show the locations of (from left to right) AAWW, AAIW, UCDW and LCDW.

the surface (fresher region in $\Theta - S$ space) there is a cooling and salinification. In the AAIW there is a general freshening and cooling, and a warming and freshening in the UCDW. There is a slight divergence of vectors in the LCDW, with an increase of water mass area in the region of highest S, and at Θ<1°C there is a cooling.

The dia-surface transformations inferred from air/sea fluxes (Figure 3.14; top panel) maintain a negative diahaline component throughout the winter season so that buoyancy loss is driven by a strong negative diathermal transformation. The freshening implied by the surface air/sea fluxes highlights the importance of mixing in driving the positive diahaline transformation in surface waters (low S, Figure 3.13). This process can be seen in Figure 3.14 (bottom panel) as a convergence of vectors at S ~34.3 g kg^{-1} and Θ ~4°C. Thus, the general seasonal change in water mass area during winter, in regions unaffected by sea-ice, is driven by a balance between the sign of the surface buoyancy inferred diathermal transformation and the residual dia-surface transformation controlled by the interaction through mixing of the surface water masses and the colder and saltier deep water.

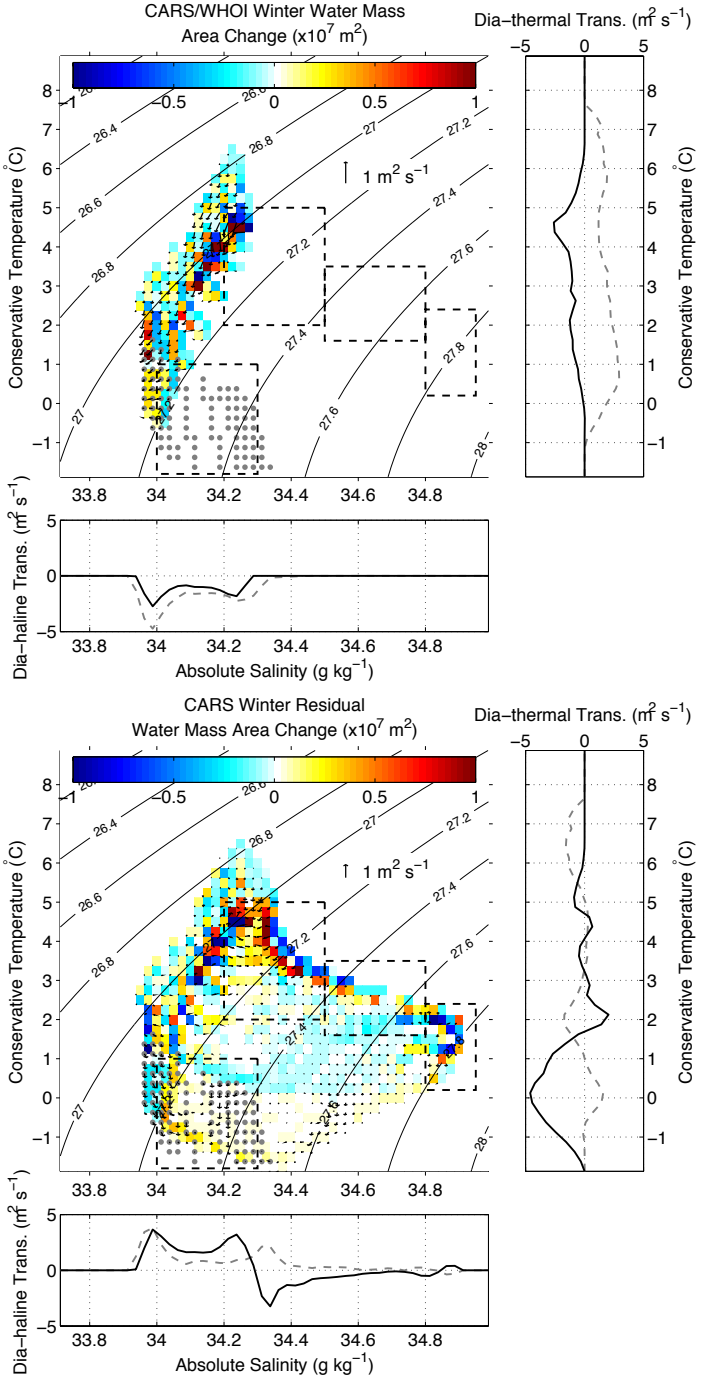

Figure 3.14: As in Figure 3.13 but showing the seasonal winter change of water mass area and associated dia-surface transformations inferred using the WHOI surface flux climatology (top), and the seasonal winter change of the residual water mass area and associated dia-surface transformations (bottom) calculated by removing the water mass area change change due to air/sea fluxes (top panel) from the total winter change shown in Figure 3.13. Again the arrows represent the associated dia-surface transformations inferred from the residual area change. Area change has units of 1×10^7 m^2.

3.6 Projection of thermohaline changes into Eulerian coordinates

A projection into a fixed geographical Eulerian coordinate system of the water mass changes and the implied dia-surface transformations calculated within thermohaline coordinates provides a visualisation that is directly comparable to the changes shown in the bottom two panels of Figure 3.1. This was done by finding the observations in Eulerian coordinates of Θ and S that match each class in thermohaline coordinates, and assigning the diathermal and diahaline components of the area weighted transformations to the corresponding latitude and pressure. These values were converted to a Θ or S change through multiplication with the grid spacing of Θ or S in thermohaline coordinates respectively, and the time difference from early to later summer, which was 3.5 months. To reduce noise caused by the loss of information resulting from the initial projection into $\Theta - S$ space, this re-projection was performed individually with each SR1b section used for the calculation of water mass area change and the resultant Θ or S change was averaged. Such loss of information is associated with the process of averaging in $\Theta - S$ space, which removes some of variability associated with the positions of each water mass in geographical coordinates. For the CARS climatology the re-projection was performed for each month from November to February and the resultant Θ or S change was then averaged for this period.

A comparison between the re-projected changes of Θ and S in latitude/pressure coordinates in both datasets is promising (Figures 3.15 and 3.16/3.17 and 3.18; SR1b/CARS respectively), the exception being the southernmost region of the SR1b section occupation re-projection which have strong increases in both Θ and S that could be the result of particularly cold water masses which warm strongly according to our analysis but are only observed a small number of times. As these waters do not exist at all in CARS, this intense warming is not seen. The SR1b section data show changes in Θ and S down to 3000 m and use the dia-surface transformations derived from the full ocean depth section occupations. Of particular interest is a freshening and slight warming of the saltier LCDW, an opposing cooling and increase in S in the deeper variety of the UCDW, a slight warming and salinification of the shallower UCDW and AAIW, and a warming of the deep waters near the Antarctic continent. A comparison between the re-projected changes in Θ and S, and the changes shown in the bottom rows of Figure 3.1 suggest a better agreement with the CARS change. That the re-projected changes in Θ and S from the SR1b section occupations are similar to both the realisations of changes in Θ and S from the CARS climatology suggest that this method has successfully removed the aliased adiabatic mesoscale variability that originally dominated the changes shown in Figure 3.1.

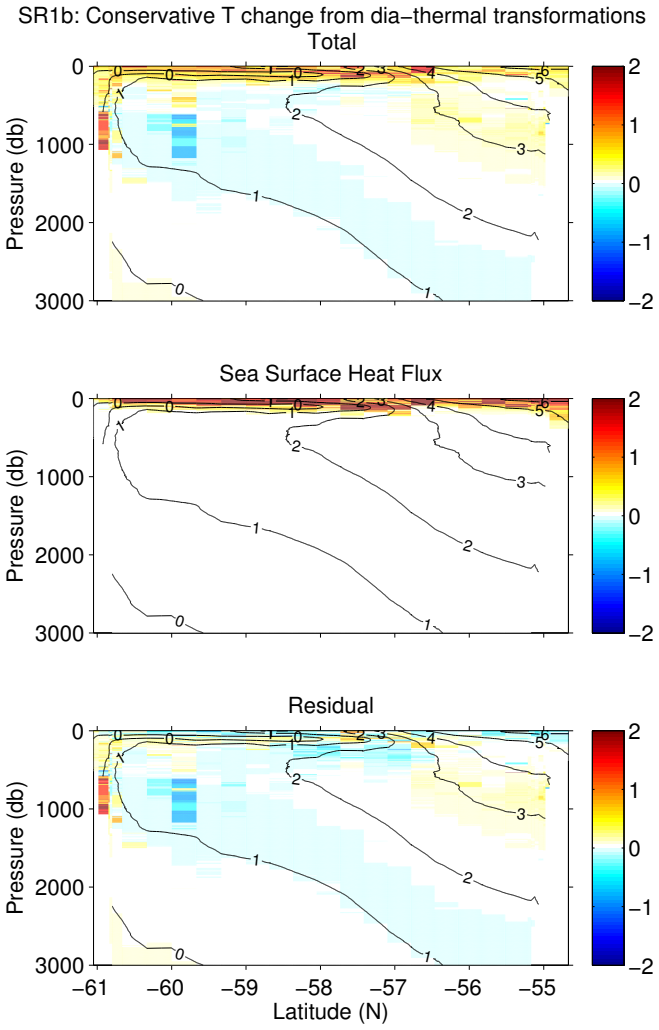

Figure 3.15: The implied early to late summer change in Θ calculated from the total (top), surface buoyancy inferred (middle) and residual (bottom) fluxes of water mass area calculated using the SR1b section occupations down to 3000m and the WHOI air/sea flux product. Black contour lines indicate mean Θ. Units °C.

3.7 Discussion and Interpretation

The general picture of the Southern Ocean overturning is well established, where the prevailing westerly wind drives upwelling of LCDW and UCDW which are transformed by air-sea-ice buoyancy exchange and mixing (Rintoul and Naveira-Garabato, 2013). Depending on the sign of these buoyancy fluxes, these deep water masses are either made denser and sink as AABW close to the Antarctic continent, or are made more buoyant and are eventually subducted equatorward of the PF as either AAIW or SAMW (Speer et al., 2000; Talley, 2013). The impact of seasonality on the water masses of

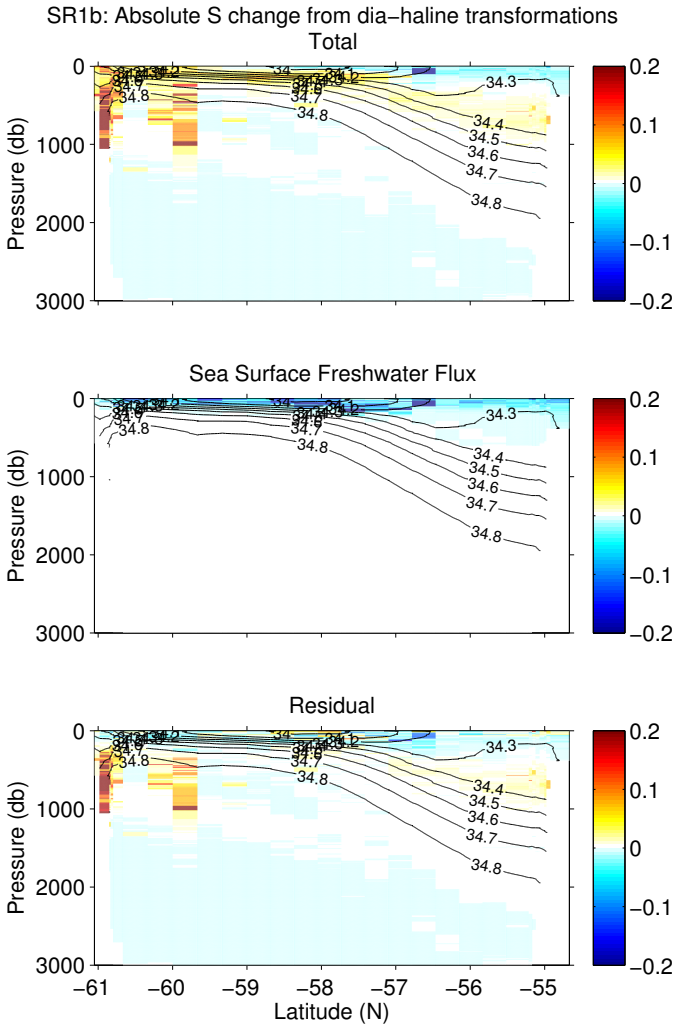

Figure 3.16: As in Figure 3.15 but showing the implied seasonal change in S. Black contour lines indicate mean S. Units g kg^{-1}.

the Southern Ocean is less well known as a result of a poor understanding of air-sea-ice buoyancy fluxes during the austral winter due to a lack of observations (Schulz et al., 2012). For example, the presence of cold/fresh AAWW and its seasonal cycle of formation/destruction as the remnant of the winter mixed layer is accepted (Park et al., 1998), but the role of AAWW in establishing the characteristic salinity minimum of AAIW is controversial (Naveira Garabato et al., 2009). Naveira Garabato et al. (2009) attribute the formation of AAIW to the year-round frontal mesoscale subduction of AAWW and relate interannual changes in properties of AAIW within Drake Passage to the properties of AAWW as set during the winter by the major modes of Southern Hemisphere climate variability. This is contradictory to the notion that AAIW is formed during the winter at specific locations in the South Pacific and South Atlantic (Talley, 1996).

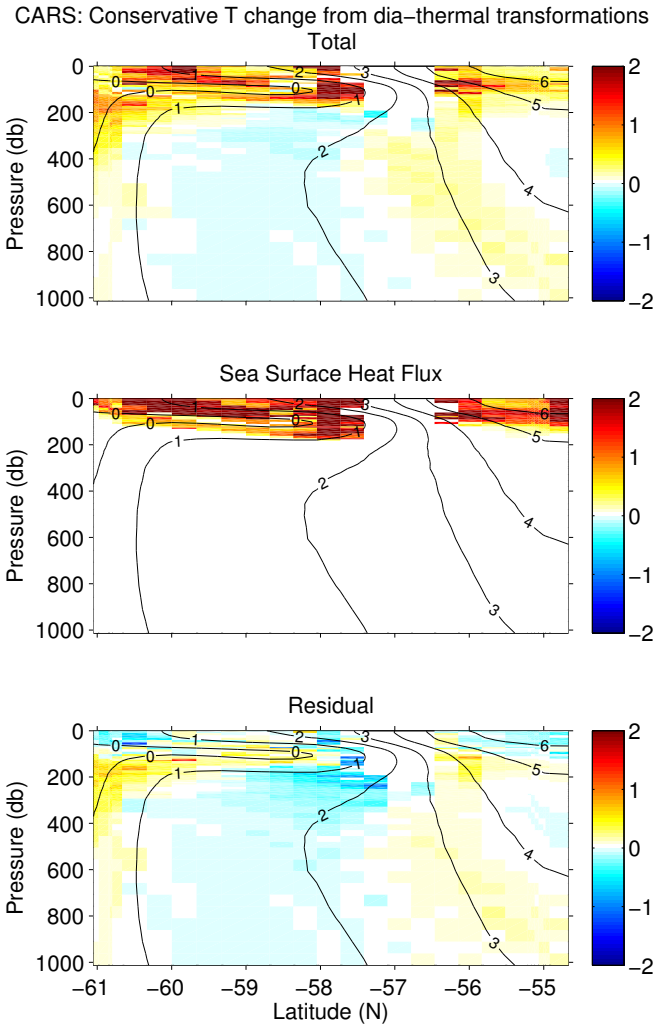

Figure 3.17: The implied early to late summer change in Θ calculated from the total (top), surface buoyancy inferred (middle) and residual (bottom) fluxes of water mass area calculated using the CARS seasonal climatology and the WHOI air/sea flux product. Black contour lines indicate mean Θ. Units °C.

From the analysis of seasonal thermohaline water mass area distribution along Drake Passage, we propose that it is possible to resolve the upwelling (CDW) and downwelling (AAIW/SAMW) limbs of the Southern Ocean overturning within Drake Passage that are enabled by the seasonal changes of buoyancy exchanged between the atmosphere and ocean. Note that although upwelling and downwelling may be driven by Ekman pumping, the transformation from one water mass to another requires surface buoyancy fluxes. The formation and gradual subduction of AAIW is evidenced in the region of $\Theta - S$ space centred at S ~34.3 g kg^{-1} and Θ ~4°C in Figures 3.3-3.14 from both the section occupations and the seasonal climatology. Firstly, in this region of $\Theta - S$ space, the early summer $\Theta - S$ profiles in Figure 3.3 (top row) show the distinct S-minimum characteristic of AAIW. By late summer (bottom row, Figure 3.3) this S-minimum is

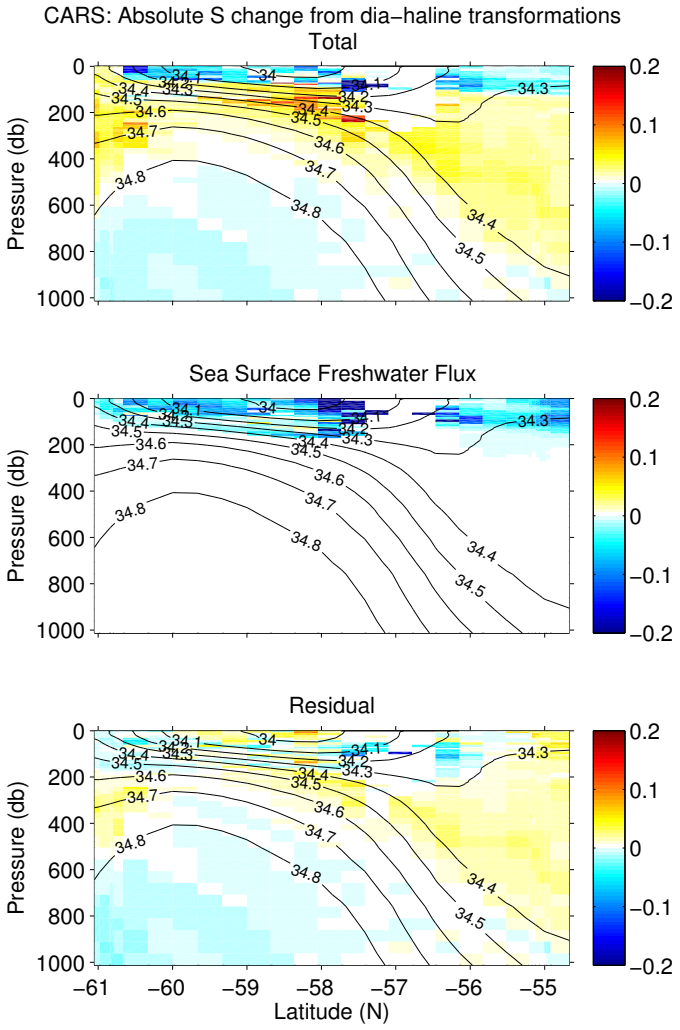

Figure 3.18: As in Figure 3.17 but showing the implied seasonal change in S. Black contour lines indicate mean S. Units g kg^{-1}.

less clear. This process is similarly manifest in the change of water mass area from early to late summer in both datasets as an apparent isopycnal redistribution of water mass area to a warmer and saltier region of $\Theta - S$ space, emphasised by a positive diathermal and diahaline transformation. AAWW is eroded during the summer, becoming warmer through diapycnal mixing from above emphasised by the convergence of positive and negative residual diathermal transformations. Regarding upwelling and transformation of CDW, the UCDW between 34.4 and 34.8 g kg^{-1} and at Θ>1°C is in general getting saltier, the warmest variety is getting warmer, and the coldest variety of UCDW is getting colder (see Figures 3.15-3.18). Finally, the salty LCDW (S>34.8 g kg^{-1}) gets slightly warmer and fresher during the summer.

In comparison, during winter (Figures 3.13-3.14) we see a gain in water mass area in the region of $\Theta - S$ space associated with the S-minimum of AAIW, with negative

diathermal and diahaline transformations and an isopycnal redistribution of water mass area. Further, by the end of winter the S-minimum is re-established, signifying the presence of a colder and fresher variety of AAIW. AAWW formation is extensive but we have no knowledge of the actual air-sea-ice buoyancy exchange that drives AAWW formation. We do see a residual salinification and cooling of surface water north of the PF despite consistently negative E-P fluxes. A positive diathermal and negative diahaline transformation in the UCDW highlight a warming and freshening during the winter, in comparison to a slight cooling and salinification of the LCDW.

The following interpretation is also represented schematically in Figure 3.19. These observations suggest that AAIW is gradually subducted and transformed during the summer and formed in excess during the winter. In winter, the S-minimum of AAIW is established as UCDW (which gets fresher), surface waters (which get cooler and saltier) and AAWW (as it is formed during the winter) mix. The warming and salinification of AAIW during the summer emphasises the importance of cold and fresh AAWW in maintaining the S-minimum of AAIW, suggesting the interaction of these water masses is reduced during the course of the summer as AAWW is eroded and made less dense once capped. If mixing between the surface water, AAIW and UCDW continued during the summer (with a reduced cold/fresh source of AAWW), the resultant re-distribution of water mass area would reflect the isopycnal shift we observe in $\Theta - S$ space, represented schematically in Figure 3.5(c). Further, the S-minimum of the $\Theta - S$ profiles in early summer along the 27.2 isopycnal highlights the pathway for mixing of AAWW across the PF through frontal mesoscale processes.

In terms of the upwelling and transformation of LCDW and UCDW, what we observe seems to be an imbalance between the continual wind-driven upwelling of LCDW and UCDW and the transformation of these water masses through mixing. The patterns of change shown in Figures 3.15-3.18 during the summer, where we observe a warming and freshening in the cold/salty LCDW and a salinification and cooling in the UCDW, most likely suggest recharge of UCDW through mechanical wind-driven upwelling, and the slight erosion of LCDW as it is mixed with the fresher UCDW. During the winter, UCDW gets fresher and slightly warmer as it mixes with AAIW and surface water, but the LDCW seems to get saltier and colder. As UCDW gets lighter during the winter, mixing between the LCDW and UCDW is reduced, so that the upwelling rate of LCDW exceeds the transformation of LCDW to lighter water masses through mixing, thus producing the apparent salinification and cooling that we observe in thermohaline coordinates.

Based on the seasonal change in water mass area of LCDW during the summer, a meridional transport anomaly of LCDW can be roughly estimated. We take the sum of the water mass area change within the region of $\Theta - S$ space associated with LCDW (Figure 3.6; far right dashed box) and multiply by an approximation of the zonal extent of LCDW. This approximation is derived by calculating the fractional area associated

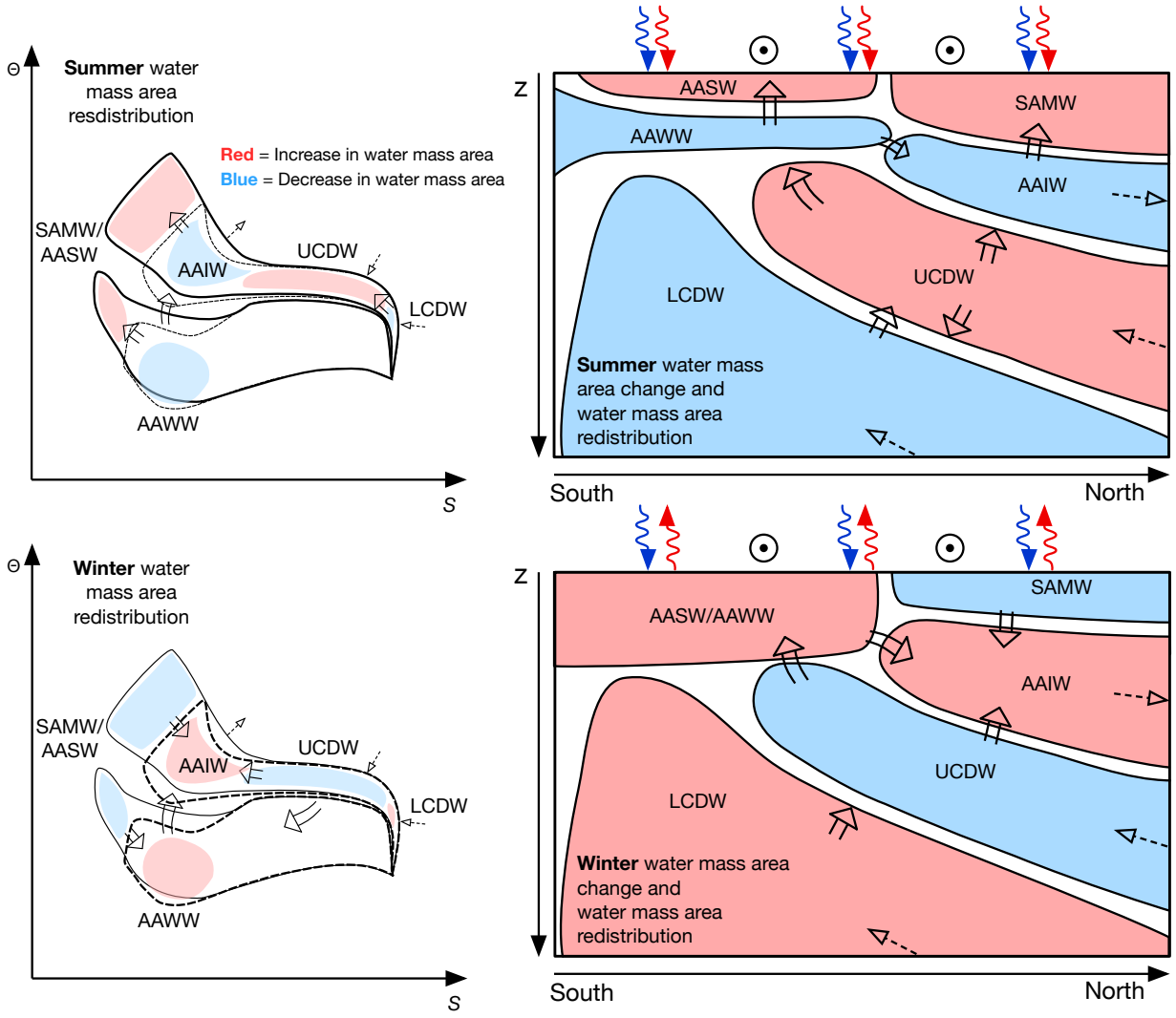

Figure 3.19: A schematic representing the changes in the distribution of water mass area during the summer (top) and winter (bottom) in thermohaline coordinates (left) and Eulerian coordinates (depth/latitude; right) highlighting the processes affecting the key water masses within Drake Passage. In both the solid black arrows indicate the transformation of water mass area and the dashed black arrows represent a advection of water into and out of the geographical domain from which water mass area is calculated. The colour change represents the change in water mass area (red=increase, blue=decrease). In the thermohaline coordinate schematic, the solid line and dashed lines are the summer and winter distribution of water mass area respectively. In the Eulerian coordinate schematic the red and blue arrows represent fluxes of heat and freshwater respectively in or out of the ocean and the black circles with dots represent the direction of the zonal winds out of the page.

with LCDW according to the CARS mean state estimate (∼0.2) in a zonal transect at ∼57°S (the mean latitude of the SR1b section), and multiplying by the circumpolar width at this latitude (∼21,400 km). This assumes that the zonal width of LCDW is much greater than the thickness. This yields a seasonal transport anomaly estimate for LCDW of approximately 10 Sv (1 Sv $= 1 \times 10^6$ m^3 s^{-1}) directed southward, interpreted as a transformation of LCDW to lighter, UCDW and near-surface water. This agrees well with the similar estimate of 13 Sv by Talley (2013).

The above interpretation of the results presented in sections 3.3 to 3.6 are at this stage speculative given the limited available data and the potential for unknown changes of water mass area as a consequence of changes in the movement of water across the geographical boundary of the domain used to calculate water mass area. Changes in the meridional wind-driven upwelling of CDW, downwelling of AAIW and the zonal transport of the ACC could alias as a dia-surface transformation that may be misinterpreted above (panel (b), Figure 3.5). However, preliminary volumetric analysis of the entire Southern Ocean in CARS and an ocean circulation state estimate (ECCO;Wunsch and Heimbach, 2013a) suggest similar seasonal variations of water mass volume. An important consideration is also the sensitivity of this method to the chosen time-interval. This will depend on the accuracy and reliability of the observational data being used relative to the size of the signal in question and could be tested using a numerical model.

3.8 Summary and Conclusions

A method is presented to diagnose seasonal changes in water mass properties in thermohaline coordinates. The use of this coordinate system naturally removes the adiabatic effects of mesoscale variability to enable a clearer interpretation of the diabatic processes that drive water mass changes. The early to late summer seasonal changes in two datasets of Θ and S observations were compared. The first dataset comprising 20 repeat hydrographic sections along Drake Passage, the second a monthly seasonal climatology of the surface 1000m of the ocean interpolated to the station positions used in the sections. In an Eulerian, fixed geographical coordinate system the seasonal change according to the two datasets vary due to the presence of adiabatic heaving of isopycnals by mesoscale processes in the section occupations. The main goal of this chapter, was therefore to present the seasonal change in the section occupations and the seasonal climatology in a manner that is not aliased by these mesoscale processes.

Both datasets were projected into thermohaline coordinates by determining the water mass area associated with each $\Theta - S$ class within $\Theta - S$ space. The change in distribution of water mass area within $\Theta - S$ space from early to late summer was then used to estimate the diathermal and diahaline transformation of water mass area, representing the amount of water transformed by the difference between each grid cell in $\Theta - S$ space

to account for the redistribution of water mass area from early to late summer. The resultant change in water mass area and the inferred dia-surface transformations are similar according to both datasets. A clear redistribution of sub-surface water mass area is similarly evident in both datasets including a warming of the seasonally formed AAWW, a warming and salinification of AAIW, salinification of UCDW and freshening of LCDW.

Using air/sea flux datasets of heat and E-P, the dia-surface transformation of water mass area and the resultant water mass area change were determined. For both the section occupations and the seasonal climatology, these dia-surface transformations indicate a warming and freshening of surface waters. Subtracting the water mass area change inferred using surface buoyancy fluxes from the seasonal water mass area change gives a residual water mass area change and therefore a residual dia-surface transformation. The residual water mass area change and the implied transformation highlight in particular the seasonal erosion of AAWW by diapycnal mixing given the convergent nature and non-isopycnal direction of the residual vectors.

Winter changes in water mass area distribution were also explored using the seasonal climatology. The change in water mass area from March to September and the derived dia-surface transformations show an opposing pattern of change to that observed during the summer. The determination of dia-surface transformations from air/sea fluxes is limited due to a lack of air/sea flux data during the winter especially in ice covered regions of Drake Passage.

Our analysis is consistent with the superposition of continual wind-driven overturning and seasonally variable water mass transformation. In the winter, strong surface cooling and consequent deep mixed layers form a large amount of AAWW and AAIW out of surface waters and underlying remnant AAWW and CDW. This depletes the CDW layer and increases the AAIW layer despite the likely constant inflow of CDW and outflow of AAIW. During the summer AAWW is eroded through surface warming and interior mixing and AAIW is exported. Meanwhile the CDW layer is inflated suggesting summertime wind driven recharge in preparation for AAWW and AAIW formation the following winter.

Chapter 4

The Southern Ocean Overturning in Thermohaline Coordinates

Abstract

The seasonal variability of Southern Ocean water masses are examined in thermohaline coordinates using an ocean model and an observationally based seasonal climatology. Changes in the volumetric distribution of water masses are related to the transformation of water across isotherms and isohalines by surface buoyancy forcing and sub-surface mixing. The diabatic transformation of the Circumpolar Deep Waters (CDW) in the Southern Ocean takes place over the course of a season. During the winter CDW upwelling occurs through mixing with the overlying Antarctic Winter Water (AAWW). AAWW which is formed by intense wintertime surface cooling, is made progressively saltier due to brine-rejection from sea-ice formation. AAWW only mixes with CDW when it reaches a critical salinity set by cabbeling. The AAWW that becomes saltier than this critical salinity becomes unstable to cabbeling, driving mixing between the AAWW layer and the CDW layer. This mixing will erode the top of the CDW layer until the upper AAWW layer is lighter than the underlying CDW. During the summer AAIW is formed from the AAWW layer though surface warming and freshening by melting sea-ice. This highlights the importance of seasonally varying air–ice–sea buoyancy fluxes in the diabatic closure of the Southern Ocean meridional overturning circulation.

4.1 Introduction

The upwelling, transformation and downwelling of all major water masses within the Southern Ocean regulates the heat, freshwater and carbon budgets of the world's oceans (Sabine et al., 2004; Purkey and Johnson, 2010; Rintoul and Naveira-Garabato, 2013; Talley, 2013). These processes are governed by a balance between wind-driven upwelling/downwelling, eddy stirring/advection, isopycnal/diapycnal mixing and air–ice–sea buoyancy fluxes (Speer et al., 2000; Naveira Garabato et al., 2007; Zika et al., 2009; Abernathey et al., 2011; Marshall and Speer, 2012). The prevailing westerly winds over the Southern Ocean drive an equatorward mass transport through an upwelling poleward of the zonal wind-stress maximum and a downwelling equatorward of the zonal wind-stress maximum. This overturns isopycnals and sets up the geostrophic Antarctic Circumpolar Current (ACC; top panel, Figure 4.1). Baroclinic instabilities within the ACC form eddies which act to shoal isopycnals balancing the action of the winds. These eddies further act to transport mass poleward.

A residual overturning circulation results from the balance between the equatorward mass transport by winds and the poleward transport by eddies (e.g. Marshall and Radko, 2003). This residual meridional overturning circulation (MOC) manifests as a poleward upwelling of deep water and a equatorward downwelling of mode and intermediate waters above this deep water. Yet, due predominantly to a physical lack of observations, the diabatic processes (i.e. air–sea buoyancy fluxes and sub-surface mixing) that drive the conversion of deep water to mode/intermediate waters are poorly constrained. This not only hinders accurate estimates of the Southern Ocean MOC, but also limits our ability to predict it's fate in a warming climate (Fyfe and Saenko, 2006; Downes et al., 2009; Morrison et al., 2015; Thomas et al., 2015). In particular, most conceptual views of the Southern Ocean MOC use time-mean values for air–ice–sea buoyancy fluxes to explain the net transformation of Upper and Lower Circumpolar Deep Water (UCDW and LCDW) into either Antarctic Bottom Water (AABW) or Antarctic Intermediate Water (AAIW; e.g. Czaja and Marshall, 2015). However, recent studies highlight the importance of seasonally varying air–ice–sea buoyancy fluxes in setting the properties of these water masses (Evans et al., 2014; Abernathey et al., 2016).

A key closure of the Southern Ocean MOC is the formation of AAIW, which forms the downwelling limb of the MOC (bottom panel Figure 4.1; Marshall and Speer, 2012; Talley, 2013). Typically, it is thought that AAIW formation occurs in the Indian and South Pacific Oceans during the winter, when deepening of the mixed layer also forms the overlying Subantarctic Mode Water from upwelled UCDW. While upwelling LCDW typically occurs in the Atlantic sector of the Southern Ocean, where it is cooled to form AABW. Recent studies also show that AAIW is formed through the northward ventilation of Antarctic Winter Water (AAWW) near Drake Passage (Naveira Garabato

et al., 2009; Evans et al., 2014). This AAWW is the remanent of the winter-time mixed layer formed in part from the underlying CDW.

Based on the work of Walin (1982) and Speer (1993), Evans et al. (2014) developed a framework to explore the temporal variability of water masses in terms of the transformation of water between water mass classes. This is achieved by first projecting temperature and salinity data into thermohaline coordinates as a volumetric distribution. The transformations across isotherms and isohalines are then inferred from changes in this volumetric distribution. According to Walin (1982) these transformations, equivalent to a volume flux, can be expressed as diabatic transformations due to air–sea fluxes of buoyancy at the sea-surface and mixing, or as volume change through transport variations across a fixed boundary that intersects a given isotherm/isohaline. The air–sea flux term can be determined using the methodology developed by Speer (1993), and compared to the transport terms when the velocities are known (e.g. in an ocean model; chapter 2), to solve for the mixing term. Thus, the temporal variability of water masses within a region of the ocean can be dissected into the variability driven by air–sea buoyancy exchange, mixing and transport, and therefore related to the important dynamical processes associated with that region.

Using this framework, Evans et al. (2014) investigated the seasonal variations in the thermohaline distribution of water masses in a hydrographic transect across Drake Passage. This highlighted the imprint of the Southern Ocean overturning on the seasonal inflation and deflation of Antarctic winter water (AAWW), AAIW and CDW. During the winter, air–sea buoyancy fluxes drive a cooling and formation of AAWW and AAIW from the underlying CDW and previously formed AAWW. This deflated the CDW layer at a rate that exceeded the wind-driven inflow. The rate of AAIW formation similarly exceeds the export, so the AAIW layer thickness increases. AAWW is eroded by surface warming during the summer, while the rate of AAIW export exceeds AAIW formation. Reduced erosion of the CDW layer enables a wind-driven inflation of CDW during the summer.

Using both models and observations, this chapter explores the seasonal variations in the volumetric distribution of water masses in the whole Southern Ocean to assess the role of air–ice–sea fluxes and mixing in setting the seasonal formation and destruction of AAWW, CDW and AAIW. From these analyses we show that seasonal variations in the air–ice–sea buoyancy fluxes play a critical role in the wintertime upwelling of CDW through mixing with overlying AAWW. Summertime warming and freshening forms AAIW through heat exchange with the atmosphere and sea-ice melt. Mixing between CDW and AAWW is governed by cabbeling. The next section will discuss the water mass framework used in this analysis, while the data used is described in section 4.3. The variability of the Southern Ocean water masses and the role of cabbeling in the wintertime upwelling of CDW is discussed in sections 4.4 and 4.5. These analyses are summarised and concluded in the final section.

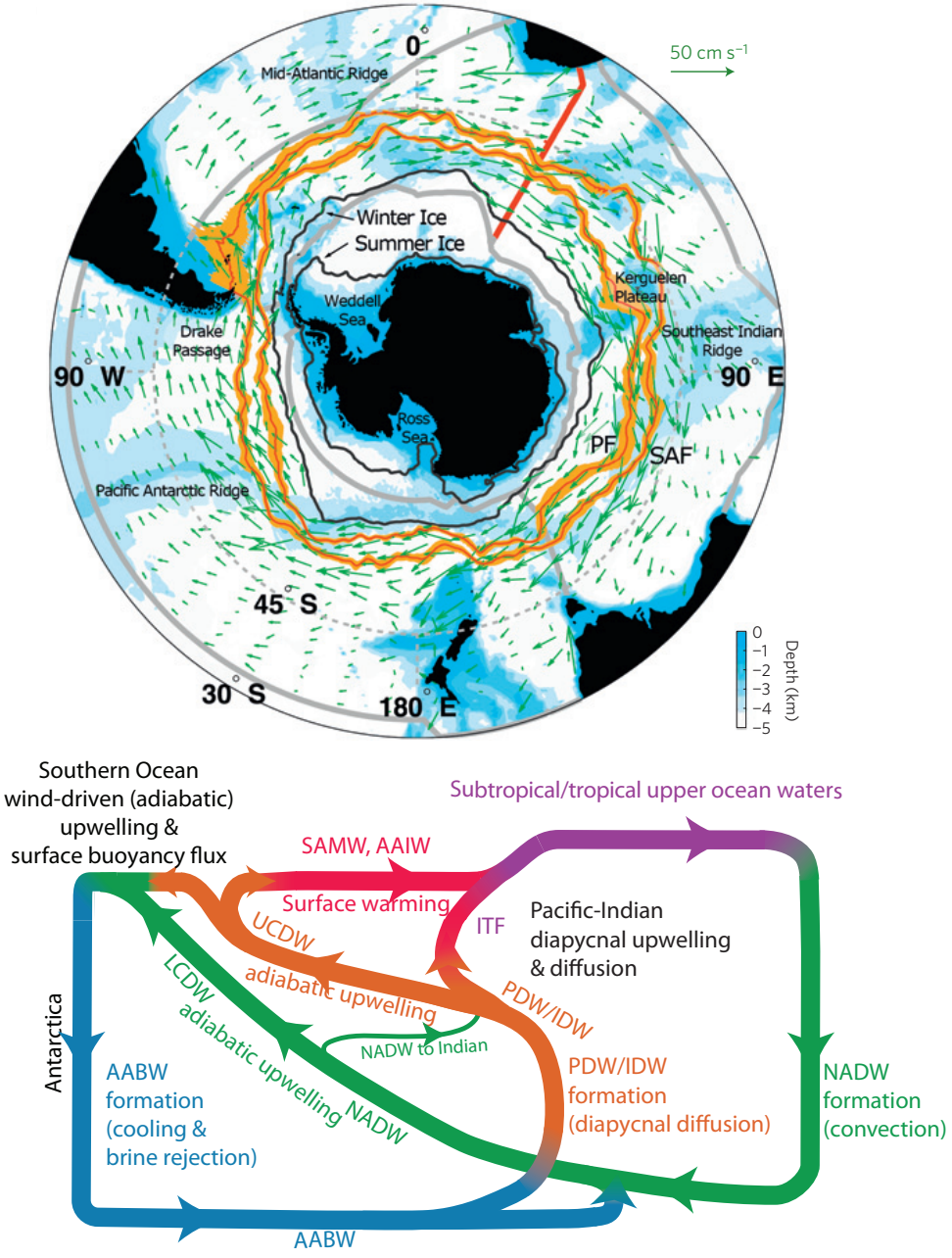

Figure 4.1: ((left) The Southern Ocean circulation as shown by observations, adapted from Marshall and Speer (2012). The orange curve represents the climatological position and latitudinal variance (thickness of the line) of the subantarctic front (SAF) and polar front (PF). The green arrows show the speed and direction of surface ocean currents of the ACC as observed by floating drifters at a depth of 15m. The ocean depth is coloured in blue and the summertime minimum and wintertime maximum sea ice extent are shown in black. (right) Schematic representation of the Southern Ocean overturning estimated from shipboard CTD sections from Talley (2013). According to current understanding upwelled LCDW cools to form AABW. This AABW is diffusively upwelled Indian and Pacific Oceans forming Indian Deep Water (IDW) and and Pacific Deep Water (PDW). These form upwelling UCDW which when exposed to surface warming forms AAIW.

4.2 Methodology

The aim of this analysis is to separate the diabatic and adiabatic variability of oceanic temperature (Θ) and salinity (S), and to understand the role of this variability in the Southern Ocean MOC. Walin (1982) introduced a framework to relate the intensity of surface heat fluxes to the strength of the MOC, comparing volumes of water in Θ classes to the dia-surface transformations of water between Θ classes by air–sea heat fluxes and mixing. Here, we extend this analysis to a time-varying ocean (Evans et al., 2014) and define a volumetric water mass distribution (V) in terms of both Θ and S.

$$V(\Theta, S, t) = \iiint \Pi(\Theta, \Theta^*)\, \Pi(S, S^*) \mathrm{d}x\mathrm{d}y\mathrm{d}z. \tag{4.1}$$

Here Π is a boxcar function that is either 1 when Θ and S are within the range defined by a given Θ-S class, or otherwise 0. Each Θ-S class is defined at $\Theta^* = \Theta \pm \Delta\Theta/2$ and $S^* = S \pm \Delta S/2$. In practice, we define $\Delta\Theta$ and ΔS as 0.5°C and 0.05 g kg^{-1} respectively, giving a volume with units of m^3/°C/g kg^{-1}.

For a given V that is entirely enclosed between Θ^*, S^* and the sea surface, the rate of change of V becomes:

$$\frac{dV}{dt} = G_\Theta(\Theta - \Delta\Theta/2, S) - G_\Theta(\Theta + \Delta\Theta/2, S) + G_S(\Theta, S - \Delta S/2) - G_S(\Theta, S + \Delta S/2), \tag{4.2}$$

where G_Θ is the diathermal transformation, in units of m^{3}s^{-1}, across the isotherm defined at $\Theta^* = \Theta + \Delta\Theta/2$ in the range $S \pm \Delta S/2$, and G_S is the diahaline transformation across the isohaline defined at $S^* = S + \Delta S/2$ in the range $\Theta \pm \Delta\Theta/2$. G_Θ and G_S represent the integral of the dia-surface velocity along a surface of constant temperature or salinity.

For the case of an entirely enclosed volume, this represents the diabatic contribution to changes in temperature and salinity, and can be separated into the dia-suface transformations due to air–sea fluxes of heat and freshwater (E_Θ and E_S) and diapycnal and isopycnal mixing (F_Θ and F_S). For example,

$$G_\Theta(\Theta^*, S) = E_\Theta(\Theta^*, S) + F_\Theta(\Theta^*, S). \tag{4.3}$$

Again, E_Θ is the diathermal transformation rate due to the air–sea heat flux, which is defined as:

$$E_\Theta(\Theta^*, S) = \frac{1}{\rho_0 C_p} \frac{\partial Q_\Theta}{\partial \Theta}, \tag{4.4}$$

where,

$$Q_\Theta(\Theta^*, S) = \iint \Pi(\Theta, \Theta^*)\,\Pi(S, S^*)\,q_{net}\,\mathrm{d}x\mathrm{d}y. \tag{4.5}$$

Here q_{net} is the net surface heat flux (W m^{-2}). The equivalent diahaline transformation across S^* due to air–sea freshwater fluxes is:

$$E_S(\Theta, S^*) = S_0\,\frac{\partial Q_S}{\partial S}, \tag{4.6}$$

where,

$$Q_S(\Theta, S^*) = \iint \Pi(\Theta, \Theta^*)\,\Pi(S, S^*)\,f_{net}\,\mathrm{d}x\mathrm{d}y. \tag{4.7}$$

Here f_{net} is the net surface freshwater flux (m s^{-1}).

The diathermal transformation due to mixing, F_Θ, across Θ^* is:

$$F_\Theta(\Theta^*, S) = \int_{\Theta=\Theta^*} \Pi(S, S^*)\,\frac{1}{|\nabla\Theta|}\nabla\cdot\mathbf{K}\nabla\Theta\,\mathrm{d}A. \tag{4.8}$$

The diffusion tensor, $\mathbf{K}$, encompasses the coefficients of both isopycnal and diapycnal mixing.

In the case where a volume is not entirely enclosed by Θ^*, S^* and the sea surface, where for example it is intersected by a fixed boundary, V is in part set by the inflow of water across this boundary. Air–sea fluxes and mixing drive dia-surface transformations across isotherms and isohalines, and transport changes across a fixed boundary imply adiabatic volume changes.

Diagnosing the dia-surface transformations (G) by integrating the dia-surface velocities is impractical. As described in Evans et al. (2014), we therefore diagnose these dia-surface transformations using the volume change, which is more easily calculated. Thus, we build a series of linear equations describing the known volume change of each Θ-S class in terms of the unknown diathermal and diahaline transformations across each isotherm and isohaline. These linear equations can then be solved for the dia-surface transformations using a least squares regression. The divergence of the resultant dia-surface transformations therefore represent a volume change that most closely matches the observed volume change, where each individual dia-surface transformation indicates the volume of water that changes by $\Delta\Theta$ or ΔS within a given time period. The resultant vectors therefore may not represent the actual path of a parcel of water through Θ/S space, but is the most that can be inferred from the available data.

The dia-surface transformations due to air-sea fluxes (E) can be determined independently using (4.4) and (4.6). To determine the volume fluxes, M, due to transport changes at a fixed boundary, transects of Θ, S and transport normal to the boundary from an ocean model are used to determine volume changes within each Θ-S class. The area occupied by a given Θ/S class at the boundary is multiplied by the mean

transport across the boundary through that Θ/S class. As above, we then solve for M using a least squares regression by substituting these volume changes for the total volume change. The dia-thermal and dia-haline transformations due to mixing (F_Θ, F_S) is then easily determined from (4.3), which depending on the geographical domain may or may not include the term M. Dia-surface transformations due to air–sea fluxes and mixing, and volume fluxes due to transport changes are presented in units of Sv, where 1 Sv$= 1 \times 10^6$ m^{3}s^{-1}.

4.3 Data sources

To determine the volumetric distribution of water masses in Θ/S space, this analysis uses Θ and S data from an observationally based seasonal climatology and an ocean state estimate. All data south of 30°S are selected, encompassing the entire Southern Ocean. The diathermal and diahaline transformations determined using these data are compared to those derived from various atmospheric re-analysis products and to the volume changes due to the transport across 30°S in the ocean state estimate.

The seasonal climatology utilised here is the CSIRO Atlas of Regional Seas (CARS) 2009 (Ridgway et al., 2002) accessed at www.cmar.csiro.au/cars. CARS is a global atlas of seasonal water mass properties with a horizontal resolution of 1/2°, that extends to 75°S, derived from all available subsurface data. Using CARS, year-round seasonal mean estimates of potential temperature and practical salinity are calculated from a mean state estimate and the semiannual/annual components of the seasonal cycle. Potential temperature and practical salinity are converted to conservative temperature and absolute salinity according to IOC et al. (2010). Finally, the seasonal mean estimates from CARS extend from the surface to 1000m.

In addition, we use monthly fields (1992–2012) for potential temperature and practical salinity from Estimating the Circulation and Climate of the Ocean version 4 (ECCO v4; Forget and Ponte, 2015). Also available from ECCO v4 are estimates of surface fluxes, velocity and transport, which are used to compare to the volume changes according to the potential temperature and practical salinity fields. ECCO v4 also includes a full sea ice model at the poles, which is encompassed by the surface flux estimates. These data are accessed from http://www.ecco–group.org. Hereinafter, both conservative temperature (CARS) and potential temperature (ECCO v4) will be referred to by Θ, while both absolute salinity (CARS) and practical salinity (ECCO v4) will be referred to by S. As a comparison to both CARS and ECCO v4 we use monthly mean fields for shortwave radiation, longwave radiation, sensible heat flux and latent heat flux from NCEP/NCAR (Kalnay et al., 1996), with a horizontal resolution of ∼1.9° for the period 1948-present. We use fields for evaporation and precipitation from the Woods Hole Oceanographic Institute OAFlux/Global Precipitation Climatology Project (OAFlux)

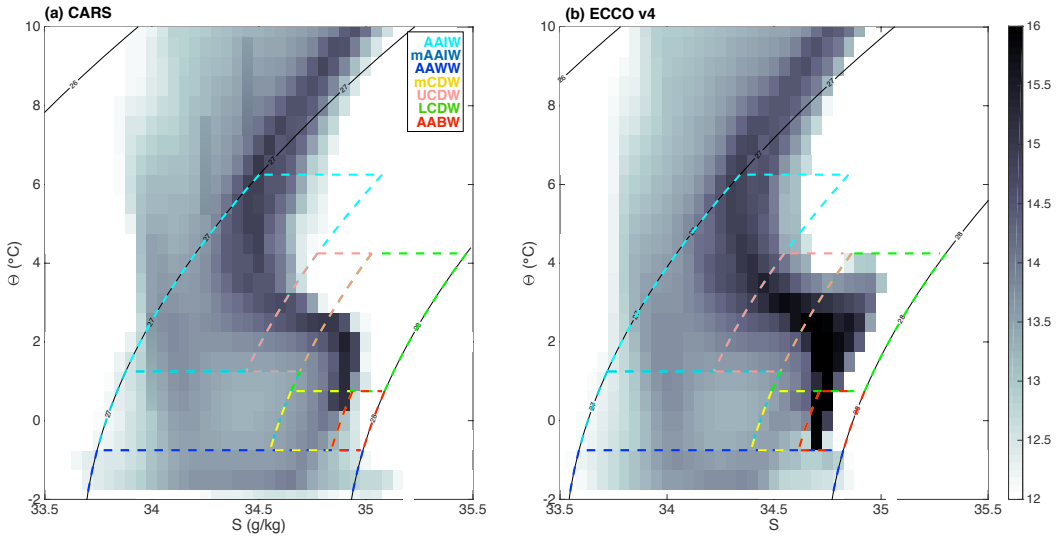

Figure 4.2: (a) Time-mean of $\log_{10}$ water mass volume (in $m^3/°C/(g/kg)$) using CARS south of 30°S, by calculating the volumetric distribution for each month and averaging. Black contours show density anomaly referenced to 0 dbar (σ_0). Coloured boxes represent the nominal definition of each water mass used for this study, enclosed by isotherms and isopycnals. AAIW = Antarctic Intermediate Water, AAWW = Antarctic Winter Water, UCDW = Upper Circumpolar Deep Water, LCDW = Lower Circumpolar Deep Water and AABW = Antarctic Bottom Water. The letter 'm' represents 'modified' (b) Time-mean (1992-2012) of $\log_{10}$ water mass volume (in $m^3/°C/(psu)$) using ECCO v4 south of 30°S. Black contours show density anomaly referenced to 0 dbar (σ_0)

datasets (Yu et al., 2006), which is globally gridded to 1 degree for period 1958-present. We therefore compare volume changes calculated from Θ/S fields in CARS and ECCO v4 to the dia-surface transformation implied by both NCEP/NCAR+OAFlux and ECCO v4 surface fluxes. Note, only the ECCO v4 surface flux estimate includes forcing due to sea-ice, but thermohaline volume changes in CARS should feel the impact of the buoyancy forcing due to the cycle of sea-ice formation. The quality of air–sea flux products in the Southern Ocean are known to be poor (Schulz et al., 2012). The advantage of the framework used here is that the resultant dia-surface transformations by air–sea fluxes can be rationalised by comparison with the volume changes, and we focus on seasonal changes which should be relatively well defined. In addition, a good comparison between NCEP/NCAR+OAFlux and the output from ECCO v4 discussed in the following section provides more confidence in our results.

4.4 Southern Ocean water mass volume variability

In the following section we will discuss the water mass volume distribution of the Southern Ocean according to CARS and ECCO v4. The major Southern Ocean water masses

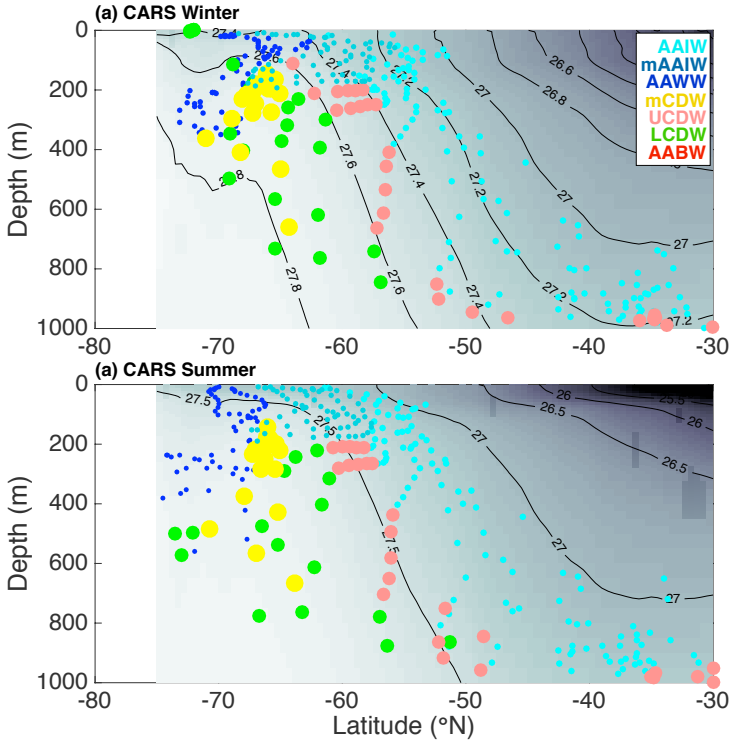

Figure 4.3: (a) Coloured circles represent winter-mean (July-September) position for each water mass defined by the coloured boxes in Figure 4.2 using CARS south of 30°S. Each circle represents an individual Θ/S bin. The size of each circle represents the relative volume of each water mass. Black contours show density anomaly referenced to 0 dbar (σ_0). (b) As in (a) but showing summer-mean (December-February).

will be defined within Θ/S space allowing their variability to be described in terms of the processes driving the dia-surface transformations of water between CDW and AAIW. When projected into Θ/S space the time-mean distribution and structure of water mass volume in CARS and ECCO v4 are very similar (Figure 4.2). In both datasets, a ridge of high volume forms an elongated 'S' that extends from a region of high Θ and S associated with Subantarctic mode water, to the cold and fresh water associated with AAIW. This ridge bends toward the higher salinities characteristic of Upper and Lower CDW (UCDW and LCDW) and then back toward the lower Θ and S associated with AABW. Also evident are two less voluminous ridges of water mass volume connecting the AAWW to the CDW and AAIW. These water masses are labelled as mCDW and mAAIW, indicating a modified variety of the respective water masses. As the CARS dataset does not extend below 1000m the total volume of CDW and AABW is low compared to ECCO v4.

The nominal definitions of each water mass are shown by the coloured boxes in Figure 4.2. Averaging the latitude and depth of the observations used to calculate the volume of each Θ/S bin reveals the familiar layered structure of the Southern Ocean water masses (e.g. Speer et al., 2000; Talley, 2013), validating the water mass definitions

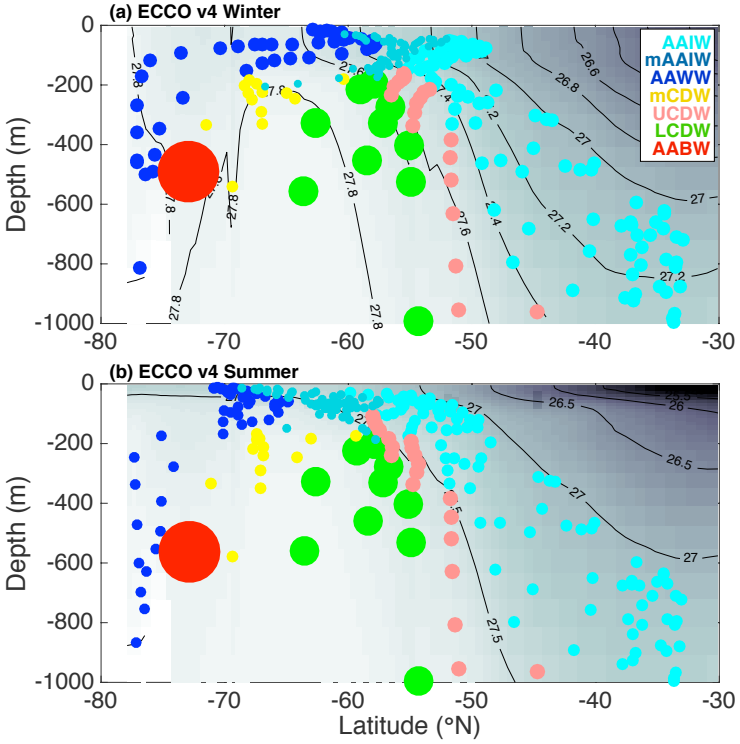

Figure 4.4: As in Figure 4.3 but for ECCO v4.

used here (Figures 4.3 and 4.4). The coloured circles in Figures 4.3 and 4.4 show the austral winter and austral summer mean latitude and depth of each Θ/S bin within the respective coloured boxes. The size of each circle indicates the relative total volume of each water mass. Within both CARS and ECCO v4, AAIW, LCDW and AABW shoal from north to south. During the winter AAWW overlies mCDW, LCDW and AABW, and lies horizontally adjacent to mAAIW and AAIW. The upwelling LCDW reaches the surface, on average, between 65°S and 55°S while the downwelling AAIW forms at the surface between 60 °S and 50°S, extending further south during the summer following the southward retreat of AAWW and mAAIW. AAIW then sinks to approximately 1000m by 30°S.

A certain degree of seasonality exists within each of the major water masses in CARS (Figure 4.5) and ECCO v4 (Figure 4.6). AAWW varies most with maximum volume during the winter and minimum volume during the summer, and is well defined in both CARS and ECCO v4. There are notable differences between CARS and ECCO v4 in the seasonality of AAIW and mCDW. According to ECCO v4 the volume of mCDW is highest in April/May and lowest during September/November, which is opposite to the seasonal cycle of mCDW in CARS. In CARS the volume of AAIW is greatest during the winter, with a minimum during the summer. In comparison, the seasonality of AAIW in ECCO v4 is more complicated, with a distinctive peak in volume during both the summer and a minimum during the spring. During some years, 2000-2002 for example, there is an additional smaller peak during the winter. However, if the volume for just the

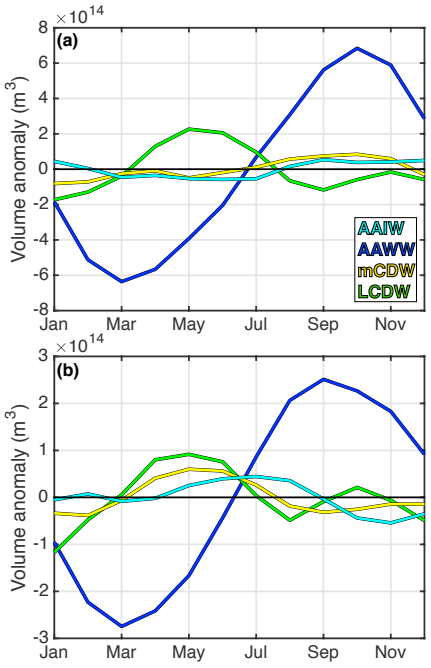

Figure 4.5: (a) Seasonal time-series of total volume $m^3/°C/(g/kg)$) from CARS for AAIW (cyan curve), AAWW (blue curve), mCDW (yellow curve) and LCDW (green curve). Calculated from the entire Southern Ocean south of 30°S. (b) As in (a) but for the Atlantic sector (Drake Passage to South Africa) of the Southern Ocean only.

Atlantic sector of the Southern Ocean is plotted the seasonality of AAIW and mCDW in CARS agrees more favourably with that in ECCO v4 (Figures 4.5b and 4.6b).

Important contrasts also exist in the seasonal distribution of AAWW, mCDW, AAIW and mAAIW in Θ/S space (Figures 4.7 and 4.8). In Figures 4.7 and 4.8 we show the volumetric distribution in ECCO v4 from late summer (April), through the austral winter (June, August and November) and into the austral spring and summer (December and February). These plots use a computationally more expensive small $\Delta\Theta$ and ΔS, better emphasising the changes in the structure of the volume. This selection of months are chosen to best highlight the observed seasonal cycle in the volumetric distribution, best viewed as an animation accessible at www.dropbox.com/s/2fx8xhd7m2ybeke/ecco_Vol.mov?dl=0. The black arrows in Figure 4.7 represent the vector $\mathbf{E} = (E_S, E_\Theta)$, the diathermal and diahaline transformations inferred from the air–sea heat and freshwater fluxes in ECCO v4, averaged for the months preceding each month shown. The black arrows in Figure 4.8 represent the vector $\mathbf{F} = (F_S, F_\Theta)$, the diathermal and diahaline transformations inferred from the volume change due to mixing in ECCO v4, averaged for the months preceding each month shown. A surface cooling beginning in April redistributes water, converting AAIW into AAWW. By June this forms a variety of AAWW centred at $S = 34.25$, just above the freezing point of sea water. This AAWW is made saltier

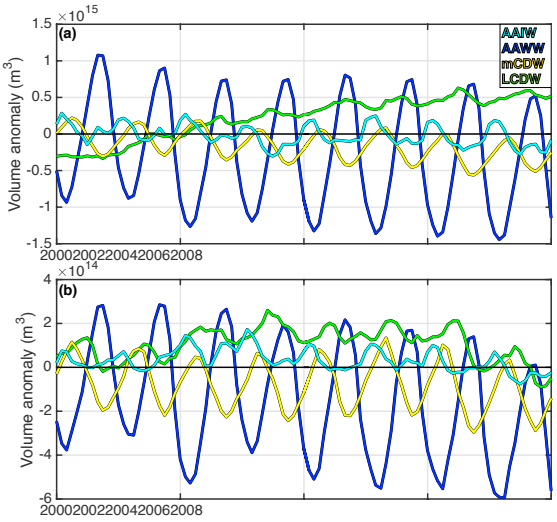

Figure 4.6: As in Figure 4.5 but for ECCO v4 and showing years 2000 to 2008

between June and November due to sea-ice formation and resultant brine rejection, increasing its salinity to ∼34.4. At the same time there is a cooling and freshening of water along the ridge of high volume which forms a straight line between the newly formed AAWW and LCDW (i.e. mCDW) in Figure 4.8. This suggests mixing occurs between AAWW and the underlying LCDW (see Figure 4.4) when the newly formed AAWW reaches a high enough salinity. During the spring and summer the AAWW is made warmer due to heat exchange with the atmosphere and fresher as sea-ice melts, eventually forming AAIW.

The volume fluxed between water masses can be assessed by summing the vectors crossing the isotherms that define the boundaries of each coloured box in Figures 4.7 and 4.8. In addition, this enables a comparison of the contribution to the total change ($\mathbf{G} = (G_S, G_\Theta)$) by advective changes ($M$) and dia-surface transformations due to air–sea exchange ($\mathbf{E} = (E_S, E_\Theta)$) and mixing ($\mathbf{F} = (F_S, F_\Theta)$). Figures 4.9 and 4.10 show the diathermal volume flux between AAIW–mAAIW, mCDW–AAWW and LCDW–mCDW in both CARS and ECCO v4. The advective component due to transport changes through 30°S are shown for ECCO v4 only. A positive dia-thermal transformation means water is warming. In the dia-surface transformation of water between AAIW and mAAIW, air–sea fluxes play a predominant role, while mixing apparently compensates slightly the air–sea fluxes. Air–sea fluxes drive a warming, and therefore formation of AAIW during the summer, while a relatively smaller cooling during the winter transforms AAIW in to mAAIW. During most of the year northward transport of AAIW at 30°S in ECCO v4 implies a weaker advective cooling indicative of the export of warmer water. This apparent cooling is strongest during the winter, while during the summer the transport induces a weaker adiabatic warming. The dia-surface transformation of water between LCDW, mCDW and AAWW is set predominantly by mixing, as

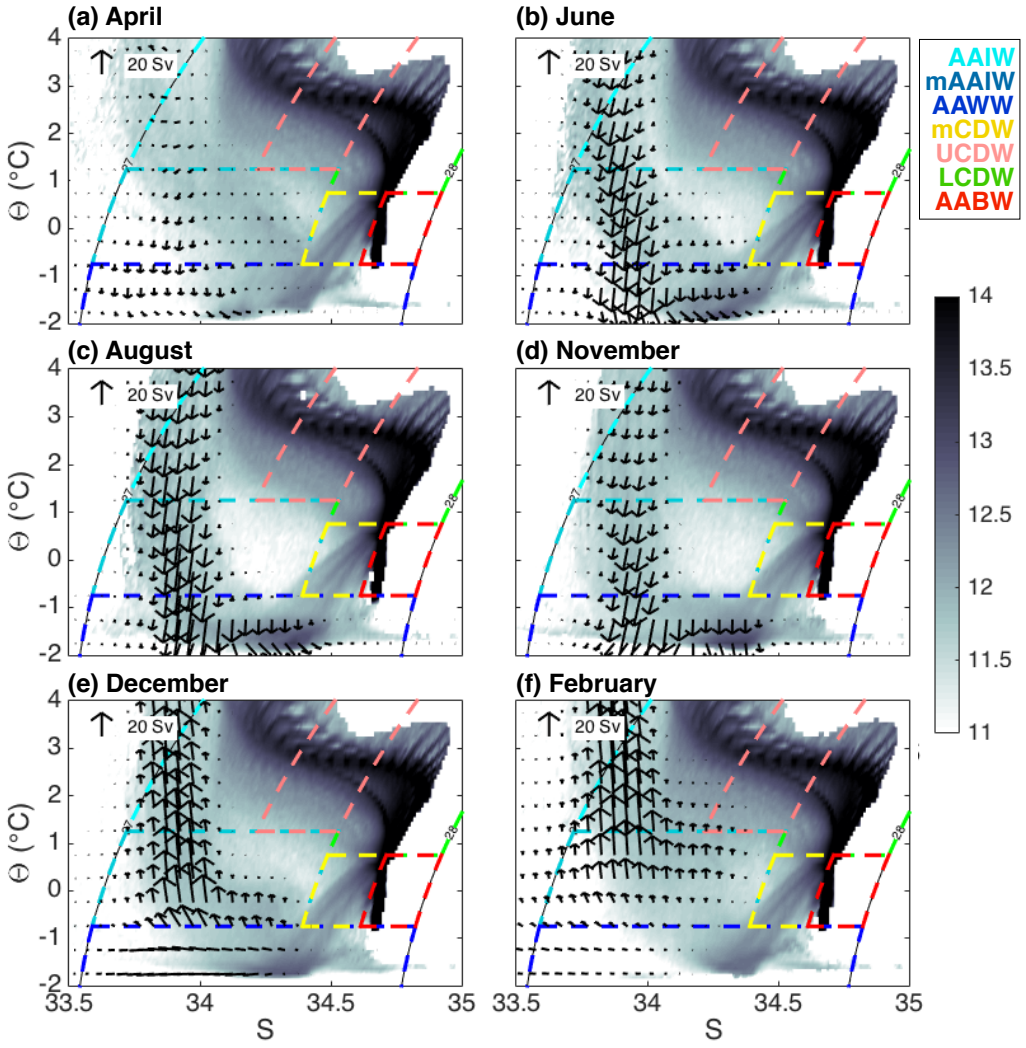

Figure 4.7: (a-f) Monthly-mean (1992-2012) of $\log_{10}$ water mass volume (in $m^3/°C/(g/kg)$) using ECCO v4 south of 30°S. Black contours show density anomaly referenced to 0 dbar (σ_0). Coloured boxes represent the nominal definition of each water mass used for this study, enclosed by isotherms and isopycnals. The black arrows represent the vector $\mathbf{E} = (E_S, E_\Theta)$, the transfromations inferred from the air–sea buoyancy fluxes in ECCO v4, averaged for the months preceding each month shown (units Sv)

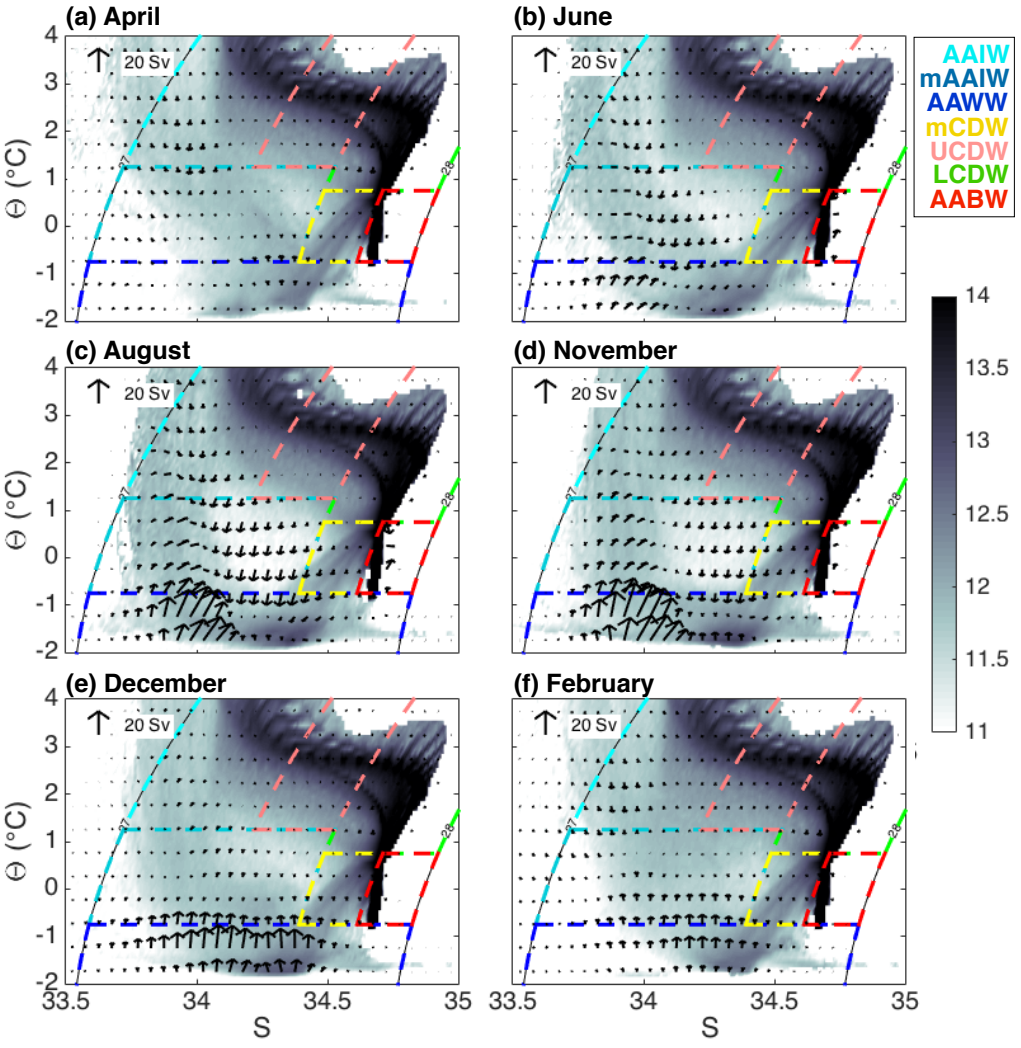

Figure 4.8: (a-f) Monthly-mean (1992-2012) of $\log_{10}$ water mass volume (in $m^3/°C/(g/kg)$) using ECCO v4 south of 30°S. Black contours show density anomaly referenced to 0 dbar (σ_0). Coloured boxes represent the nominal definition of each water mass used for this study, enclosed by isotherms and isopycnals. The black arrows represent the vector $\mathbf{F} = (F_S, F_\Theta)$, the dia-surface transformations inferred from the volume change due to mixing between each time step in ECCO v4, averaged for the month preceding each month shown (units Sv)

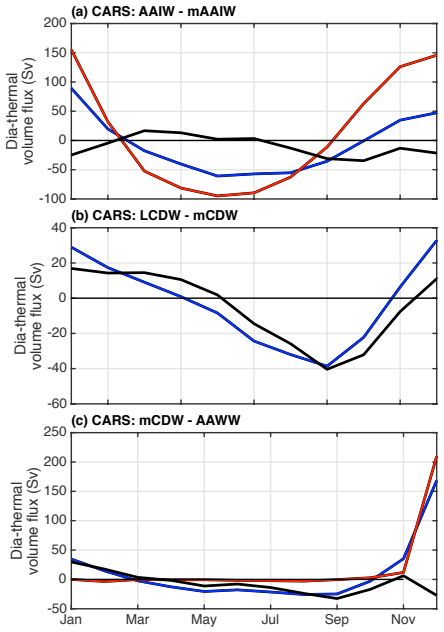

Figure 4.9: Seasonal time-series of total diathermal transformations from CARS volume change (G_Θ; blue curves), air–sea fluxes (E_Θ; red curves) and mixing (F_Θ; black curves) across the boundary between: (a) AAIW/mAAIW, (b) LCDW/mCDW and (c) mCDW/AAWW. Units: Sv.

the exchange between these water masses occurs below the sea surface (see Figure 4.4). The dia-surface transformation of LCDW into AAWW through mCDW occurs during the austral winter, with a maximum cooling of mCDW into AAWW preceding that of LCDW into mCDW by one to two months. The southward transport of LCDW at 30°S in ECCO v4 imposes a relatively consistent advective warming, with a slight maximum during the winter.

Analysis of the variability of water mass volume in the Southern Ocean therefore suggests that LCDW is upwelled and diabatically transformed into AAIW during the course of a year. During the winter we show that newly formed AAWW overlies LCDW. Diabatic upwelling of this LCDW through mixing occurs when AAWW reaches a critical maximum salinity due to sea-ice formation and brine rejection. In Θ/S space, this mixing occurs along a ridge of volume that forms a straight line between LCDW and AAWW, which we have labeled mCDW. During the summer this newly formed AAWW, partly composed of the upwelled LCDW, is transformed into AAIW through a warming and a freshening by air–sea heat exchange and melting sea-ice. Wind-driven upwelling replenishes the LCDW layer throughout the year, while the newly formed AAIW is predominantly exported during the winter. The following section will explore the physical mechanism responsible for the mixing between LCDW and AAWW, showing that this mixing is set by cabbeling.

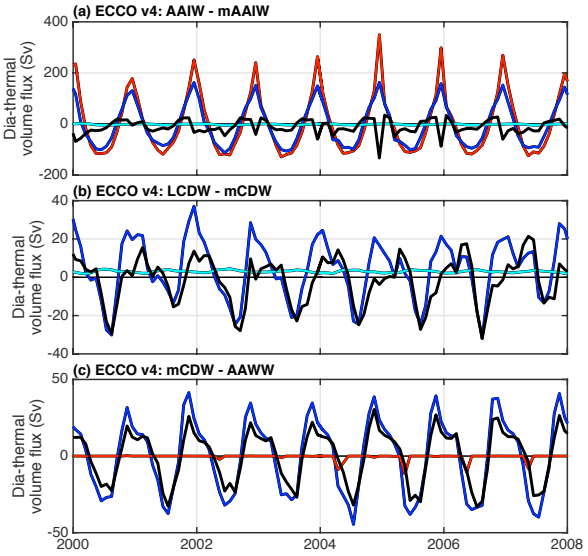

Figure 4.10: As in 4.9 but for ECCO v4 and showing years 2000 to 2008. Additionally showing adiabatic volume flux implied by the transport through 30°S (M_Θ; cyan curve).

4.5 Wintertime dia-surface transformation of LCDW into AAWW

This section discusses the physical processes governing the diathermal and diahaline transformation of LCDW into AAWW. The results presented in section 4.4 suggest that mixing plays an important role, and is strongest during the winter when AAWW reaches a maximum critical salinity. The process that drives this mixing can be assessed by understanding the relative stability of the water column to gravitational and cabbeling instabilities. Cabbeling is a consequence of the nonlinearity of the equation of state for seawater, in which two parcels of water with the same density but differing Θ and S (e.g. warm/salty against cold/fresh) will mix to create a water of a higher density (McDougall, 1987). More specifically cabbeling arises because the thermal expansion coefficient (α) and the haline contraction coefficient (β) vary with Θ and S resulting in the curvature of isopycnals in Θ/S space. This is shown schematically in Figure 4.11. Fofonoff (1957) and Foster and Carmack (1976) emphasise the importance of cabbeling for formation of AABW in the Weddell Sea at values of Θ and S similar to those discussed here.

Foster and Carmack (1976) discussed the stability of a water column in which a layer of cold/fresh AAWW sits above a layer of warmer and slightly saltier Warm Deep Water (equivalent to LCDW defined here). They point out that such a water column is weakly stratified, but unstable to cabbeling when AAWW is made saltier than a critical S. In Θ/S space this cut-off is defined at the S where a tangent to the isopycnal defined at the Θ, S and pressure of the Warm Deep Water intersects the Θ of AAWW (i.e. near

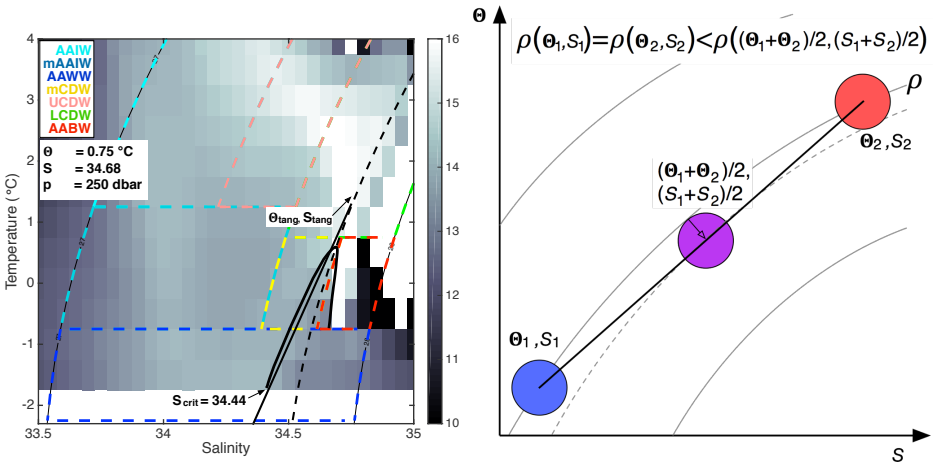

Figure 4.11: (left) As in Figure 4.2 but the the dashed black contour represents an isopycnal at a Θ, S and pressure (p) similar to that used in Foster and Carmack (1976), referred to here as Θ_{tang}, S_{tang} and p_{tang}. The solid black line is the tangent to this isopycnal at Θ_{tang} and S_{tang}. The critical S (S_{crit}) where this tangent the temperature at the freezing point of seawater. Any AAWW that is denser (higher than S_{crit}) than the solid black tangent, but less dense than the density represented by the dashed black isopycnal will unstable to cabbeling. The solid black curve shows a representative Θ/S profile. (right) Schematic representation of cabbeling, showing the mixing of two water masses (red and blue circles) of the same density (ρ) represented by the grey curve, but differing Θ/S. The two water masses mix along the black mixing line to form a new water mass (purple circle). This water mass has the average Θ/S of the original water masses, but due to the curvature of isopycnal surfaces in Θ/S space, the density (grey dashed curve) of the new water mass is greater than the original density, ρ.

the freezing point of seawater). According to Foster and Carmack (1976) AAWW that is saltier and denser than this tangent but less dense than the isopycnal defined at the Θ, S and pressure of the Warm Deep Water will be unstable to cabbeling. Mixing due to this cabbeling instability will continue until the mixture of the two layers lies along the tangent. If the Θ/S profile of the water column follows more closely the isopycnal defined at the Θ, S and pressure of the Warm Deep Water, it is more likely that vertical convection due to a gravitational instability is setting the properties of the water column. The slope of this tangent therefore represents the minimum vertical density gradient, along which the mixture of two vertically adjacent parcels of water is not denser than the deepest parcel. The slope of this tangent is therefore set by the Θ, S and pressure of the LCDW.

A tangent at a similar Θ and S is drawn in Figure 4.11 and shows that to a first approximation the ridge of high volume between LCDW and AAWW lies to the left of this tangent. Due to the fact that this does not lie along the black dashed isopycnal, this suggests that the process responsible for mixing between LCDW and AAWW may be cabbeling rather than gravitational instability. To show that cabbeling instability

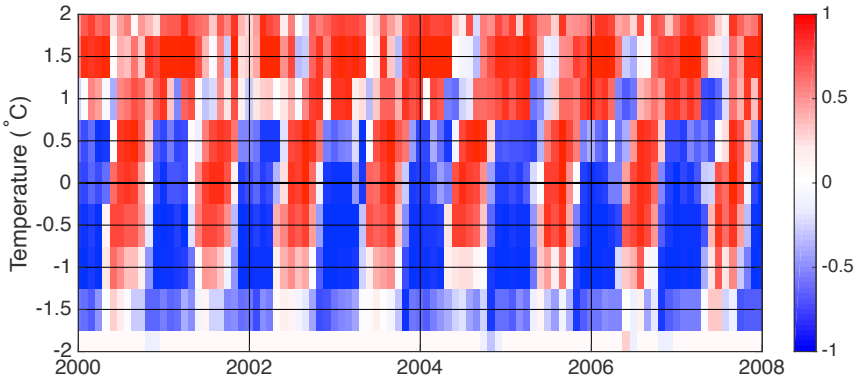

Figure 4.12: From ECCO v4; time-series representing the fraction of the vector $\mathbf{F} = (F_S, F_\Theta)$ projected onto the tangent shown in Figure 4.11. When this value is 1, $\mathbf{F}$ lies parallel to the tangent in the direction of a dia-surface transformation from LCDW to AAWW (i.e. cooling and freshening).

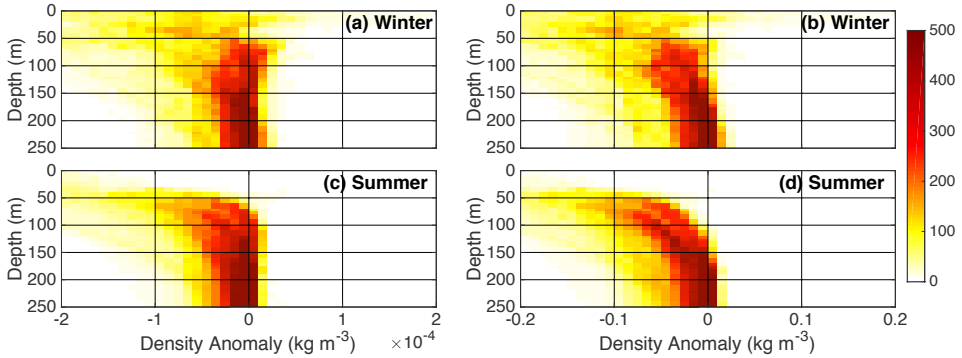

Figure 4.13: (left) The number of profiles in bins of depth and density anomaly averaged for (a) September and (c) December, January and February using CARS. Density anomaly was calculated for each profile by subtracting the density of LCDW referenced to the pressure of LCDW form the vertical profile of density calculated using the α and β referenced to the Θ, S and pressure of LCDW. (right) The number of profiles in bins of depth and density anomaly averaged for (b) September and (d) December, January and February using CARS. Density anomaly was calculated for each profile by subtracting the density of LCDW referenced to the pressure of LCDW form the vertical profile of density referenced to the pressure of LCDW.

is important for the upwelling of LCDW, in the remainder of this section we will show that the mixing discussed above and in section 4.4 seems to occur parallel to the black tangent in Figure 4.11. We will further demonstrate that in general density profiles in both CARS and ECCO v4 lie to the lighter side of the tangent and rarely reach the density defined by the dashed black isopycnal.

Calculating the fraction of the vectors $\mathbf{F} = (F_S, F_\Theta)$ (representing the diathermal and diahaline transformations due to mixing from ECCO v4) that project onto the tangent in Figure 4.11 shows that during the winter, mixing drives dia-surface transformation

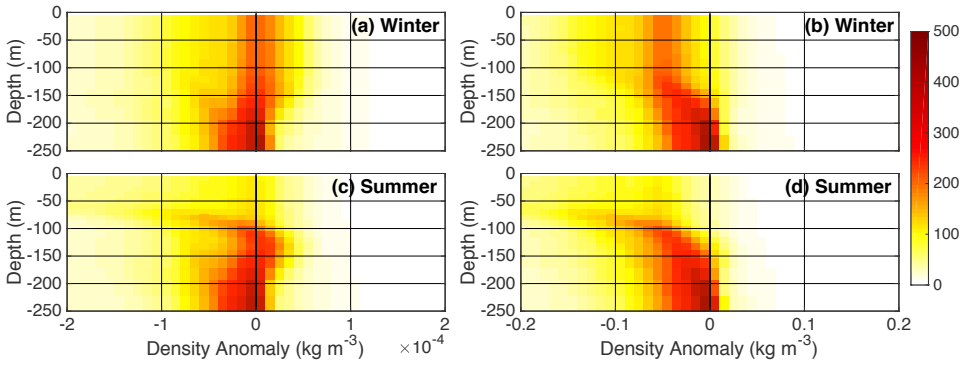

Figure 4.14: (left) The number of profiles in bins of depth and density anomaly averaged for (a) July, August and September and (c) December, January and February using ECCO v4. Density anomaly was calculated for each profile by subtracting the density of LCDW referenced to the pressure of LCDW form the vertical profile of density calculated using the α and β referenced to the Θ, S and pressure of LCDW. (right) The number of profiles in bins of depth and density anomaly averaged for (a) July, August and September and (c) December, January and February using ECCO v4. Density anomaly was calculated for each profile by subtracting the density of LCDW referenced to the pressure of LCDW from the vertical profile of density referenced to the pressure of LCDW.

parallel to the tangent (Figure 4.12). A fraction of 1 in Figure 4.12 during the winter indicates a cooling and freshening, and therefore a dia-surface transformation of water from LCDW into AAWW. During the winter, a fraction of -1 at the coldest AAWW, indicates the convergence water mass volume within the AAWW box.

To further demonstrate that the mixing between LCDW and AAWW is set by cabbeling, vertical profiles of density referenced to p_{tang} are compared to the density of the lightest LCDW (i.e. at Θ_{tang}, S_{tang} and p_{tang} in Figure 4.11). If the density of AAWW reaches the density of LCDW, this would be indicative of mixing due to a gravitational instability. Figures 4.13 and 4.14 instead suggest that the density anomaly in the surface 250m is consistently negative both during the summer, when AAWW is much warmer, fresher and less voluminous, and more importantly during the winter, when mixing between LCDW and AAWW is shown to be highest. Alternatively, if a linear profile of density (effectively representing the tangent in Figure 4.11) is defined using the α and β at the Θ_{tang}, S_{tang} and p_{tang}, the equivalent density anomaly in the surface 250m appears to be consistently near zero during the winter. The distribution of profiles in Figures 4.13 and 4.14 therefore indicate that during the winter months AAWW lies along or to the less dense side of the tangent in Figure 4.11. Any AAWW that becomes saltier and (therefore denser) than S_{crit} is unstable to cabbeling and induces mixing between AAWW and LCDW. This mixing will erode the top of the LCDW layer until all the water in the upper AAWW layer is lighter than LCDW and lies along the tangent in Figure 4.11, representing a linear combination of LCDW and AAWW.

4.6 Summary and conclusions

The conventional theory of the Southern Ocean overturning is based on the balance between the action of winds that steepen isopycnal gradients and the role of eddies in flattening these isopycnal gradients. The resultant residual mean overturning circulation drives an upwelling of CDW south of the Polar Front and a downwelling of AAIW and Subantarctic Mode Water north of the polar front (Marshall and Radko, 2003). The diabatic conversion of CDW into AAIW or AABW is thought to depend on the location in which CDW is upwelled relative to the sign of the time-mean air–ice–sea buoyancy flux (Speer et al., 2000; Marshall and Speer, 2012). Observations suggest that AAIW is typically formed in the Indian and South Pacific Oceans through a wintertime deepening of the mixed layer from the densest classes of Subantarctic Mode Water (Talley, 2013).

Using a novel framework, this chapter shows that the diabatic conversion of LCDW into AAIW relies on seasonal variations of surface buoyancy forcing and sub-surface mixing in the Atlantic sector of the Southern Ocean. This presents an alternative pathway for this diabatic conversion in which LCDW is first cooled and freshened during the winter as it mixes with overlying AAWW in a process governed by cabbeling. Summertime warming and freshening of this AAWW/LCDW mixture consequently forms AAIW. These processes are represented schematically in Figure 4.15. Seasonal variations in the total volume of AAIW suggests that formation occurs both during the summer through the processes outlined here, and during the winter in the Indian and South Pacific Oceans.

To understand changes in Θ and S, this framework relates variations in the volume of water within Θ/S classes to the diathermal and diahaline transformation of water across isotherms and isohalines by air–ice–sea buoyancy fluxes and mixing. Volume changes due to variations in transport can also be included, if a given Θ/S class extends beyond the boundary of the domain in question.

Data from an observationally based seasonal climatology (CARS) is compared to the output of an ocean state estimate (ECCO v4). Data from the Southern Ocean south of 30°S are projected into thermohaline coordinates as a volumetric distribution. Both the mean volume and the seasonal variations in each dataset agree well. Seasonally, AAWW varies most, with a maximum during the winter and minimum during the summer. In ECCO v4, AAIW volume peaks during both the summer and winter. This seasonality is not as strong in CARS, and is most apparent in the Atlantic sector of the Southern Ocean. The seasonal variability of LCDW is less clear, particularly in ECCO v4. In both datasets, a ridge of high volume connects LCDW to AAWW. The volume of water along this ridge also varies seasonally with a maximum during the summer and a minimum during the winter.

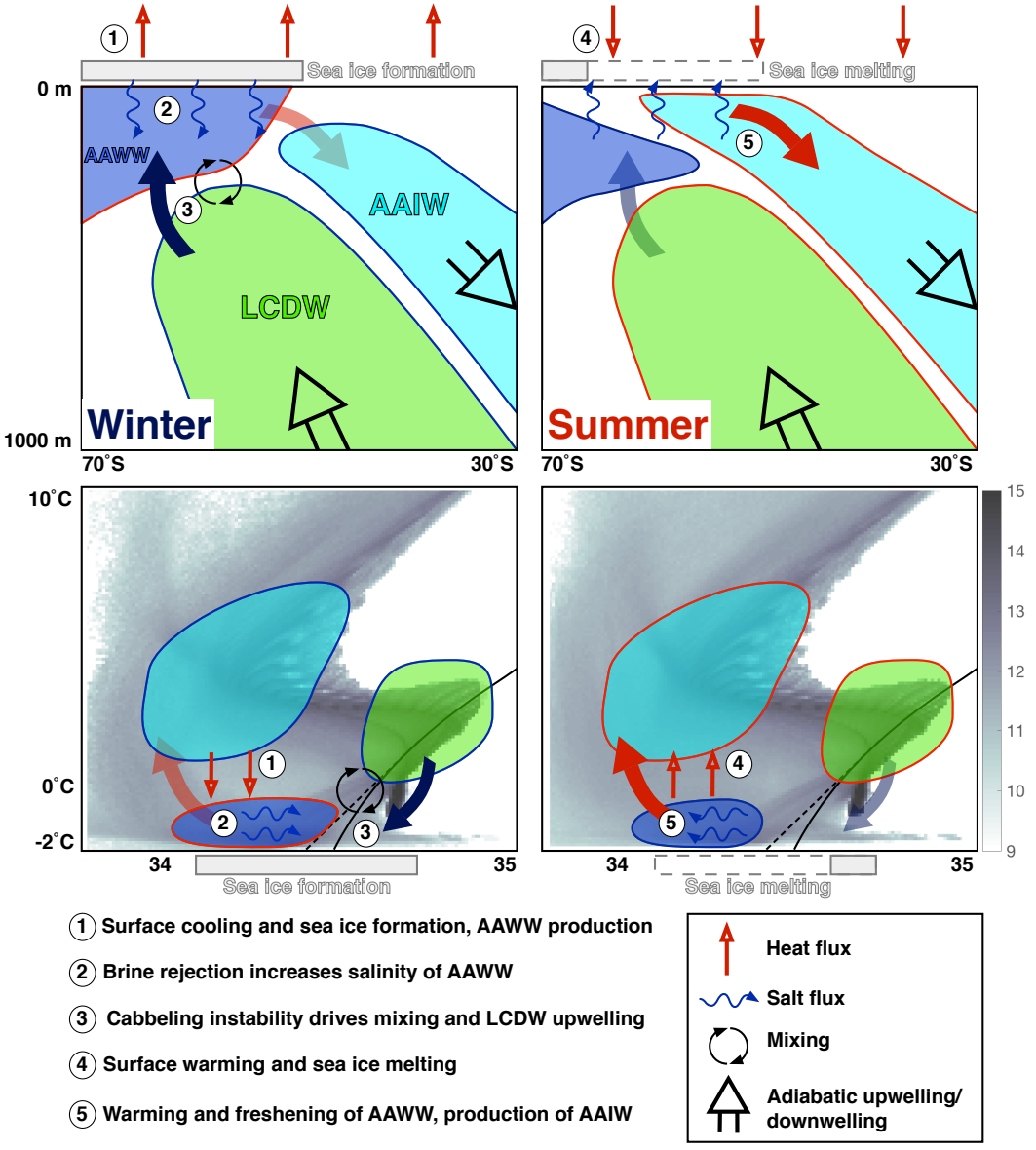

Figure 4.15: Schematic representation of the diabatic conversion of LCDW into AAIW through AAWW, over the course of a season in the Atlantic sector of the Southern Ocean. This presents an alternative pathway for AAIW formation in addition to the pathways that drive formation in the South Pacific and Indian Oceans. Each water mass is represented by the coloured blobs, where a red (blue) outline indicates an increasing (decreasing) volume. The top row presents the changes in geographical coordinates and the bottom shows the same changes in temperature and salinity coordinates.

These volume changes are related to the dia-surface transformation of water between each water mass due to air–ice–sea fluxes and sub-surface mixing. The contribution by air–sea fluxes is determined using atmospheric reanalysis products, and output from ECCO v4 which also includes a sea-ice component. Wintertime surface cooling forms AAWW at the expense of existing surface water and AAIW. When AAWW reaches the freezing point of seawater, brine rejection due to sea-ice formation increases its salinity,

at which point LCDW is then cooled and freshened as it mixes with this overlying AAWW. This explains the presence and variability of the volume connecting LCDW to AAWW. Surface warming during the summer and freshening via sea-ice melt forms AAIW from this mixture of newly formed AAWW and upwelled LCDW. During the winter AAIW is also formed as the densest variety of the Subantarctic mode waters, explaining the a peak in AAIW volume during both the summer and winter. In a similar analysis seasonal water mass variability along Drake Passage, Evans et al. (2014) showed that AAIW typically formed during the winter only. This may suggest that formation of AAIW during the summer may occur downstream of Drake Passage in the Atlantic sector of the Southern Ocean.

The upwelling of LCDW by sub-surface mixing only occurs when AAWW reaches a critical salinity. At this point the water column is weakly stratified but is unstable to cabbeling when this AAWW becomes saltier than this critical salinity. The resultant mixture of this AAWW and any water along the ridge connecting LCDW to AAWW will be denser than the water below it due to cabbeling. This would induce convection that would drive mixing between AAWW and the top of the LCDW layer until the resultant mixture is lighter than the underlying LCDW, while its Θ/S properties form the ridge connecting LCDW and AAWW. We speculatively suggest that the upwelling of LCDW by sub-surface mixing appears to predominately occur in the Atlantic sector of the Southern Ocean.

This analysis therefore shows that seasonal variations in air–ice–sea buoyancy, and their impact on sub-surface mixing, play a key role in the diabatic closure of the MOC in the Southern Ocean. The upwelling of LCDW through sub-surface mixing is set by cabbeling, arising from the non-linearity of the equation of state for seawater. These findings may improve our ability to estimate the strength of the Southern Ocean MOC, and may lead to better predictions for the fate of the Southern Ocean MOC in a warming climate.

Chapter 5

Argo Profile Based North Atlantic Water Mass Volume Climatology

Abstract

The thermohaline volumetric distribution is most easily calculated using gridded fields for temperature and salinity. Observing oceanic changes in thermohaline coordinates as variations in the volumetric distribution naturally isolates diabatic variability, which is un-aliased by the heaving associated by wind and eddies. These diabatic changes can be easily separated into those associated with the surface buoyancy forcing and mixing. This exploratory chapter discusses an alternative approach that calculates the volumetric distribution directly from profiles of temperature and salinity. The volumetric distribution is calculated using Argo profiles and synthetic profiles that sample the grid of an ocean model. These are compared to the distribution calculated using a gridded Argo product and the fully gridded fields from the same ocean model. This shows that the time-mean, seasonal-mean and temporal variability of the volumetric distribution can be correctly calculated directly from profiles. The comparison to the distribution estimated using the gridded Argo product suggests that interpolating data onto a regular grid appears to artificially mix water masses. Finally, further development into a publicly available dataset is discussed.

5.1 Introduction

Estimating oceanic variability using water mass coordinates is a well established and powerful approach (Walin, 1982). Recent studies typically apply such water mass frameworks using a single tracer. That is, they define a volume of water within a surface of constant temperature (Maze et al., 2009; Forget et al., 2011), salinity (Zika et al., 2015) or density (Badin et al., 2013; Cerovečki et al., 2013) and relate changes in that volume to the transformation of water across the tracer surface by air–sea buoyancy fluxes and mixing. By following tracer surfaces this framework naturally removes the adiabatic effects of vertical and horizontal heave that mask diabatic changes when observing the ocean from a fixed geographical framework (i.e. pressure surfaces).

Defining a water mass using two tracers improves upon the conventional use of the water mass framework by reducing the chance of ambiguously defining several separate water masses within one tracer class. Using temperature and salinity in particular enables more geographical information to be discerned from a distribution of volume, as the temperature and salinity of water masses are set by very geographically distinct surface forcing. This is highlighted for the subtropical North Atlantic within Figure 5.1. This shows the mean latitude and longitude for a given range of temperature and salinity classes based on the time-mean, three dimensional fields of temperature and salinity from a gridded Argo climatology. Figure 5.1 indicates that the warmest and saltiest water masses are located along the southern boundary of the domain, between 25°N and 45°N, while colder/fresher water is found to the north. The zonal distribution of water can also be discerned from this figure, with the saltiest water generally found to the east, while the freshest water is located to the west. One caveat of Figure 5.1 is that information regarding depth is lost.

Analyses of water masses in temperature and salinity (or thermohaline) coordinates typically seeks to understand the ways in which air–sea buoyancy fluxes and mixing maintain the time-mean state of the ocean (Speer, 1993; Döös et al., 2012; Zika et al., 2012; Groeskamp et al., 2014; Hieronymus et al., 2014). This thesis has explored the temporal variability of water mass volume in thermohaline coordinates, and the role air–sea buoyancy fluxes and mixing play in driving this variability. This exploratory chapter seeks to understand the ways in which this variability is affected by the methods used to project data into thermohaline coordinates as a volumetric distribution. The ultimate aim would be to produce a water mass volume climatology that can be publicly disseminated. Two techniques for calculating a volumetric distribution in thermohaline coordinates are explored here. The first involves using a geographically gridded product of temperature and salinity. This encompasses gridded model data and optimally interpolated observations. The alternative technique uses profiles of temperature and salinity to estimate the volumetric distribution. Using and comparing observational profiles to profiles that sample the grid of a numerical model, akin to the way Argo floats sample the

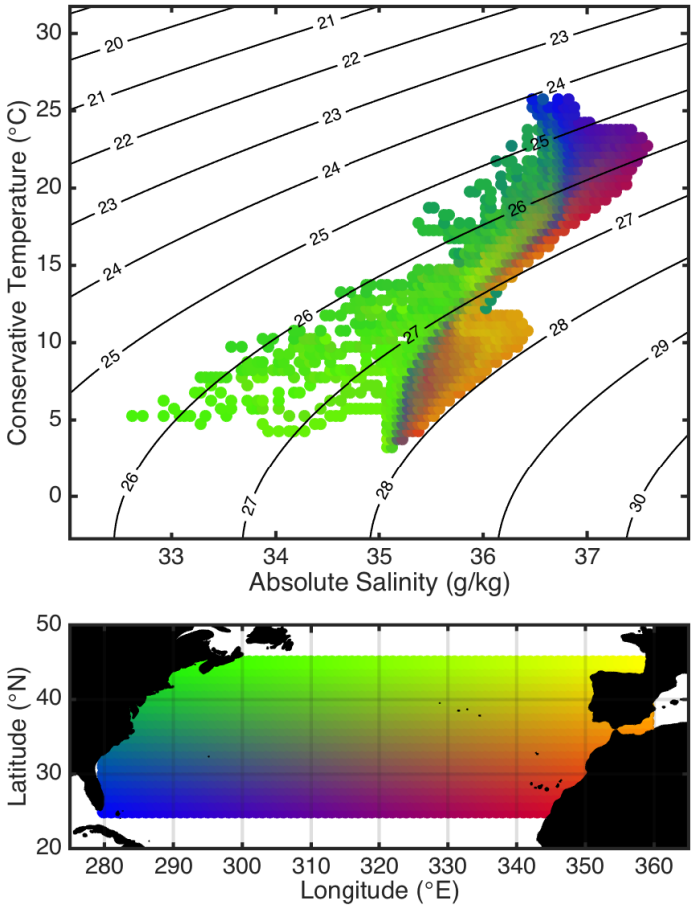

Figure 5.1: A scatter plot showing the mean latitude and longitude (colour) for a each of temperature and salinity class (circle) based on the time-mean, three dimensional fields of temperature and salinity from a gridded Argo climatology. With reference to the map of the subtropical North Atlantic, the mean longitude and latitude of a blue circle is 280°E and 25°N respectively.

real ocean, is a powerful tool for this type of analysis. For example, if the thermohaline volumetric distribution estimated from the model grid is the same as the distribution calculated from the profiles that sample the model grid, this suggests the profile only approach works. Further, if the estimated volumetric distribution from the observationally based gridded product differs from the observationally based profile estimate, this may highlight unwanted effects due to the interpolation scheme used to produce the geographically gridded product. Utilising Argo profiles in particular is appealing because of the large spatial coverage and relatively fast sampling period provided by Argo profiling floats. Argo profile data is also widely available in near real-time, so that any water mass volume climatology developed from this analysis could also be updated in near real-time.

The methods developed in this chapter use USGODAE Argo profiles to estimate the thermohaline volumetric distribution of water masses in the North Atlantic between 25°N and 45°N. We produce estimates for the mean thermohaline volumetric distribution, a seasonal cycle of this distribution and a complete time-series for the latter part of the Argo period. Using the methods developed in this chapter, profiles are separated into sub-regions, within which the mean thickness of temperature/salinity classes are estimated from each profile. These thicknesses are converted to a volume using the area of each sub-region. The total North Atlantic thermohaline volumetric distribution is therefore the sum of the thermohaline volume from each sub-region. We also use the Estimating the Circulation and Climate of the Ocean version 4 state estimate (ECCO v4; Forget et al., 2015) to compare the volumetric distribution determined using the geographically gridded model estimate to the volumetric distribution calculated using profiles, which sample the model grid at locations that match those of the Argo profiles used to constrain ECCO v4. By using ECCO v4 in this way, we can compare our profile estimate of the volumetric distribution to the well defined volumetric distribution determined using the gridded model output. These estimates are also compared to the volumetric distribution determined using the gridded Roemmich-Gilson Argo Climatology (Roemmich and Gilson, 2009). Throughout, those estimates determined using Argo profiles and profiles from ECCO v4 will be referred to as the 'Argo profile estimate' and 'ECCO v4 profile estimate'. Estimates determined using the gridded Roemmich-Gilson Argo Climatology and the full model grid from ECCO v4 will be referred to as the 'RGAC estimate' and the 'gridded ECCO v4 estimate'.

The next section will discuss in more detail the data and any pre-processing techniques used, while the following section will investigate the spatial and temporal distribution of Argo profile data in the subtropical North Atlantic. Sections 5.4, 5.5 and 5.6 will describe the methodology developed to calculate the volume of water masses in thermohaline coordinates using profile data and compare to the volume estimated using the gridded datasets. The discussion and conclusions will form the final section of this chapter.

5.2 Data sources and pre-processing

Profiles were accessed from the USGODAE Argo website as NetCDF files. Atlantic floats are selected from the profile index text file ar_index_global_prof.txt. From these files, the parameters labelled '_ADJUSTED' are selected and only data with a quality control (QC) flag of 1 are used (see Argo QC manual, reference table 2). Temperature and salinity data are converted to Conservative Temperature (Θ) and Absolute Salinity (S) using the TEOS-10 Gibbs-SeaWater oceanographic toolbox available at www.teos–10.org. After selecting profiles only from the subtropical North Atlantic, we remove data that falls outside the range -3<Θ<32 and 32<S<39. Further, we select profiles that occurred after 2004 at which point Argo achieved sufficient global coverage (Roemmich

and Gilson, 2009). Each profile is interpolated on to depth surfaces chosen to match the standard Argo depth intervals: 5 to 200m at 5m intervals, 220 to 400m at 20m intervals and 450 to 1950m at 50m intervals.

Data from the Estimating the Circulation and Climate of the Ocean version 4 (ECCO v4) state estimate (Forget et al., 2015) are accessed from www.ecco–group.org. We utilise fields for temperature and salinity (hereinafter we refer to the temperature and salinity from all data sources as Θ and S) and select data between 25°N and 45°N. The thermohaline volumetric distribution using the full model grid is determined monthly (between 1992-2012), by summing the volume of the model grid cells with a Θ and S that fall within a given Θ/S range (Evans et al., 2014). The time-mean and seasonal-mean estimates are determined by time-averaging the resultant time-series of the thermohaline volumetric distribution. The ECCO v4 profiles are available at www.ecco–group.org. The RGAC (Roemmich and Gilson, 2009) (monthly estimates, 2004-present) can be accessed at sio–argo.ucsd.edu/RG_Climatology. The thermohaline volumetric distribution is determined using the same method described for ECCO v4.

It is useful to briefly describe the methodology used to create the gridded fields in RGAC. The methodology is described in detail within Roemmich and Gilson (2009). Argo profiles for temperature and salinity are interpolated to a latitude, longitude and pressure at horizontal resolution of 1 degree and a vertical resolution of between 10 dbar at the surface and 100 dbar at 2000m. The first stage of this interpolation involves a first guess of the mean field for each month using weighted least-squares fit with linear and quadratic terms for longitude, latitude and pressure. These monthly mean fields are calculated using the 100 nearest Argo profiles, regardless of their distance. The monthly anomaly fields are then calculated from these monthly mean fields using objective analysis and by linearly interpolating the monthly mean field to the location of each individual Argo profile. Mapping errors arise from the small volume of data and the uncertainties in the statistics of the fields, and more complicated approaches do not reduce these errors.

5.3 Profile and data density

Following the pre-processing and quality control described above, a total of 26,270 profiles remain for this analysis. On a monthly-mean basis there are consistently high profile numbers (a mean of 2,195) with a very even spatial distribution, which is consistent throughout the year (Figure 5.2). The dashed grid in the two lower plots of Figure 5.2 are spaced at intervals of 4 degrees, and highlight that profiles generally occupy each of these $4° \times 4°$ sub-regions. In contrast to Figure 5.2, the number of profiles (per 30 day window) vary throughout the time period used here (2004-present; Figure 5.3), decreasing between 2004 and 2006, then increasing up to 2008 after which they gradually

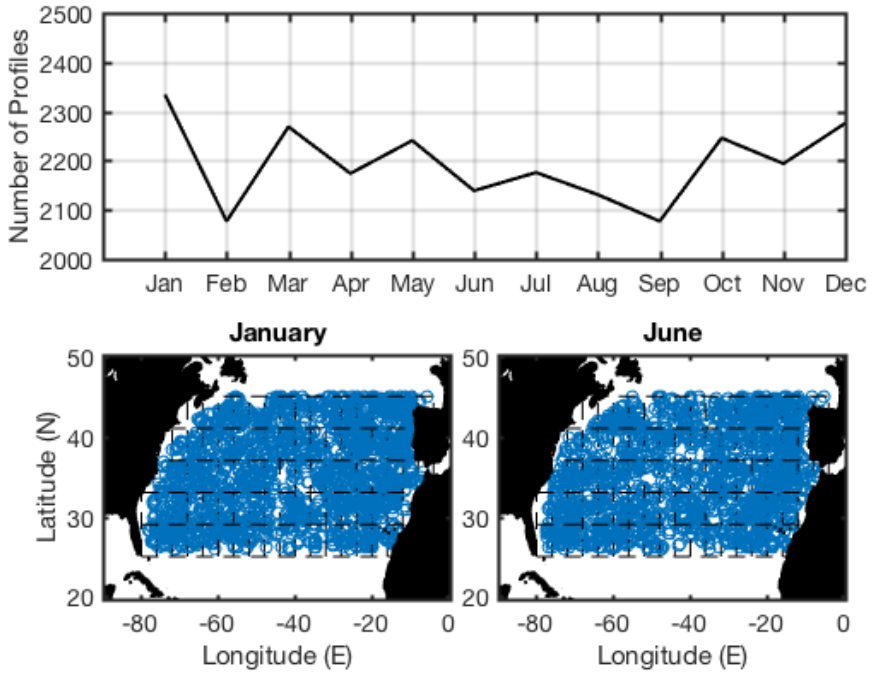

Figure 5.2: (top) Number of Argo profiles in monthly 30-day bins used for the seasonal estimates between 25°N and 45°N. (bottom) Spatial distribution of profiles in January and June.

decrease, giving a mean of 217 profiles per 30 day window. The spatial distribution of profiles also varies in time, with a generally more even distribution when profiles are more numerous, as highlighted for example by a comparison between January 2004 and June 2008 (Figure 5.3). Comparing the lower plots of Figure 5.3 and 5.2 there are number unsampled sub-regions in Figure 5.3. This highlights that the profile coverage presents the largest challenge when estimating a time-series of the thermohaline volumetric distribution. Within section 5.4 we discuss the sensitivity of the resultant thermohaline volumetric distribution to the sub-region size and temporal sampling window width.

Data density (number of Θ or S measurements per depth bin) also varies with depth both on a monthly-mean basis and with time (upper and lower plots Figure 5.4 respectively). Within the surface 1000m there are a monthly mean of ∼2100 data points available in each depth bin (upper plot Figure 5.4). This decreases to ∼1800 data points at 1200m and ∼1200 at 2000m. This distribution of data density is consistent throughout the mean seasonal cycle. Data density varies more dramatically in both depth and time over the entire time-series (lower plot Figure 5.4). At the surface data density matches the time-series shown in Figure 5.3. Earlier in the time-series (2004-2005) data density decreases more dramatically below 1000m compared to the latter part of the time-series (2007-2012). However, data density is relatively poor below 1700m and between 2005 and 2007 and after 2012.

5.4 Calculation of the time-mean thermohaline volumetric distribution

We determine the thermohaline volumetric distribution from Argo profiles by determining the mean thickness of a given Θ/S class within a defined sub-region. The total volume for that given Θ/S class is the sum for all sub-regions of the thickness multiplied by the sub-region area. The surface area (A) for each depth layer ($k = 1...z_k$) within each sub-region ($j = 1...[m \times n]$ where m = latitudinal distance/grid resolution and n = longitudinal distance/grid resolution) is calculated. For a depth layer in a region of the ocean where the depth of that layer is shallower than 1950m, a reduced surface area is calculated by determining a fractional surface area based on the ocean depth at each corner of the sub-region. The thickness (H) of each sub-region layer is also determined, centred at the depth of that layer. The time-mean volumetric distribution for a given sub-region ($\overline{V_j}$) using all available profiles is therefore:

$$\overline{V_j}(\Theta, S) = \sum_i \sum_k A(z_{jk}) H_{jk}\ \delta(\Theta - \Theta_{ik}, S - S_{ik})\ \frac{1}{D(z_{jk})}, \tag{5.1}$$

where D is the data density within the j-th sub-region and $i = 1...$number of profiles. The delta function is one when the Θ and S of the i-th profile is within the given Θ/S

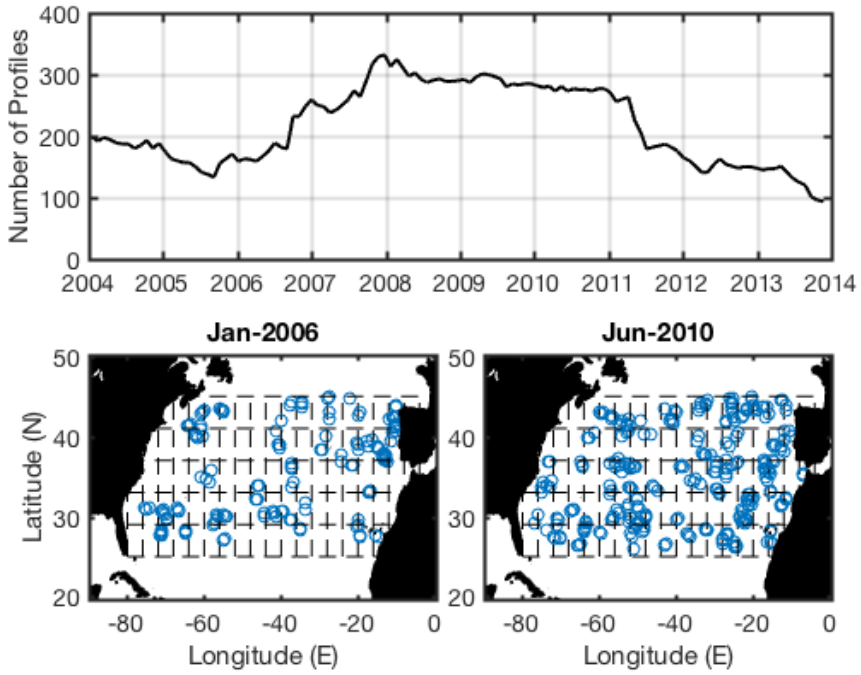

Figure 5.3: (top) Number of Argo profiles in 30-day bins between 25°N and 45°N. (bottom) Spatial distribution of profiles in January 2004 and June 2008.

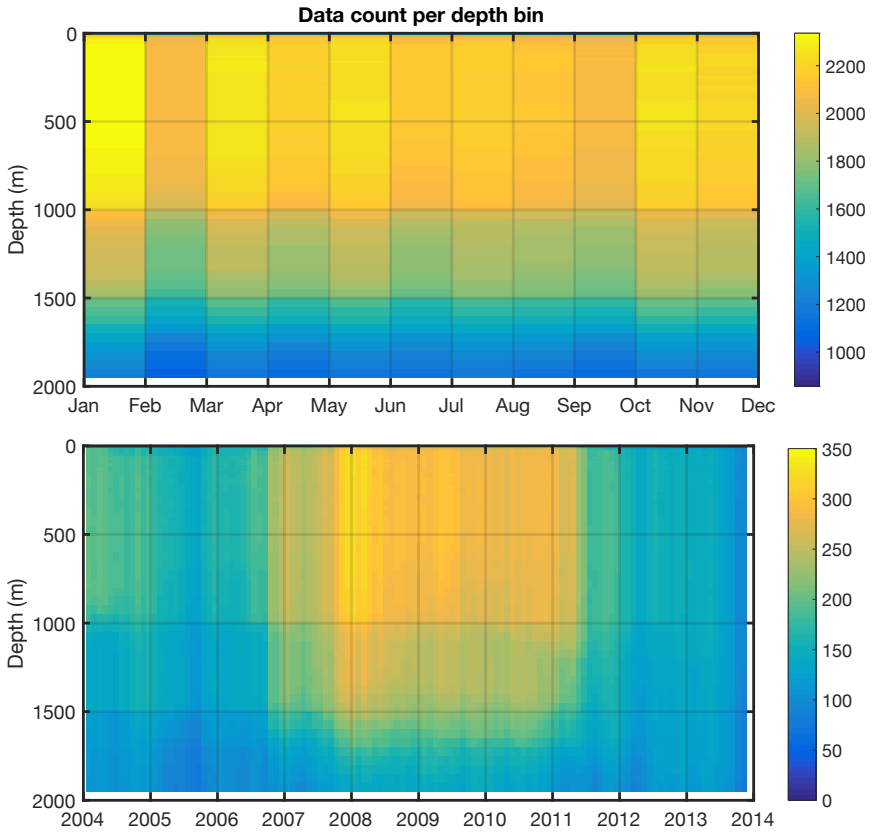

Figure 5.4: Number of data points within each depth bin between 25°N and 45°N for seasonal estimate and time-series estimate.

class, otherwise it is zero. The total time-mean thermohaline volumetric distribution ($\overline{V}$) is given as:

$$\overline{V}(\Theta, S) = \sum_j V_j(\Theta, S). \tag{5.2}$$

In determining $\overline{V}$, the first consideration that must made is the size of the sub-region from which $\overline{V_j}$ is calculated. To test the sensitivity of $\overline{V}$ to the sub-region size, sub-regions with a resolution of 2 and 4 degrees are compared for Argo and ECCO v4 profile estimates. These different resolution estimates of $\overline{V}$ from Argo profiles and ECCO v4 profiles are compared to the estimates from RGAC and ECCO v4 respectively (Figure 5.5-5.8). The shape of the distribution is captured well in both the Argo and ECCO v4 profile estimates, particularly within the main modes of water-mass volume where the volume is larger than 10^{13} $m^3/°C/(g/kg)$. Starting in the warmest and saltiest waters, these represent the surface waters of the subtropical gyre. At temperatures of approximately 18°C along the ridge of high volume is the subtropical mode water (STMW). Moving down the distribution, through central and intermediate waters, the most voluminous water is the North Atlantic deep water (NADW) at the coldest and

freshest point of the main distribution. Also captured is the Mediterranean overflow water indicated by a tongue of salty water at approximately 10°C. There is very little visual difference in $\overline{V}$ determined using 2 or 4 degree sub-regions (Figure 5.5 and Figure 5.7). The estimates using the gridded RGAC and ECCO v4 products have slightly more volume on the fresher side of the distribution, indicative of the surface waters, suggesting both profile estimates are not capturing the very surface water. The profile and gridded estimates are compared directly in Figures 5.6 and 5.8, which shows that with both 2 and 4 degree resolution sub-regions, there are differences between the estimates using Argo and ECCO v4, and subtle differences between the different sub-region resolutions.

The Argo profile estimate is generally larger in extreme regions of Θ/S space, for example, in the warm/salty STMW, the cold/fresh NADW and along the warmer/fresher flank of main volumetric mode. In all other regions of Θ/S space the RGAC estimate produces larger volumes. Importantly the total volume of both estimates is similar at $\sim 2.5 \times 10^{16}$ m^3. The key difference between the Argo profile estimate and the RGAC estimate is that the method used to calculate the Argo profile estimate captures all water masses sampled by each profile, with no smoothing. It is likely that some of this variability is reduced by the interpolation scheme used to create RGAC, so that volume is more concentrated within the more voluminous water masses. This notion is reflected in the structure of the difference between estimates in Θ/S space, as most of the volume in the RGAC estimate is focussed toward the centre of mass of the volumetric distribution in Θ/S space as if water masses have been artificially mixed compared to those determined using the Argo profile estimate.

Such differences should not be expected when comparing the ECCO v4 profile estimate and the gridded ECCO v4 estimate, as these profiles directly sample the ECCO v4 grid. Again both estimates capture a similar total volume, but there are slight differences in Figures 5.6 and 5.8, which suggest that in particular the profile estimate calculates more volume at $\Theta = 5$°C and in general slightly more total volume. Comparing the 2 and 4 degrees estimates, the sub-region size seems to reduce both the total difference and the difference at $\Theta = 5$°C. Given these differences are predominant in the deeper water masses, and reduce when sub-region size is reduced, this indicates that the difference between ECCO v4 profile and gridded estimates may be the result of the way the profile estimate accounts for topography when estimating the volume of the deepest sub-region layers. It may also be a consequence of the relatively poor data coverage at depths of greater than 1500m (e.g. see Figure 5.3). The difference between the ECCO v4 profile and gridded estimates are small elsewhere in Θ/S space and are likely due to a slight inhomogeneity in the temporal and spatial distribution of profiles.

In summary, sub-region size used to calculate V_j, seems to affect the volume of the deeper water masses due to the way topography is accounted for when estimating the volume of the deepest sub-region layers. Poor data coverage at depths greater than 1500m may also affect the estimated volume of the deeper water masses. Larger sub-regions over

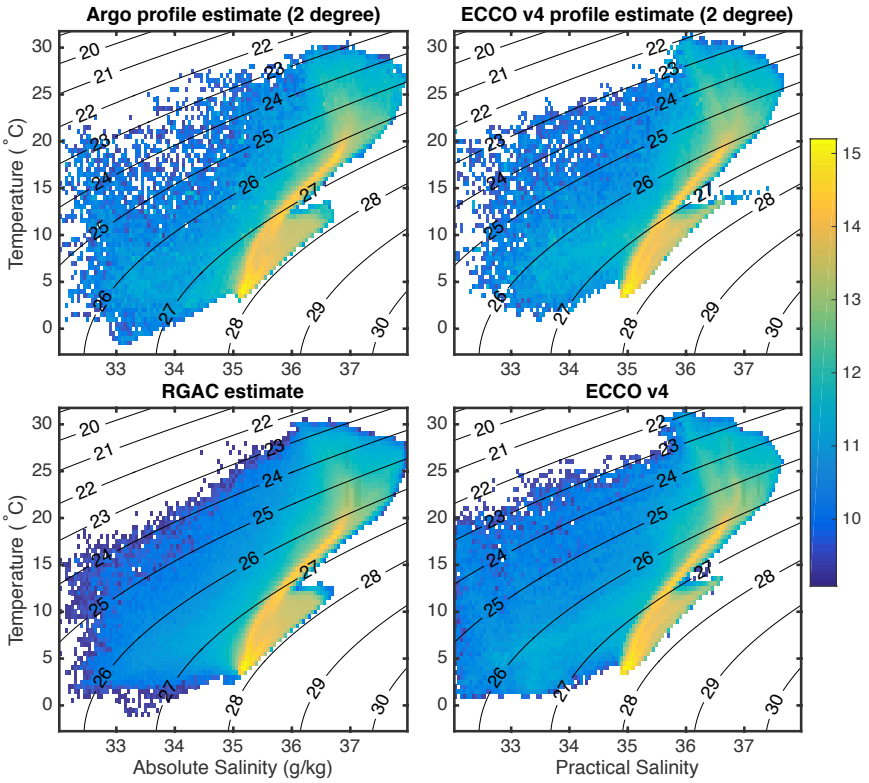

Figure 5.5: Logarithm of the thermohaline volumetric distribution as estimated by Argo profiles (top left), RGAC (bottom left), ECCO v4 profiles (top right) and ECCO v4 (bottom right). Profile estimates use 2 degree sub-regions between 25°N and 45°N. Volume has units of $m^3/°C/(g/kg)$.

estimate the volume of the deepest water masses. In general however, this method does seem to correctly estimate the time-mean $\overline{V}$, suggested by the comparison between the ECCO v4 profile estimate and the ECCO estimate. Discrepancies between the Argo profile estimate and the RGAC estimate indicate some fundamental differences in the distribution of water-masses determined using each method, which may be indicative of the interpolation scheme used to create the RGAC. The next section will describe how the above method is extended to calculate a seasonal cycle in the volumetric distribution.

5.5 Calculation of the seasonal mean thermohaline volumetric distribution

The seasonal mean thermohaline volumetric distribution is determined by adding a time dependency (t=year-day) to equations (5.1) and (5.2):

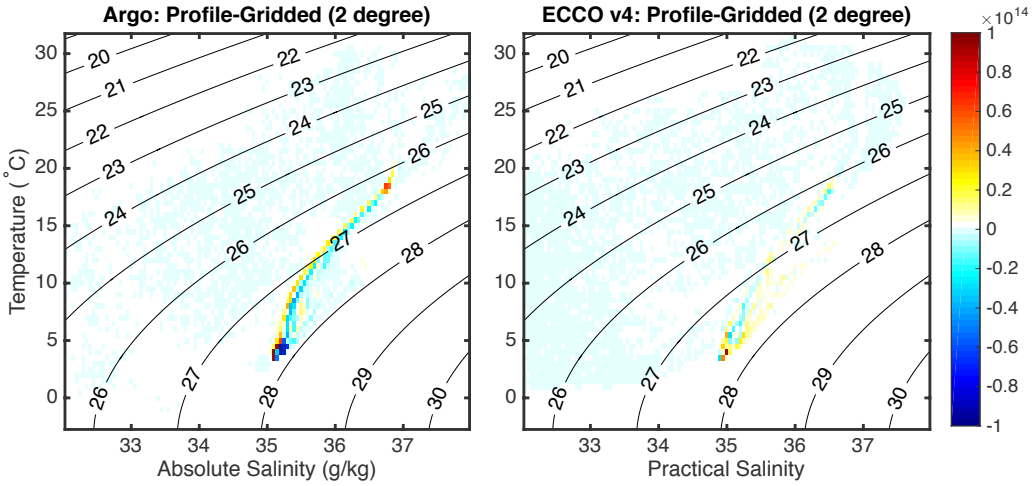

Figure 5.6: Difference between the thermohaline volumetric distribution estimated from Argo profiles and RGAC, and ECCO v4 profiles and ECCO v4. Profile estimates use 2 degree sub-regions between 25°N and 45°N. Units: $m^3/°C/(g/kg)$.

$$V_j(t,\Theta,S) = \sum_i \sum_k A(z_{jk}) H_{jk}\ \delta(t - t_{ik}, \Theta - \Theta_{ik}, S - S_{ik})\ \frac{1}{D(z_{jk},t)}.n \tag{5.3}$$

The delta function is now one when the sampling date (t_{ik}) falls within a defined year-day range, and the Θ and S of the i-th profile is within the given Θ/S class. Data density (D) is re-defined within both a given year-day range and the j-th sub-region. Again i = 1...number of profiles. The total seasonal mean thermohaline volumetric distribution (V) at values of t between 1 to 366 is given as:

$$V(t,\Theta,S) = \sum_j V_j(t,\Theta,S). \tag{5.4}$$

A seasonal cycle of V can then be created at a temporal resolution that best suits the data availability. Shown in Figure 5.2 is the availability of profiles within monthly-bins of 30 days. In general these ∼2200 profiles per 30-day bin have an even spatial distribution. Increasing this resolution to for example 10 days, reduces the number of profiles to ∼700, with some regions of sparse data (not shown).

To display the seasonal cycle of V, the volume is summed across all values of S and plotted against Θ with $\overline{V}$ removed. The seasonal cycle is determined using the Argo and ECCO v4 profile estimates, with sub-regions of 2 and 4 degrees (Figures 5.9 and 5.10). These estimates are compared to the RGAC estimate and the ECCO v4 estimate (Figure 5.11 and 5.12). Both the Argo and ECCO v4 profile estimates show good agreement with the seasonal cycle of volumetric distribution calculated using the gridded products. The agreement is best at values of Θ where there is a strong seasonal cycle, particularly

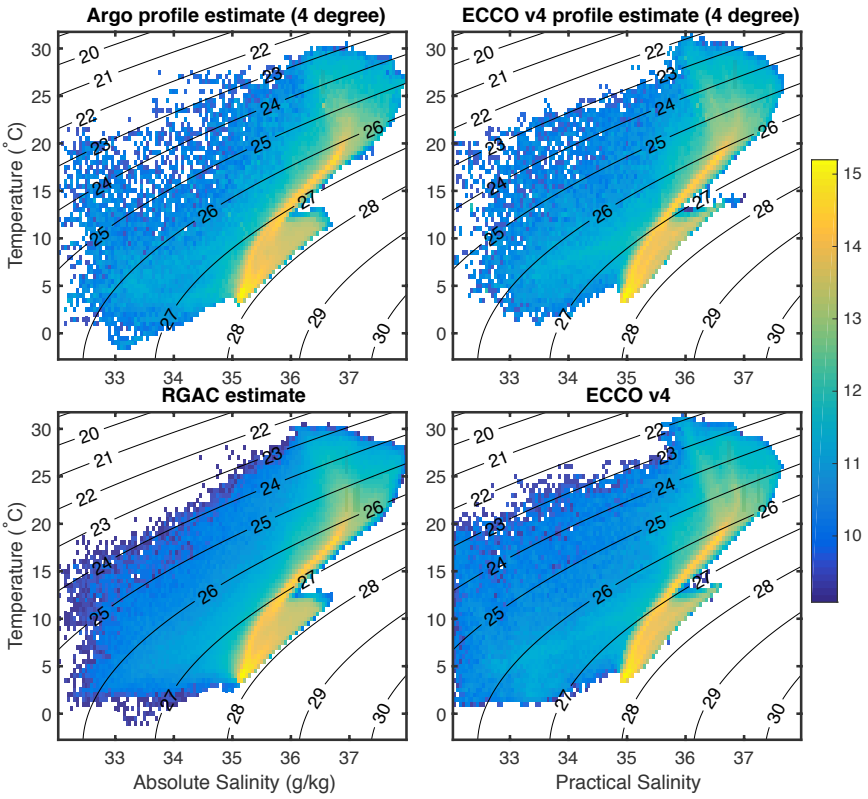

Figure 5.7: As in figure 5.5 but using 4 degree sub-region resolution.

at Θ>15°C. Here, volume at Θ>20°C is lowest during the winter and highest during the summer, which contrasts an opposing seasonal cycle between 15°C and 20°C. This reflects a seasonal exchange of water between the surface mixed layer and the Θ/S classes representing mode waters. The agreement is less strong at Θ<15°C particularly in the Argo profile estimate where the ratio of signal to noise is high. The choice of sub-region size affects the Argo profile estimate more significantly, with reduced noise at Θ<15°C.

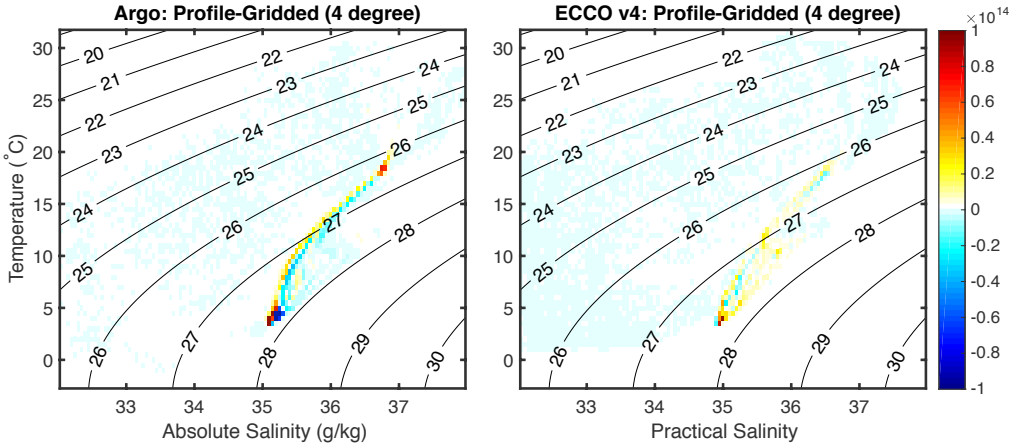

Figure 5.8: As in figure 5.6 but using 4 degree sub-region resolution.

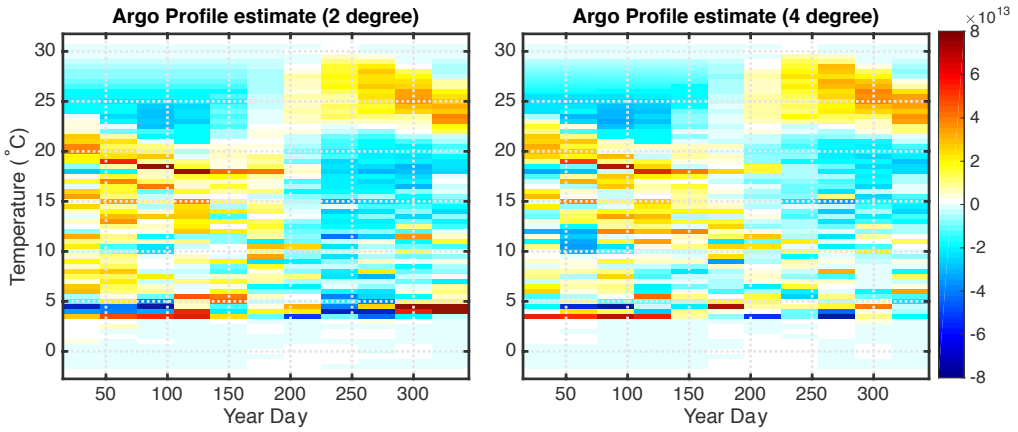

Figure 5.9: Seasonal cycle of the thermohaline volumetric distribution estimated using Argo profiles in 2 (left) and 4 (right) degree sub-regions using a 30-day sampling window, between 25°N and 45°N. The volume at each time-step is summed across all values of S and plotted against Θ with $\overline{V}$. Units: $m^3/°C$.

Therefore, it seems that the seasonal cycle of V in the surface and mode waters is captured well by the Argo and ECCO v4 profile estimates using both 2 and 4 degree sub-regions. Profile estimates from both Argo and ECCO v4 are both noisier at Θ<15°C in comparison to the gridded estimates. This noise is reduced when the sub-region size is increased, which suggests that the reduced number of profiles used to estimate the seasonal cycle using sub-regions with 2 degree resolution affects the deeper water masses. This begins to indicate that a careful balance needs to be struck between the effects of the chosen sub-region resolution and the number of available profiles. The next section expands upon this approach to create a time-series of the volumetric distribution using an idealised seasonal cycle calculated using the estimates in this section.

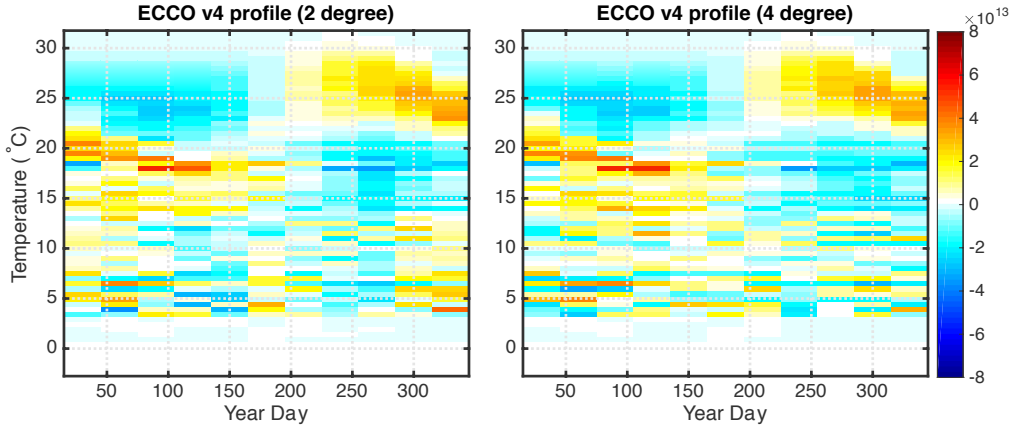

Figure 5.10: As in Figure 5.9 but using ECCO v4 profiles.

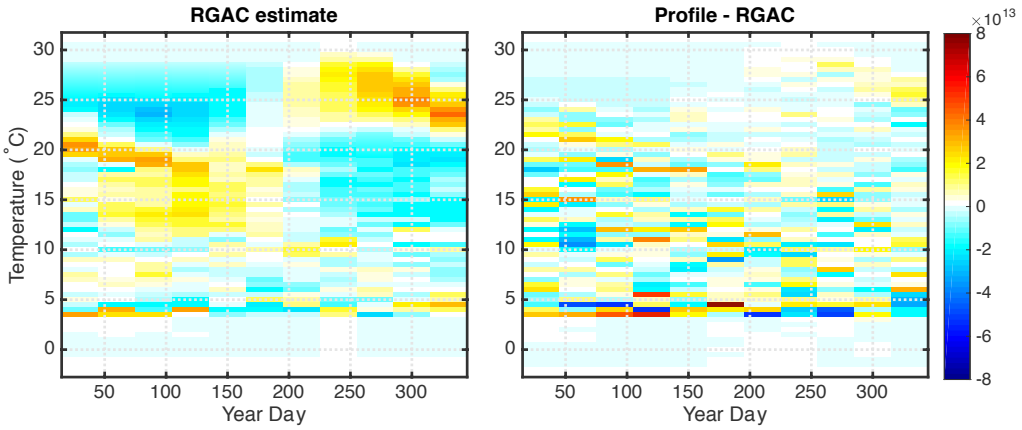

Figure 5.11: (left) Seasonal cycle of the thermohaline volumetric distribution estimated using RGAC. The volume at each time-step is summed across all values of S and plotted against Θ with mean volume removed. (right) Difference between the volume calculated using Argo profiles and RGAC. Profile estimate uses 4 deg sub-regions and a 30-day sampling window, between 25°N and 45°N. Units: $m^3/°C$.

5.6 Estimating the temporal variability of V

The ultimate goal of this analysis is to produce a time-series of V using Argo profiles alone. The challenge of doing so in comparison to estimating the time or seasonal mean of V is the poor data coverage at intervals of a month or less (e.g. Figure 5.3). For example, if a time-series of V is calculated using just the methods outlined above, but equation (5.3) is adjusted to select profiles that fall within 30-day intervals starting on January 2007, the resultant ECCO v4 profile estimate has large biases relative to the gridded ECCO v4 estimate (Figure 5.15). These errors occur when there are sub-regions without data coverage, as a consequence of a spatial bias in the distribution of profiles. This bias can be reduced by estimating the mean volumetric distribution within a given

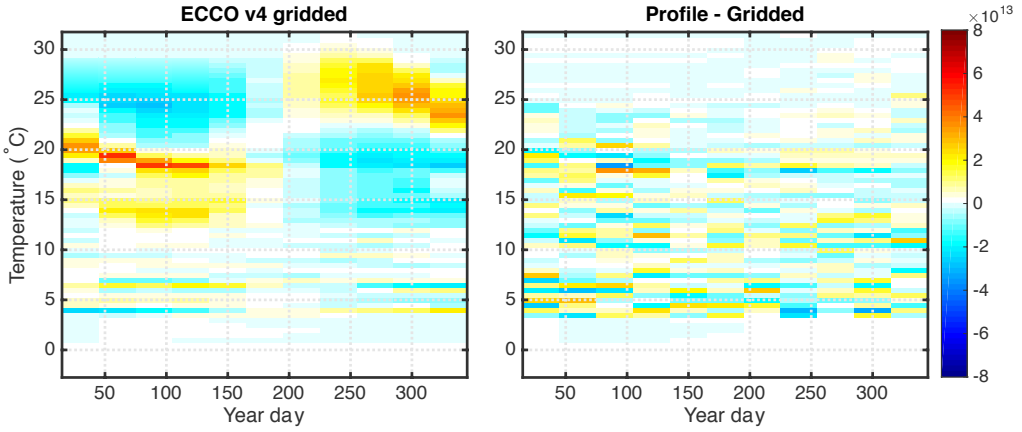

Figure 5.12: As in Figure 5.11 but using ECCO v4.

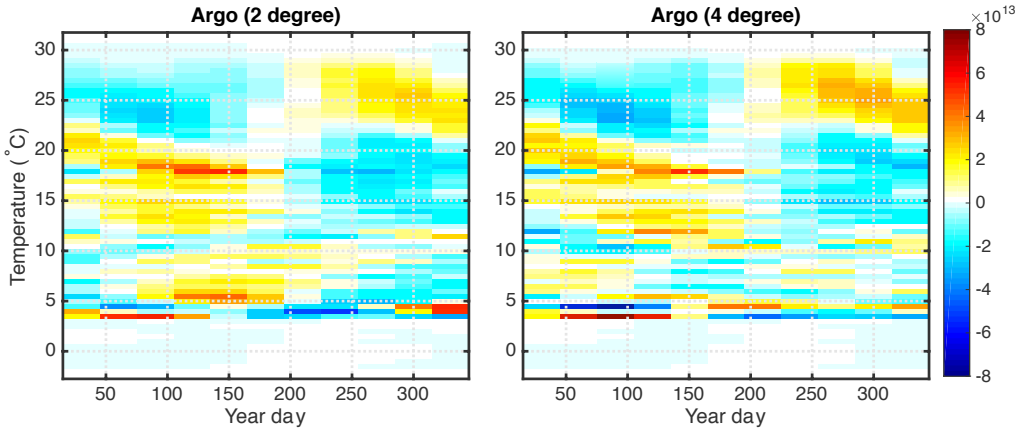

Figure 5.13: As in Figure 5.11 but displaying the idealised seasonal cycle calculated using equation (5.5).

sub-region at the relevant time of the year if there are no profiles. This can be achieved by calculating an idealised seasonal cycle for each Θ/S class within each sub-region.

Using the mean seasonal cycles shown in Figures 5.9 and 5.10 an idealised seasonal cycle can be constructed at each point in Θ/S space. This is achieved by determining the annual and semi-annual components of the seasonal cycle according to Argo or ECCO v4 in a method similar to that used by Ridgway et al. (2002):

$$V_S(t,\Theta,S) = \overline{V}(\Theta,S)+X_1(\Theta,S)\cos(t)+X_2(\Theta,S)\sin(t)+X_3(\Theta,S)\cos(2t)+X_4(\Theta,S)\sin(2t)+\epsilon. \tag{5.5}$$

Here the coefficients X_1 and X_2 are the cosine and sine of the annual cycle, X_3 and X_4 are the cosine and sine of the semiannual cycle and t is the year-day. The mean volume is given by $\overline{V}$. The coefficients are solved for using a matrix inversion to minimise ϵ in $X = bA^{-1} + \epsilon$, where X is the matrix of unknown coefficients in (5.5), b is the known volume anomaly of the seasonal cycle at Θ and S from equation (5.4), and A represents the sine and cosine terms in (5.5).

Shown in Figures 5.13 and 5.14 are the idealised seasonal cycles of V calculated using (5.5), from the Argo and ECCO v4 profile estimates. These are calculated based on the total volume from all sub-regions. These estimates compare well with the seasonal cycle in Figures 5.9 and 5.10, as well as reduce the effects of noise at Θ<15°C. This good agreement suggests that these idealised seasonal estimates are suitable for estimating the V when data coverage is poor.

A time-series of V is therefore estimated at 30-day intervals using both Argo and ECCO v4 profiles, by calculating the sum of all V_j from each sub-region when there is a minimum of two profiles. Increasing the minimum threshold to a larger number of profiles introduces variability not replicated by the gridded estimates. When the number of

profiles in a given sub-region falls below this threshold, V_j is calculated at the relevant year-day based on the idealised seasonal cycle within that sub-region (Figures 5.16 and 5.17) . Again V in Figures 5.16 and 5.17 is summed across all values of S and plotted against Θ with $\overline{V}$ removed. The resultant time-series agree favourably with the gridded ECCO v4 and RGAC estimate, capturing much of the interannual variability at all values of Θ. There is still more noise at lower values of Θ, but the ratio of signal to noise is not too high to discern any variability. It is particularly promising that some of the variability within mode and central waters ($15 < \Theta < 18$) is resolved using the profile estimate. Interestingly, in a manner consistent with the comparison of the estimated $\overline{V}$, the range of variability calculated with the Argo profile estimate is larger than the RGAC time-series. This is particularly evident in the STMW between 2009 and 2011.

In summary, it is possible to successfully estimate a time-series of V using only vertical profiles of temperature and salinity. Noise in the the time-series of V is likely the result of poor data coverage and the consequential spatial inhomogeneity of profiles. Poor data coverage in the subtropical North Atlantic is a known problem (Roemmich and Gilson, 2009), so expanding the domain to encompass the whole North Atlantic for example, may produce an improved estimate using the profile only method.

5.7 Conclusions

This chapter describes the development of a novel method to project the temporal variability of water masses into thermohaline coordinates using only vertical profiles of temperature and salinity. Using this method the time-mean, seasonal mean and temporal variability of the thermohaline volumetric distribution is successfully estimated in the subtropical North Atlantic. This method calculates the thermohaline volumetric distribution by dividing the ocean horizontally into sub-regions and vertically into layers. The mean thickness of a given Θ/S class from all profiles within a given sub-region

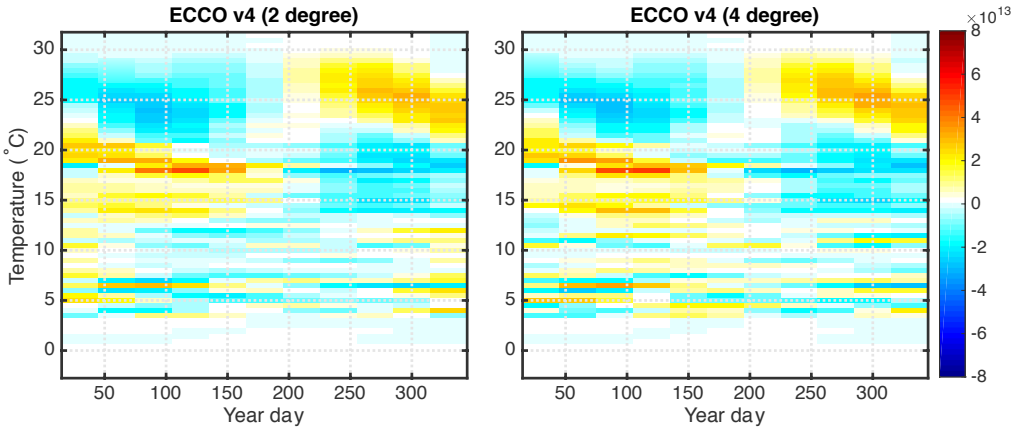

Figure 5.14: As in Figure 5.12 but displaying the idealised seasonal cycle calculated using equation (5.5).

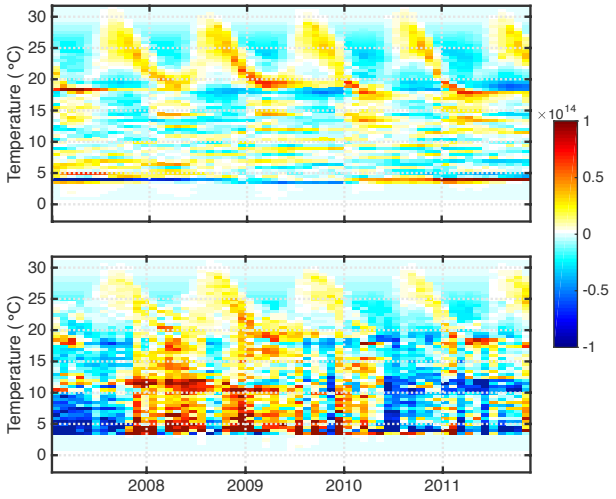

Figure 5.15: (top) Time-series of the thermohaline volumetric distribution calculated using the ECCO v4 grid between 25°N and 45°N. The volume at each time-step is summed across all values of S and plotted against Θ with the mean volume removed. (bottom) Time-series of the thermohaline volumetric distribution calculated from ECCO v4 profiles using 4 degree sub-regions and a 30-day sampling window, between 25°N and 45°N. Units: $m^3/°C$

is multiplied by the sub-region surface area at each layer, giving a mean volume for that sub-region. The volume from each sub-region is summed to give the total thermohaline volumetric distribution. The ability of the profile only method to estimate the thermohaline volumetric distribution is assessed by a comparison with the distribution estimated using gridded products of temperature and salinity. The volume is estimated using Argo

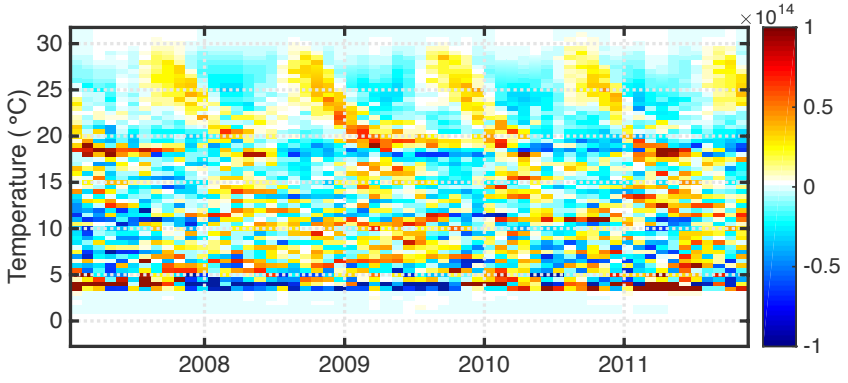

Figure 5.16: Time-series of the thermohaline volumetric distribution calculated from ECCO v4 profiles using 4 degree sub-regions and a 30-day sampling window, between 25°N and 45°N. The volume at each time-step is summed across all values of S and plotted against Θ with $\overline{V}$ removed. When there are fewer than two profiles within a given sub-region, the volumetric distribution is calculated for the given day using the idealised seasonal cycle for that sub-region. Units: $m^3/°C$

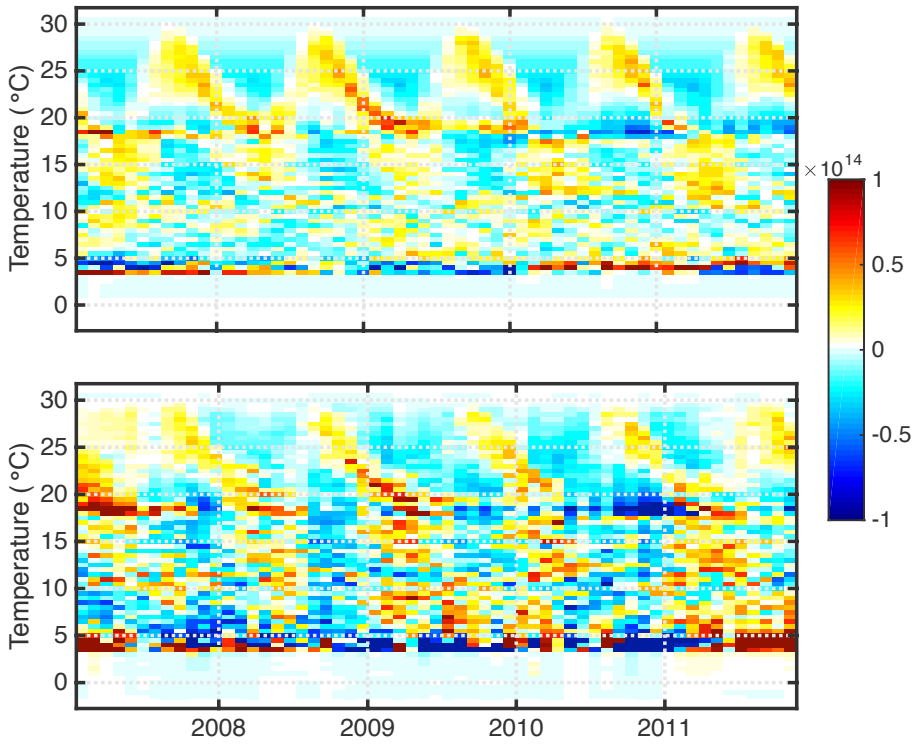

Figure 5.17: (top) Time-series of the thermohaline volumetric distribution calculated using RGAC between 25°N and 45°N. The volume at each time-step is summed across all values of S and plotted against Θ with the mean volume removed. (bottom) Time-series of the thermohaline volumetric distribution calculated from Argo profiles using 4 degree sub-regions and a 30-day sampling window, between 25°N and 45°N. When there are fewer than two profiles within a given sub-region, the volumetric distribution is calculated for the given day using the idealised seasonal cycle for that sub-region. Units: $m^3/°C$

profiles and artificial vertical profiles that sample the grid of ECCO v4. These estimates are then compared to the thermohaline volumetric distribution calculated using the full ECCO v4 grid and an optimally interpolated, gridded Argo climatology (RGAC).

These comparisons show that the profile only estimate is sensitive to the sub-region size. Larger sub-regions tend to overestimate the volume within the deeper water masses, which is likely a consequence of a larger grid spacing that misses topographic features that penetrate shallower than the maximum depth of Argo data. Also, both the Argo profiles and the artificial profiles from ECCO v4 have limited coverage at depths of greater than 1500m, also affecting the estimated volume of the deeper water masses. Reducing the sub-region size also affects the estimated thermohaline volumetric distribution using profiles, as the number of profiles per sub-region reduces when the sub-region size is reduced. This is particularly limiting when estimating the temporal variability

of volume, as profile numbers are lower within short temporal windows. Profile distribution is also not homogeneous, so that when estimating the temporal variability of the volumetric distribution there are often sub-regions with no profiles. To estimate the temporal variability of the volumetric distribution, the sub-regions with low profile numbers are supplemented by estimating the seasonal mean volumetric distribution for that sub-region, at the relevant time of year. Interestingly, using a minimum of two profiles per sub-region best estimates the temporal variability using this approach, with limited noise.

Of particular interest are the differences between the thermohaline volumetric distribution estimated using Argo profiles and the gridded RGAC. The time-mean volume according to the profile estimate is generally greater in the more extreme regions of Θ/S space such as in the warm/salty and cold/fresh regions. The volume towards the centre of the distribution is generally higher using RGAC. This change from the volume estimated using Argo profiles to volume estimated using RGAC is similar to the change that would be expected through mixing, which acts to narrow the distribution of volume within thermohaline coordinates. This difference is not apparent in the comparison from ECCO v4, therefore it would seem that the process of optimally interpolating observations onto a regular geographical grid narrows the distribution of water masses in thermohaline coordinates. This difference is also present in the temporal variability of the volumetric distribution, so that the range of variability estimated from the Argo profiles is wider than the variability estimated using RGAC. The coverage of Argo in the subtropical North Atlantic is known to be poor, and therefore the estimate may improve if the domain is extended to include the whole North Atlantic.

Further development is therefore required before the methods developed here can be used for types of analyses within this thesis. It is also likely that gridded observational products are suitable for estimating the temporal variability of the thermohaline volumetric distribution. To develop this method further and produce a climatology of the thermohaline volumetric distribution using only Argo profiles, this approach should be extended to each of the ocean basins. In doing so the sensitivity of the estimated volume to the number of profiles should be established by comparing volumes estimated with different numbers of profiles with varying spatial distributions. Finally, a platform for the public dissemination of the climatology could also be developed, which should also make available the software developed to produce the climatology.

Chapter 6

Conclusions

6.1 The challenges in understanding oceanic changes of temperature and salinity

This thesis has sought to understand the processes that drive variability in temperature and salinity in the ocean to aid our understanding of how the ocean is changing due to anthropogenic climate change. A methodology has been developed to isolate the diabatic changes of temperature and salinity from the adiabatic changes associated with the vertical and horizontal motion of water. These diabatic changes are those due to a direct addition or removal of heat/freshwater through air–sea buoyancy fluxes or via exchange by sub-surface mixing.

Measurements of temperature and salinity from a fixed hydrographic record are subject to adiabatic changes due to vertical and horizontal motions. Vertical heaving of surfaces of constant temperature, salinity or density result in changes in temperature and salinity at a fixed depth that are not the result of diabatic processes (Bindoff and McDougall, 1994). Changes in the transport of water also impose an adiabatic change on observations from a fixed geographical location (Pardaens et al., 2008). The main challenge in estimating oceanic change is accounting for these adiabatic processes in observations of temperature and salinity. It is also important to ensure that a climate signal or trend is not aliased by any poorly sampled variability from the wide range of temporal and spatial scales on which the ocean changes.

In this thesis a novel framework is utilised to understand the variability of temperature and salinity in the worlds oceans. This framework is based on the water mass framework presented by Walin (1982), extended to define ocean volumes in terms of both temperature and salinity. This framework is a quasi-Lagrangian approach that estimates changes between surfaces of constant temperature and salinity, naturally removing the associated effects of vertical and horizontal motions. Temperature and salinity are a natural

pair of tracers to use, for significant geographical information can be inferred from the temperature and salinity of a water mass, as these properties are set by geographically distinct surface forcing (e.g. see Figure 5.1).

Within each chapter, observational and ocean model data are projected into thermohaline coordinates as a volumetric distribution in temperature and salinity classes. The variability of this distribution is described in terms of the transformation of water across the isotherms and isohalines that define each temperature/salinity class. These transformations represent a diabatic change in the temperature or salinity of water due to air–sea fluxes of heat and freshwater, and mixing. The volume change within a particular region of the ocean due to transport changes into and out of the domain boundaries are also included in this budget. This framework is constructed so that unwanted adiabatic variability associated with the heave of isopycnal surfaces by eddies/Rossby waves or basin scale changes in wind-stress are naturally removed. The adiabatic variability resulting from the horizontal migration of isopycnal outcrops is also accounted for with this framework.

Recent work has focused on the mean state of the ocean in thermohaline coordinates, exploring the balance between air–sea buoyancy fluxes and mixing. The work in this thesis focuses on regions of the world's oceans where the seasonal and interannual variability of air–sea fluxes and mixing are closely linked to the variability of the overturning circulation. Over these spatial and temporal scales the variability of air–sea fluxes are relatively well known, allowing the related changes to the water mass distribution in thermohaline coordinates to be easily calculated. Changes in the volumetric distribution calculated from observational records and model output of temperature and salinity are compared to these variations due to air–sea fluxes to infer the intensity of sub-surface mixing. These studies highlight the suitability of the water mass framework for understanding complex oceanographic processes, enabling a better prediction of how anthropogenic climate change is affecting and will affect the momentum, heat and freshwater budgets of the ocean. The insight gained into the roles of mixing and transport throughout this thesis, will therefore improve estimates of the long-term changes in the exchange of heat and freshwater between the atmosphere and the ocean.

In the remainder of this chapter the findings of this thesis and their theoretical implications are discussed in the next section, while recommendations for future work are described in section 6.3. Finally, this chapter is concluded in section 6.4.

6.2 The findings of this thesis and their theoretical implications

This thesis has sought to understand how the seasonal and interannual variations in air–sea buoyancy fluxes and mixing interact with the overturning circulation of the ocean in

the absence of adiabatic heaving, to improve our understanding of the circulation itself. The focus of this study was therefore on regions of the ocean where the interplay of air–sea interaction and mixing processes is important in the closure of the global overturning circulation. Two such regions are the Southern Ocean and the subtropical North Atlantic. Doing so required the development of a novel framework that projects observations and model output of temperature and salinity into thermohaline coordinates as a volumetric distribution, and described in terms of the transformations across isothermal and isohaline surfaces. Throughout this thesis it is shown that this framework successfully removes the adiabatic effects associated with the vertical and horizontal motions of tracer surfaces, and allows a clearer understanding of the processes that are important in setting the seasonal and interannual variations of oceanic temperature and salinity. Using this framework this thesis has shown how the mean ocean circulation is governed by the climatological seasonal cycle, and emphasised the role of the wind in driving interannual changes in the overturning circulation.

In the subtropical North Atlantic this thesis focused on interannual variability. The objective was to use the water mass framework to understand the interaction between interannual variations in the Atlantic Meridional Overturning Circulation (AMOC) and the water mass distribution of the subtropical North Atlantic, and how these changes relate to the water mass changes caused by air–sea heat fluxes. The variability of volume above the thermocline and the heat content within that volume is closely linked to the transport across the boundaries of the subtropical North Atlantic. Air–sea heat fluxes only play a role in setting the interannual variations of the heat content in the upper ocean. This analysis also shows that the variability in volume of the upper subtropical ocean and therefore the transport divergence in the subtropical ocean are closely linked to the basin wide Ekman pumping. Thus, on interannual timescales the heat budget of the subtropical North Atlantic is set equally by transport and air–sea fluxes, and the transport variability is driven by integrated variations in the wind over the subtropical ocean.

In the Southern Ocean, it is generally thought that wind-driven upwelling brings circumpolar deep water (CDW) to the surface, which is transformed by zonally contrasting air–sea buoyancy fluxes to form dense Antarctic bottom water (AABW) to the south of the Antarctic circumpolar current (ACC), and lighter Antarctic intermediate water (AAIW) to the north of the ACC (Speer et al., 2000; Talley, 2013). AABW flows into the abyssal ocean down the Antarctic continental shelf, while AAIW is subducted into the interior ocean by wind-driven Ekman pumping (Marshall and Speer, 2012). Air–sea buoyancy fluxes across the ACC therefore play a crucial role in determining the properties of most of the oceans major water masses, and are an important mechanism for the closure of the global overturning circulation (Marshall and Speer, 2012)

However, most theoretical views of the Southern Ocean limb of the overturning circulation describe this diabatic transformation using time-mean air–sea fluxes of heat

and freshwater (e.g. Speer et al., 2000). Using a variety of observational data, complemented by model analysis, this thesis finds that seasonal variations in air–sea buoyancy fluxes are critical in the transformation of Southern Ocean water masses. Seasonal variations in the thermohaline distribution of water masses were initially investigated from a hydrographic transect across Drake Passage and an observationally based seasonal climatology. Using the water mass framework to remove the effects of eddy related heave, this highlighted the imprint of the Southern Ocean overturning on the seasonal inflation and deflation of Antarctic winter water (AAWW), AAIW and CDW. Air–sea buoyancy fluxes drive a wintertime cooling and formation of AAWW and AAIW from the underlying CDW and previously formed AAWW, thus deflating the CDW layer at a rate that exceeds the wind-driven inflow. Similarly the rate of AAIW formation exceeds the wind-driven export, increasing the thickness of the AAIW layer. In the summer, AAWW is eroded by surface warming while AAIW is exported. This enables an inflation of CDW during the summer.

An extension of this analysis to encompass the whole Southern Ocean revealed the importance of cabbeling in setting the diabatic transformation of CDW into AAIW. The volumetric distribution of water masses in the Southern Ocean was examined using an ocean state estimate and a seasonal climatology. The ocean state estimate, ECCO v4, is a modelling framework that simulates the evolving state of the ocean between 1992-2011. It is constrained to observations in a physically consistent manner using an adjoint model, and forced at the poles by a full sea ice model. Thus the model output represents the variability of the oceanic temperature and salinity in as physically realistic a manner as possible.

The analysis of the whole Southern Ocean revealed a seasonal pathway for the transformation of CDW into AAIW. It also highlights the importance of sea ice formation in determining the transformation of water between CDW and AAWW. Again wintertime surface cooling forms AAWW near the freezing temperature of seawater, but in addition this analysis shows that brine rejection due to sea ice formation salinifies this newly formed AAWW. The mixing between AAWW and CDW suggested by the study in Drake Passage only occurs when AAWW reaches a critical salinity. This salinity represents the maximum density at the freezing point of seawater, beyond which the water column (consisting of AAWW overlying CDW) becomes unstable to cabbeling. AAWW that is saltier than this critical salinity will, when mixed with the underlying water, form a water mass that is denser than the water surrounding it and sink. This mixing will therefore continue along a linear combination of temperatures and salinities connecting AAWW to the CDW, eroding the underlying CDW layer, until the entire surface layer is less dense than the top of CDW layer. During the summer, this mixture of AAWW and upwelled CDW is subsequently warmed and freshened by surface warming and sea ice melt to form AAIW. AAIW is also formed during the winter in both datasets. It seems that AAIW does not form during the summer in Drake Passage as

these processes seem to occur downstream from Drake Passage in the Atlantic sector of the ACC. These analyses in the Southern Ocean therefore reveal that a balance exists between the seasonal formation of water masses and the constant wind-driven process of upwelling and downwelling. Further, the diabatic transformation of CDW into AAIW occurs over the course of a season and its rate is governed by cabbeling.

The separate investigations on the seasonal and interannual variability in the Southern Ocean and North Atlantic reveal how the interaction between air–sea fluxes, mixing and transport variability set the temperature and salinity of the ocean. In the subtropical North Atlantic, the question remains as to whether the long-term upper ocean changes in temperature and salinity reflect a change in the transport divergence across the subtropical gyre or a change in the exchange of heat and freshwater at the sea-surface. Recent studies suggest the it is convergences and divergences in AMOC transport that set the heat and freshwater content in the North Atlantic (Lozier et al., 2010; Williams et al., 2013). Using an ocean model, the framework developed in this thesis could easily be used to determine the separate roles of transport divergence and air–sea fluxes in setting the long term changes of the volumetric distribution of water masses. The challenge remains in adapting these methods to understand changes in observational datasets. The work in chapter 2 presents the potential to estimate the interannual variability across the subtropical gyre using the thermohaline volume changes combined with estimates of wind-stress curl. Such transports could be constrained using time-series such as the RAPID-WATCH AMOC monitoring project, and could subsequently be used to extend such datasets. With longer estimates of the component of temperature and salinity change due to transport variations in the sub-tropical North Atlantic, estimates of changes in oceanic heat and freshwater content would be more representative of a diabatic change, and not aliased by adiabatic processes.

The importance of cabbeling in the diabatic transformation of water masses in the Southern Ocean, as revealed in this thesis, has important implications for our understanding of the overturning circulation, and the impact of anthropogenic climate change on the temperature/salinity properties of the Southern Ocean water masses. Firstly, this analysis may improve our ability to estimate the mean strength and interannual variability of the Southern Ocean overturning from hydrographic data. Specifically, if the majority of CDW is upwelled via this pathway, this represents the closure of the overturning in the Southern Ocean, as it is this diabatic transformation that draws CDW to the surface. This leads to the question that regards the impact a warming ocean would have on the mixing governed by cabbeling, and whether these impacts would alter the strength of the Southern Ocean overturning. Property changes in both the AAWW and CDW would affect the sensitivity of the water column to cabbeling and therefore the rate of CDW upwelling. An anomalous warming at the surface of the Southern Ocean during winter for example, would produce a warmer variety of AAWW. The critical salinity at which a warmer AAWW is unstable to cabbeling is higher. The critical salinity would

be equivalently higher for a warmer and saltier CDW, reflecting potential upstream changes in North Atlantic Deep Water. A higher critical salinity would require brine rejection through sea-ice formation to input more salt into AAWW to promote CDW upwelling. If in the current system, brine rejection injects salt into AAWW in excess, the system would be less sensitive to a warming ocean. Alternatively, if the current system reflects a delicate balance in the diabatic transformation of CDW, a warmer AAWW (or warmer/saltier CDW) would reduce the upwelling of CDW, stagnating the overturning circulation. A reduction in the upwelling of CDW may also increase the freshwater content of the upper ocean, further reducing mixing through cabbeling in a potential negative feedback. These contrasting scenarios reflect systems with a very different stability to a perturbed change, and warrant further investigation.

The work in chapter 5 assessed the effects of data interpolation on the distribution of volume in thermohaline coordinates. By developing a method to calculate the distribution of volume using individual profiles of temperature and salinity, it was possible to show that gridded products artificially mix water masses when interpolating data onto a regular grid. The volumetric distribution calculated directly from the profiles was higher in extreme temperature/salinity classes, and lower toward the centre of mass of the distribution. The profile-only approach was validated by sub-sampling profiles from a model grid and comparing the resultant volumetric distribution to that calculated using the full model grid. This chapter also showed that it is possible to construct a time-series of volume directly from profiles by defining an idealised seasonal cycle to account for periods of time when data coverage is low in some regions. Further development would be required before the approach could be applied to the types of analysis within this thesis.

That the process of interpolating temperature and salinity data onto a regular grid affects the properties of the volumetric distribution among temperature and salinity classes, raises questions relating to how well these datasets represent trends in the heat and freshwater content. Further, such effects may have implications for the momentum budgets determined from these data-sets. The extent to which trends in a gridded data-set may vary from those calculated using a profile-only approach would depend on whether the reduction in volume (and subsequently heat and freshwater) in opposing extreme temperature and salinity classes is equal. For example, if more volume is lost in cold/fresh classes than in warm/salty ones, this would impose an artificial warming and salinification. This thesis as of yet provides no evidence that such a process may be occurring, but it is something that warrants further investigation.

6.3 Recommendations for future work

This thesis presents many potential avenues for future work, which can be separated into two main groups. The first focuses on improving the water mass framework, while the second relates to the open questions that remain following the analyses in this thesis. The water mass framework could be used with additional tracers, encompassing biogeochemical variables. This could provide useful insight into biogeochemical cycling within the surface and deep ocean, or the ventilation time-scales of the ocean using tracers like dissolved oxygen or chlorofluorocarbons. With regards to improving the water mass framework, work is required to improve our understanding of how mixing is represented in this framework. Based on the work of Walin (1982), in thermohaline coordinates the difference between the total water mass transformation and the transformation implied by air–sea buoyancy fluxes must represent a transformation due to mixing. These residual transformations due to mixing are discussed throughout this thesis, and potential future analysis could work towards calculating isopycnal and diapycnal coefficients for mixing. As given in equations (3.1) and (4.8) the transformation across an isotherm or isohaline by mixing represents the divergence of a mixing tensor acting on a tracer gradient. Mixing coefficients could therefore be calculated by determining the diapycnal and isopycnal gradients of temperature and salinity along which this mixing is acting.

The directionality of the vectors representing transformations due in particular to mixing, is something that should also be explored further. The framework developed in this thesis calculates the minimum transformation across each isotherm and isohaline required to explain the volume change in each temperature/salinity class. It is given no information to regarding relative location and orientation of each water mass, therefore a given transformation may be physically unrealistic. This is most important for example, when regarding the direction of mixing along or across isopycnals. A vector calculated using this framework that represents mixing may suggest a diapycnal transformation that given particular local gradients in density is unlikely. Improving this aspect of the water mass framework may require constraining the least squares minimisation that calculates each vector with some information regarding the strength of the mean gradients at each point in temperature and salinity space.

Another potential for future work is the further development of the water mass volume climatology based on profile data. The first stage of development would be to work towards an improved estimate for the temporal variability of the volumetric distribution in thermohaline coordinates, reducing the noise in the time-series shown in this thesis. Further, determining the sensitivity of this estimate to the data coverage would also be another key step toward improving the profile-only approach. Beyond this, the method should be applied to the global ocean, while a platform for the dissemination of the resultant climatology could be created. Once the development of this water mass volume climatology reaches a suitable level of quality it would be informative to further

explore the effects of the difference from the volumetric distribution calculated using the geographically gridded climatology.

Most of the open questions that remain following the analyses in this thesis are discussed in section 6.2, and these provide many options for future work. In the investigation of the subtropical North Atlantic it would useful to extend the analysis in time, and to apply the approach to different regions of the ocean. Extending the time-series would determine if the strong correlations persist between the variability in the upper ocean volume/heat budget, the transport variability at the domain boundary and wind-driven heave. Extending the domain to beyond the subtropical gyre would also assess whether the wind-driven transport variability is as important in setting the heat budget in other regions of the worlds oceans. This would aid in answering the open question as to how much the transport divergence drives changes in the heat and freshwater budgets of the North Atlantic compared to the diabatic effects of anthropogenic climate change.

In the analysis of the diabatic transformation of CDW into AAIW, further work should involve estimating the sensitivity of the cabbeling mechanism to changes in the temperature and salinity of CDW and AAWW. The aim would therefore be to estimate the impact of anthropogenic climate change on the upwelling of CDW. This could be achieved using two potential approaches. The first would be to assess the interannual variability in the transformation of CDW into AAIW, and to how this compares to the properties of AAWW, CDW and AAIW. This would allow an assessment of the relationship between the intensity of mixing due to cabbeling and the properties of CDW and AAWW. An alternative approach that could also be used in addition to the first, would be to build an idealised numerical simulation to represent the interaction between AAWW and CDW. This would allow the properties of each water mass to be changed so that the sensitivity of the mixing between AAWW and CDW could be assessed to determine the stability of the system.

6.4 Conclusions

This thesis has developed a new framework describing oceanic variability and change in thermohaline coordinates. Using this water mass framework, changes related to air–sea buoyancy fluxes, mixing and transport are used to explain variations in water mass volumes. The analyses within this thesis focus on regions where the overturning circulation of the ocean is closely linked to the interannual and seasonal variations in air–sea buoyancy fluxes and sub-surface mixing. The aim was to understand how these processes interact to affect the momentum, heat and freshwater budgets of the ocean, allowing an improved understanding of the impacts of anthropogenic climate change in the ocean. In the subtropical North Atlantic it was shown that the volume and heat budget of the upper ocean is driven by wind-driven transport variations on interannual timescales.

This highlights the difficulty in solely attributing changes in North Atlantic temperature and salinity to diabatic processes. In the Southern Ocean, this thesis emphasised the importance of seasonal variations in air–sea buoyancy fluxes in driving the diabatic closure of the meridional overturning circulation via the non-linear properties of the equation of state for seawater. This new understanding will improve our ability to predict how the strength of the Southern Ocean overturning may change in a warming ocean. These analyses therefore demonstrate the suitability of the water mass framework developed within this thesis for unravelling the nature of oceanic change.

References

Abernathey, R., Marshall, J., and Ferreira, D. (2011). The dependence of southern ocean meridional overturning on wind stress. *Journal of Physical Oceanography*, 41(12):2261–2278.

Abernathey, R. P., Cerovecki, I., Holland, P. R., Newsom, E., Mazloff, M., and Talley, L. D. (2016). Water-mass transformation by sea ice in the upper branch of the southern ocean overturning. *Nature Geosci*, advance online publication:–.

Adler, R. F., Huffman, G. J., Chang, A., Ferraro, R., Xie, P.-P., Janowiak, J., Rudolf, B., Schneider, U., Curtis, S., Bolvin, D., Gruber, A., Susskind, J., Arkin, P., and Nelkin, E. (2003). The version-2 global precipitation climatology project (gpcp) monthly precipitation analysis (1979–present). *Journal of Hydrometeorology*, 4(6):1147–1167.

Anderson, D. L. and Gill, A. (1975). Spin-up of a stratified ocean, with applications to upwelling. *Deep Sea Research and Oceanographic Abstracts*, 22(9):583 – 596.

Andres, M., Kwon, Y.-O., and Yang, J. (2011). Observations of the kuroshio's barotropic and baroclinic responses to basin-wide wind forcing. *Journal of Geophysical Research: Oceans*, 116(C4):n/a–n/a.

Andres, M., Yang, J., and Kwon, Y.-O. (2012). Adjustment of a wind–driven two–layer system with mid–basin topography. *Journal of Marine Research*, 70(6):851–882.

Badin, G., Williams, R. G., Jing, Z., and Wu, L. (2013). Water mass transformations in the southern ocean diagnosed from observations: Contrasting effects of air–sea fluxes and diapycnal mixing. *Journal of Physical Oceanography*, 43(7):1472–1484.

Berry, D. I. and Kent, E. C. (2009). A new air–sea interaction gridded dataset from icoads with uncertainty estimates. *Bulletin of the American Meteorological Society*, 90(5):645–656.

Bindoff, N. L. and McDougall, T. J. (1994). Diagnosing climate change and ocean ventilation using hydrographic data. *Journal of Physical Oceanography*, 24:1137–1152.

Bindoff, N. L. and McDougall, T. J. (2000). Decadal changes along an Indian Ocean section at 32° S and their interpretation. *Journal of Physical Oceanography*, 30:1207–1222.

Böning, C. W., Dispert, A., Visbeck, M., Rintoul, S. R., and Schwarzkopf, F. U. (2008). The response of the Antarctic Circumpolar Current to recent climate change. *Nature Geoscience*, 1:864–869.

Boyer, T. P., Levitus, S., Antonov, J. I., Locarnini, R. A., and Garcia, H. E. (2005). Linear trends in salinity for the world ocean, 1955–1998. *Geophys. Res. Lett.*, 32(L01604).

Bryden, H. L., King, B. A., McCarthy, G. D., and McDonagh, E. L. (2014). Impact of a 30% reduction in atlantic meridional overturning during 2009–2010. *Ocean Science Discussions*, 11(2):789–810.

Bryden, H. L., McDonagh, E. L., and King, B. A. (2003). Changes in Ocean water mass properties: Oscillations or trends. *Science*, 300:2086–2088.

Buckley, M. W., Ponte, R. M., Forget, G., and Heimbach, P. (2014). Low-frequency SST and upper-ocean heat content variability in the North Atlantic. *Journal of Climate*, 27:4996–5018.

Calil, P. H. R. and Richards, K. J. (2010). Transient upwelling hot spots in the oligotrophic north pacific. *J. Geophys. Res.*, 115(C02003).

Cerovečki, I., Talley, L. D., and Mazloff, M. R. (2011). A comparison of southern ocean air–sea buoyancy flux from an ocean state estimate with five other products. *Journal of Climate*, 24(24):6283–6306.

Cerovečki, I., Talley, L. D., Mazloff, M. R., and Maze, G. (2013). Subantarctic mode water formation, destruction, and export in the eddy-permitting southern ocean state estimate. *Journal of Physical Oceanography*, 43(7):1485–1511.

Chelton, D. B., Schlax, M. G., and Samelson, R. M. (2011). Global observations of nonlinear mesoscale eddies. *Progress in Oceanography*, 91(2):167 – 216.

Collins, M., Knutti, R., Arblaster, J., Dufresne, J.-L., Friedlingstein, P., Gao, X., Gutowski, W. J., Johns, T. C., Krinner, G., Shongwe, M., Tebaldi, C., Weaver, A. J., and Wehner, M. (2013). *Long-term Climate Change: Projections, Commitments and Irreversibility. In: Climate Change 2013: The Physical Science Basis. Contribution of Working Group I to the Fifth Assessment Report of the Intergovernmental Panel on Climate Change*. Cambridge University Press, Cambridge, United Kingdom and New York, NY, USA.

Cunningham, S. A., Roberts, C. D., Frajka-Williams, E., Johns, W. E., Hobbs, W., Palmer, M. D., Rayner, D., Smeed, D. A., and McCarthy, G. (2013). Atlantic meridional overturning circulation slowdown cooled the subtropical ocean. *Geophysical Research Letters*, 40(23):2013GL058464.

Curry, R., Dickson, B., and Yashayaev, I. (2003). A change in the freshwater balance of the Atlantic Ocean over the past four decades. *Nature*, 426:826.

Curry, R. and Mauritzen, C. (2005). Dilution of the northern north atlantic ocean in recent decades. *Science*, 308(5729):1772–1774.

Curry, R. G., McCartney, M. S., and Joyce, T. M. (1998). Oceanic transport of subpolar climate signals to mid-depth subtropical waters. *Nature*, 391(6667):575–577.

Czaja, A. and Marshall, J. (2015). Why is there net surface heating over the antarctic circumpolar current? *Ocean Dynamics*, 65(5):751–760.

Dee, D. P., Uppala, S. M., Simmons, A. J., Berrisford, P., Poli, P., Kobayashi, S., Andrae, U., Balmaseda, M. A., Balsamo, G., Bauer, P., Bechtold, P., Beljaars, A. C. M., van de Berg, L., Bidlot, J., Bormann, N., Delsol, C., Dragani, R., Fuentes, M., Geer, A. J., Haimberger, L., Healy, S. B., Hersbach, H., Hólm, E. V., Isaksen, L., Kållberg, P., Köhler, M., Matricardi, M., McNally, A. P., Monge-Sanz, B. M., Morcrette, J.-J., Park, B.-K., Peubey, C., de Rosnay, P., Tavolato, C., Thépaut, J.-N., and Vitart, F. (2011). The era-interim reanalysis: configuration and performance of the data assimilation system. *Quarterly Journal of the Royal Meteorological Society*, 137(656):553–597.

Delcroix, T., Henin, C., Porte, V., and Arkin, P. (1996). Precipitation and sea-surface salinity in the tropical pacific ocean. *Deep Sea Research Part I: Oceanographic Research Papers*, 43(7):1123 – 1141.

Delcroix, T., McPhaden, M. J., Dessier, A., and Gouriou, Y. (2005). Time and space scales for sea surface salinity in the tropical oceans. *Deep Sea Research Part I: Oceanographic Research Papers*, 52(5):787 – 813.

Domingues, C. M., Church, J. A., White, N. J., Gleckler, P. J., Wijffels, S. E., Barker, P. M., and Dunn, J. R. (2008). Improved estimates of upper-ocean warming and multi-decadal sea-level rise. *Nature*, 453(7198):1090–1093.

Döös, K., Nilsson, J., Nycander, J., Brodeau, L., and Ballarotta, M. (2012). The world ocean thermohaline circulation. *Journal of Physical Oceanography*, 42(9):1445–1460.

Downes, S. M., Bindoff, N. L., and Rintoul, S. R. (2009). Impacts of climate change on the subduction of mode and intermediate water masses in the southern ocean. *Journal of Climate*, 23:6526–6541.

Durack, P. J. and Wijffels, S. E. (2010). Fifty year trends in global ocean salinities and their relationship to broadscale warming. *Journal of Climate*, 23:4342–4362.

Durack, P. J., Wijffels, S. E., and Matear, R. J. (2012). Ocean salinities reveal strong global water cycle intensification during 1950 to 2000. *Science*, 336:455–458.

Evans, D. G., Zika, J. D., Naveira Garabato, A. C., and Nurser, A. J. G. (2014). The imprint of southern ocean overturning on seasonal water mass variability in drake passage. *Journal of Geophysical Research: Oceans*, 119(11):7987–8010.

Ferrari, R. and Ferreira, D. (2011). What processes drive the ocean heat transport. *Ocean Modelling*, 38:171–186.

Fofonoff, N. (1957). Some properties of sea water influencing the formation of antarctic bottom water. *Deep Sea Research (1953)*, 4:32 – 35.

Forget, G., Campin, J.-M., Heimbach, P., Hill, C. N., Ponte, R. M., and Wunsch, C. (2015). Ecco version 4: an integrated framework for non-linear inverse modeling and global ocean state estimation. *Geoscientific Model Development Discussions*, 8(5):3653–3743.

Forget, G., Maze, G., Buckley, M., and Marshall, J. (2011). Estimated seasonal cycle of north atlantic eighteen degree water volume. *Journal of Physical Oceanography*, 41(2):269–286.

Forget, G. and Ponte, R. M. (2015). The partition of regional sea level variability. *Progress in Oceanography*, 137, Part A:173 – 195.

Foster, T. D. and Carmack, E. C. (1976). Temperature and salinity structure in the weddell sea. *Journal of Physical Oceanography*, 6(1):36–44.

Fyfe, J. C. and Saenko, O. A. (2006). Simulated changes in the extratropical southern hemisphere winds and currents. *Geophys. Res. Lett.*, 33(6).

Gent, P. R. and McWilliams, J. C. (1990). Isopycnal mixing in ocean circulation models. *Journal of Physical Oceanography*, 20:150–155.

Grist, J. P., Josey, S. A., Marsh, R., Kwon, Y.-O., Bingham, R. J., and Blaker, A. T. (2014). The surface-forced overturning of the north atlantic: Estimates from modern era atmospheric reanalysis datasets. *Journal of Climate*, 27(10):3596–3618.

Grist, J. P., Marsh, R., and Josey, S. A. (2009). On the relationship between the north atlantic meridional overturning circulation and the surface-forced overturning streamfunction. *Journal of Climate*, 22(19):4989–5002.

Groeskamp, S. J., Zika, J. D., McDougall, T. J., Sloyan, B. M., and Laliberté, F. (2014). The representation of ocean circulation and variability in thermodynamic coordinates. *Submitted to the Journal of Physical Oceanography.*

Häkkinen, S., Rhines, P. B., and Worthen, D. L. (2011). Warm and saline events embedded in the meridional circulation of the northern north atlantic. *Journal of Geophysical Research: Oceans*, 116(C3):n/a–n/a. C03006.

Häkkinen, S., Rhines, P. B., and Worthen, D. L. (2015). Heat content variability in the north atlantic ocean in ocean reanalyses. *Geophysical Research Letters*, 42(8):2901–2909. 2015GL063299.

Helm, K. P., Bindoff, N. L., and Church, J. A. (2010). Changes in the global hydrologicalcycle inferred from ocean salinity. *Geophys. Res. Lett.*, 37(L18701).

Hieronymus, M., Nilsson, J., and Nycander, J. (2014). Water mass transformation in salinity–temperature space. *Journal of Physical Oceanography*, 44(9):2547–2568.

Hirschi, J. and Marotzke, J. (2007). Reconstructing the meridional overturning circulation from boundary densities and the zonal wind stress. *J. Phys. Oceanogr.*, 37:743–763.

Hosoda, S., Suga, T., Shikama, N., and Mizuno, K. (2009). Global surface layer salinity change detected by argo and its implication for hydrological cycle intensification. *Journal of Oceanography*, 65:579–586.

Imbrie, J., Boyle, E. A., Clemens, S. C., Duffy, A., Howard, W. R., Kukla, G., Kutzbach, J., Martinson, D. G., McIntyre, A., Mix, A. C., Molfino, B., Morley, J. J., Peterson, L. C., Pisias, N. G., Prell, W. L., Raymo, M. E., Shackleton, N. J., and Toggweiler, J. R. (1992). On the structure and origin of major glaciation cycles 1. linear responses to milankovitch forcing. *Paleoceanography*, 7(6):701–738.

IOC, SCOR, and IAPSO (2010). *The international thermodynamic equation of seawater - 2010: Calculation and use of thermodynamic properties.* UNESCO (English), manuals and guides no. 56 edition.

Johns, W. E., Baringer, M. O., Beal, L. M., Cunningham, S. A., Kanzow, T., Bryden, H. L., Hirschi, J. J. M., Marotzke, J., Meinen, C. S., Shaw, B., and Curry, R. (2010). Continuous, array-based estimates of atlantic ocean heat transport at 26.5 °n. *Journal of Climate*, 24(10):2429–2449.

Johnson, H. L. and Marshall, D. P. (2002). A theory for the surface atlantic response to thermohaline variability. *J. Phys. Oceanogr.*, 32:1121–1132.

Josey, S. A. (2011). Air–sea fluxes of heat, freshwater and momentum. In Schiller, A. and Brasington, G. B., editors, *Operational Oceanography in the 21st Century*, pages 155–184. Springer Netherlands.

Josey, S. A., Kent, E. C., and Taylor, P. K. (1999). New insights into the ocean heat budget closure problem from analysis of the soc air–sea flux climatology. *Journal of Climate*, 12(9):2856–2880.

Kalnay, E., Kanamitsu, M., Kistler, R., Collins, W., Deaven, D., Gandin, L., Iredell, M., Saha, S., White, G., Woollen, J., Zhu, Y., Leetmaa, A., Reynolds, R., M. Chelliah, W. Ebisuzaki, W. H., Janowiak, J., Mo, K. C., Ropelewski, C., Wang, J., Jenne, R., and Joseph, D. (1996). The ncep/ncar 40-year reanalysis project. *Bulletin of the American Meterological Society*, 77(3):437–471.

Kobayashi, T., Mizuno, K., and Suga, T. (2012). Long-term variations of surface and intermediate waters in the southern indian ocean along 32 °s. *Journal of Oceanography*, 68:243–265.

Lozier, M. S., Roussenov, V., Reed, M. S. C., and Williams, R. G. (2010). Opposing decadal changes for the north atlantic meridional overturning circulation. *Nature Geoscience*, 3:728–734.

Maidens, A., Arribas, A., Scaife, A. A., MacLachlan, C., Peterson, D., and Knight, J. (2013). The influence of surface forcings on prediction of the north atlantic oscillation regime of winter 2010/11. *Monthly Weather Review*, 141(11):3801–3813.

Marsh, R., Josey, S. A., de Nurser, A. J. G., Cuevas, B. A., and Coward, A. C. (2005). Water mass transformation in the north atlantic over 1985-2002 simulated in an eddy-permitting model. *Ocean Science*, 1(2):127–144.

Marsh, R., Nurser, A. J. G., Megann, A. P., and New, A. L. (2000). Water mass transformation in the Southern Ocean of a global isopycnal coordinate GCM. *Journal of Physical Oceanography*, 30:1013–1045.

Marshall, J. and Radko, T. (2003). Residual-mean solutions for the antarctic circumpolar current and its associated overturning circulation. *Journal of Physical Oceanography*, 33(11):2341–2354.

Marshall, J. and Speer, K. (2012). Closure of the meridional overturning circulation through southern ocean upwelling. *Nature Geosci*, 5(3):171–180.

Maze, G., Farget, G., Buckley, M., Marshall, J., and Cerovecki, I. (2009). Using Transformation and Formation Maps to Study the Role of Air–Sea Heat Fluxes in North Atlantic Eighteen Degree Water Formation. *Journal of Physical Oceanography*, 39:1818–1835.

McCarthy, G., Frajka-Williams, E., Johns, W. E., Baringer, M. O., Meinen, C. S., Bryden, H. L., Rayner, D., Duchez, A., Roberts, C., and Cunningham, S. A. (2012a). Observed interannual variability of the atlantic meridional overturning circulation at 26.5 °n. *Geophysical Research Letters*, 39(19).

McCarthy, G., McDonagh, E., and King, B. (2011). Decadal variability of thermocline and intermediate waters at 24° s in the south atlantic. *Journal of Physical Oceanography*, 41:157–165.

McCarthy, G. D., King, B. A., Cipollini, P., McDonagh, E. L., Blundell, J. R., and Biastoch, A. (2012b). On the sub-decadal variability of south atlantic antarctic intermediate water. *Geophys. Res. Lett.*, 39(L10605).

McDonagh, E. L., Bryden, H. L., King, B. A., Sanders, R. J., Cunningham, S. A., and Marsh, R. (2005). Decadal changes in the south indian ocean thermocline. *Journal of Climate*, 18:1575–1590.

McDougall, T. J. (1987). Thermobaricity, cabbeling, and water–mass conservation. *Journal of Geophysical Research*, 92(c5):5448–5464.

McGillicuddy, D. J., Anderson, L. A., Bates, N. R., Bibby, T., Buesseler, K. O., Carlson, C. A., Davis, C. S., Ewart, C., Falkowski, P. G., Goldthwait, S. A., Hansell, D. A., Jenkins, W. J., Johnson, R., Kosnyrev, V. K., Ledwell, J. R., Li, Q. P., Siegel, D. A., and Steinberg, D. K. (2007). Eddy/wind interactions stimulate extraordinary mid-ocean plankton blooms. *Science (New York, N.Y.)*, 316(5827):1021–1026.

Meijers, A. J., Bindoff, N. L., and Rintoul, S. R. (2011). Frontal movements and property fluxes: Contributions to heat and freshwater trends in the southern ocean. *J. Geophys. Res.*, 116(C08024).

Meredith, M. P., Woodworth, P. L., Chereskin, T. K., Marshall, D. P., Allison, L. C., Bigg, G. R., Donohue, K., Heywood, K. J., Hughes, C. W., Hibbert, A., Hogg, A. M., Johnson, H. L., Jullion, L., King, B. A., Leach, H., Lenn, Y.-D., Morales Maqueda, M. A., Munday, D. R., Naveira Garabato, A. C., Provost, C., Sallée, J.-B., and Sprintall, J. (2011). Sustained monitoring of the southern ocean at drake passage: Past achievements and future priorities. *Reviews of Geophysics*, 49(4):n/a–n/a.

Morrison, A. K., England, M. H., and Hogg, A. M. (2015). Response of southern ocean convection and abyssal overturning to surface buoyancy perturbations. *Journal of Climate*, 28(10):4263–4278.

Naveira Garabato, A. C., Jullion, L., Stevens, D. P., Heywood, K. J., and King, B. A. (2009). Variability of subantarctic mode water and antarctic intermediate water in the drake passage during the late-twentieth and early-twenty-first centuries. *Journal of Climate*, 22(13):3661–3688.

Naveira Garabato, A. C., Stevens, D. P., Watson, A. J., and Roether, W. (2007). Short-circuiting of the overturning circulation in the Antarctic Circumpolar Current. 440:194–197. doi:10.1038/nature05832.

Nurser, A. J. G. and Marsh, R. (1998). Water mass transformation theory and the meridional overturning streamfunction. *International WOCE newsletter*, 31:36–38.

Nurser, A. J. G., Marsh, R., and Williams, R. G. (1999). Diagnosing water mass formation from air–sea fluxes and surface mixing. *Journal of Physical Oceanography*, 29:1468–1487.

Palmer, M. D. and Haines, K. (2009). Estimating oceanic heat content change using isotherms. *Journal of Climate*, 22(19):4953–4969.

Pardaens, A., Vellinga, M., Wu, P., , and Ingleby, B. (2008). Large-scale atlantic salinity changes over the last half-century: A model–observation comparison. *Journal of Climate*, 21:1698–1720.

Park, Y.-H., Charriaud, E., and Fieux, M. (1998). Thermohaline structure of the antarctic surface water/winter water in the indian sector of the southern ocean. *Journal of Marine Systems*, 17(1–4):5 – 23.

Polo, I., Robson, J., Sutton, R., and Balmaseda, M. A. (2014). The importance of wind and buoyancy forcing for the boundary density variations and the geostrophic component of the amoc at 26 °n. *Journal of Physical Oceanography*, 44(9):2387–2408.

Purkey, S. G. and Johnson, G. C. (2010). Warming of global abyssal and deep southern ocean waters between the 1990s and 2000s: Contributions to global heat and sea level rise budgets*. *Journal of Climate*, 23(23):6336–6351.

Reynolds, R. W., Rayner, N. A., Smith, T. M., Stokes, D. C., and Wang, W. (2004). An Improved In Situ and Satellite SST Analysis for Climate.

Richardson, P. L. (2008). On the history of meridional overturning schematic diagrams. *Progress in Oceanography*, 76:466–486.

Ridgway, K. R., Dunn, J. R., and Wilkin, J. L. (2002). Ocean interpolation by four-dimensional weighted least squares—application to the waters around australasia. *Journal of Atmospheric and Oceanic Technology*, 19(9):1357–1375.

Rintoul, S. R. and Naveira-Garabato, A. C. (2013). Dynamics of the southern ocean circulation. In Siedler, G., Griffies, S. M., Gould, J., and Church, J., editors, *Ocean Circulation and Climate, 2nd Edition: A 21st Century Perspective*, pages 471–492. Academic Press, Oxford GB.

Roberts, C. D., Waters, J., Peterson, K. A., Palmer, M. D., McCarthy, G. D., Frajka-Williams, E., Haines, K., Lea, D. J., Martin, M. J., Storkey, D., Blockley, E. W., and Zuo, H. (2013). Atmosphere drives recent interannual variability of the atlantic meridional overturning circulation at 26.5 °n. *Geophysical Research Letters*, 40(19):5164–5170.

Roemmich, D. and Gilson, J. (2009). The 2004–2008 mean and annual cycle of temperature, salinity, and steric height in the global ocean from the argo program. *Progress in Oceanography*, 82(2):81 – 100.

Roemmich, D., John Gould, W., and Gilson, J. (2012). 135 years of global ocean warming between the challenger expedition and the argo programme. *Nature Clim. Change*, 2(6):425–428.

Sabine, C. L., Feely, R. A., Gruber, N., Key, R. M., Lee, K., Bullister, J. L., Wanninkhof, R., Wong, C. S., Wallace, D. W. R., Tilbrook, B., Millero, F. J., Peng, T.-H., Kozyr, A., Ono, T., and Rios, A. F. (2004). The Oceanic Sink for Anthropogenic CO2. *Science*, 305:367–371.

Schanze, J., Schmitt, R., and Yu, L. (2010). The global oceanic freshwater cycle: A state-of-the-art quantification. *Journal of Marine Research*, 68(3-4):569–595.

Schiffer, R. A. and Rossow, W. B. (1985). Isccp global radiance data set: A new resource for climate research. *Bulletin of the American Meteorological Society*, 66(12):1498–1505.

Schloesser, F., Furue, R., McCreary, J., and Timmermann, A. (2014). Dynamics of the atlantic meridional overturning circulation. part 2: Forcing by winds and buoyancy. *Progress in Oceanography*, 120:154 – 176.

Schulz, E. W., Josey, S. A., and Verein, R. (2012). First air-sea flux mooring measurements in the southern ocean. *Geophysical Research Letters*, 39(16).

Smeed, D., McCarthy, G., Rayner, D., Moat, B., Johns, W., Baringer, M., and Meinen, C. (2015). Atlantic meridional overturning circulation observed by the rapid-mocha-wbts (rapid-meridional overturning circulation and heatflux array-western boundary time series) array at 26n from 2004 to 2014.

Smith, S. R., Hughes, P. J., and Bourassa, M. A. (2011). A comparison of nine monthly air–sea flux products. *International Journal of Climatology*, 31(7):1002–1027.

Sonnewald, M., Hirschi, J. J.-M., Marsh, R., McDonagh, E. L., and King, B. A. (2013). Atlantic meridional ocean heat transport at 26n: impact on subtropical ocean heat content variability. *Ocean Science*, 9(6):1057–1069.

Speer, K. and Forget, G. (2013). Chapter 9 - global distribution and formation of mode waters. In Gerold Siedler, Stephen M. Griffies, J. G. and Church, J. A., editors, *Ocean Circulation and ClimateA 21st Century Perspective*, volume 103 of *International Geophysics*, pages 211 – 226. Academic Press.

Speer, K. and Tziperman, E. (1992). Rates of water mass formation in the North Atlantic Ocean. *Journal of Physical Oceanography*, 22:93–104.

Speer, K. G. (1993). Conversion among north atlantic surface water types. *Tellus*, 45:72–79.

Speer, K. G., Rintoul, S. R., and Sloyan, B. M. (2000). The diabatic Deacon cell. *Journal of Physical Oceanography*, 30:3212–3222.

Stephens, G. L., L'Ecuyer, T., Forbes, R., Gettlemen, A., Golaz, J., BodasSalcedo, A., Suzuki, K., Gabriel, P., and Haynes, J. (2010). Dreary state of precipitation in global models. *J. Geophys. Res.*, 115(D24211).

Talley, L. D. (1996). Antarctic Intermediate Water in the South Atlantic. In Wefer, G., Berger, W. H., Siedler, G., and Webb, D. J., editors, *The South Atlantic: Present and Past Circulation*, pages 219–238. Springer–Verlag Berlin Heidelberg.

Talley, L. D. (2013). Closure of the global overturing circulation through the indian, pacific, and southern oceans: Schematics and transports. *Oceanography*, 26(1):80–97.

Thomas, J. L., Waugh, D. W., and Gnanadesikan, A. (2015). Southern hemisphere extratropical circulation: Recent trends and natural variability. *Geophysical Research Letters*, 42(13):5508–5515. 2015GL064521.

Trenberth, K. E. and Caron, J. M. (2001). Estimates of meridional atmosphere and ocean heat transports. *Journal of Climate*, 14:3433–3443.

Walin, G. (1982). On the relation between sea–surface heat flow and thermal circulation in the ocean. *Tellus*, 34:187–195.

Willebrand, J., Philander, G. H., and Pacanowski, R. C. (1980). The oceanic response to large-scale atmospheric disturbances. *Journal of Physical Oceanography*, 10:411–429.

Williams, R. G., Roussenov, V., Smith, D., and Lozier, M. S. (2013). Decadal evolution of ocean thermal anomalies in the north atlantic: The effects of ekman, overturning, and horizontal transport. *Journal of Climate*, 27(2):698–719.

Wunsch, C. and Heimbach, P. (2013a). Dynamically and kinematically consistent global ocean circulation state estimates with land and sea ice. In Siedler, G., Griffies, S. M., Gould, J., and Church, J., editors, *Ocean Circulation and Climate, 2nd Edition: A 21st Century Perspective*, pages 553–579. Academic Press, Oxford GB.

Wunsch, C. and Heimbach, P. (2013b). Two decades of the atlantic meridional overturning circulation: Anatomy, variations, extremes, prediction, and overcoming its limitations. *Journal of Climate*, 26(18):7167–7186.

Wunsch, C. and Heimbach, P. (2014). Bidecadal thermal changes in the abyssal ocean. *Journal of Physical Oceanography*, 44(8):2013–2030.

Yang, J. (2015). Local and remote wind stress forcing of the seasonal variability of the atlantic meridional overturning circulation (amoc) transport at 26.5 °n. *Journal of Geophysical Research: Oceans*, 120(4):2488–2503.

Yu, L. and Jin, X. (2014). Insights on the oaflux ocean surface vector wind analysis merged from scatterometers and passive microwave radiometers (1987 onward). *Journal of Geophysical Research: Oceans*, 119(8):5244–5269.

Yu, L., Jin, X., and Weller, R. A. (2006). Role of net surface heat flux in seasonal variations of sea surface temperature in the tropical atlantic ocean. *Journal of Climate*, 19(23):6153–6169.

Zika, J. D., England, M. H., and Sijp, W. P. (2012). The Ocean Circulation in Thermohaline Coordinates. *Journal of Physical Oceanography*, 2:708–724.

Zika, J. D., Skliris, N., Nurser, A. J. G., Josey, S. A., Mudryk, L., Laliberté, F., and Marsh, R. (2015). Maintenance and broadening of the ocean's salinity distribution by the water cycle. *Journal of Climate*, 28(24):9550–9560.

Zika, J. D., Sloyan, B. M., and McDougall, T. J. (2009). Diagnosing the Southern Ocean Overturning from tracer fields. *Journal of Physical Oceanography*, 39:2926–2940.